UNIVERSITÀ
DEGLI STUDI
DI PADOVA

University of Padova
Department of Industrial Engineering
PhD School in Industrial Engineering – XXVIII ciclo
Curriculum: Chemical, Materials and Mechanical Engineering

Centre for Mechanics of Biological Materials

INTEGRATED EXPERIMENTAL AND NUMERICAL APPROACH TO THE BIOMECHANICS OF SURGICAL MESHES EVALUATING INTERACTION PHENOMENA WITH REGARD TO ABDOMINAL WALL REPAIR

Director of the School: Ch.mo Prof. Paolo Colombo
Coordinator: Prof. Enrico Savio
Supervisor: Ch.mo Prof. Arturo N. Natali
Co-supervisor: Prof. Piero G. Pavan

PhD candidate: Paola Pachera

ABSTRACT

The research activity performed is addressed to the evaluation of the interaction phenomena between surgical meshes and native biological tissues and structures, with the aim to assess the biomechanical compatibility, which represents a mandatory factor for successful adoptions in different surgical procedures. The mechanical characterization of meshes for repairs is performed by means of an integrated experimental-numerical approach, in direct correlation with the surgical techniques.

Surgical grafts can origin from different sources and they can be classified as synthetic or biological, characterized by peculiar biochemical and mechanical properties and, consequently, by different biomechanical performances. Biological grafts are derived from collagen-rich tissues and can be drawn from animal (xenografts) or human (allograft) sources, the latter are usually obtained from the fascial system. For this reason, the mechanical characterization of fascial tissues is performed, evaluating the in situ functional role in the interaction with surrounding biological structures. With the purpose to interpret fascial tissues mechanical behaviour, which is characterized by anisotropy, coupled geometric and material non-linearity and time-dependent phenomena, a specific fiber reinforced visco-hyperelastic model is provided. The constitutive parameters evaluation is performed through the minimization of a cost function that defines the discrepancy between experimental data and results from the model of the tensile tests. The optimization technique, based on the Simulated Annealing optimization algorithm, leads to the definition of the set of constitutive parameters to be adopted within the constitutive formulation and implemented in the model, with the purpose to achieve a suitable description of tissue in situ mechanical behaviour.

The preliminary phase of fascial tissues performances is investigated through numerical analysis of the anterior compartment of the leg. The response in this region allow for a definition of the

characteristic facial tissues behaviour and is of clinical interest in the several painful syndrome, as the compartment syndrome, also offering the possibility of several references in literature.

As an example of xenograft, Permacol ™ is characterized through experimental analysis and constitutive modelling. It is derived from decellularized and cross-linked porcine skin and it is a graft commonly used in abdominal wall surgery.

As far as synthetic meshes is concerned, Bard® Soft mesh is studied, as a lightweight, large pore monofilament polypropylene mesh, following the above mentioned procedure.

The mechanical investigation of different kinds of surgical meshes is fundamental for the definition of the numerical model of the herniated and repaired human abdominal wall. The reconstruction of the abdominal region is based on MR images integrated with data from literature. Constitutive formulations of the different biological tissues of the anatomical region are provided. The numerical model allows the analysis of different configurations, firstly considering the healthy abdomen to assess its overall mechanical behaviour in physiological conditions. Then a hernia defect is introduced in the abdominal wall, with size and position defined in accordance with clinical evidences, virtually repaired by means of different kinds of grafts (biologic and synthetic). The purpose is to evaluate the mechanical interaction between native abdominal wall tissues and structures and surgical meshes, to assess the mechanical functional response and compatibility. The analysis allows the comparison between physiological and pathological conditions and between different kinds of meshes, by means of the estimation of the stress and strain fields within biological tissues and prosthesis. Attention is paid to the interaction at tissue-implant interface, providing a useful computational tool for the evaluation of surgical strategies in dependence on prosthesis configuration.

The investigation entails a relevant experimental effort, essential for the extensive numerical analysis of the anatomical district considered, providing a result evaluation by direct correlation with surgical competences.

SOMMARIO

Lo scopo della presente ricerca consiste nella valutazione dei fenomeni di interazione che si vengono a creare nell’accoppiamento di mesh chirurgiche e tessuti e strutture biologiche. La valutazione della compatibilità meccanica tra tessuti e impianto rappresenta un fattore fondamentale per il buon esito dell’intervento. In quest’ottica, risulta necessaria la caratterizzazione meccanica delle mesh chirurgiche che viene condotta attraverso un approccio numerico-sperimentale integrato, in diretta correlazione con le tecniche chirurgiche.

Le mesh chirurgiche hanno differente origine e possono essere classificate come sintetiche o biologiche, caratterizzate da particolari proprietà biochimiche e meccaniche e, conseguentemente, da differenti prestazioni. Le mesh biologiche sono ricavate da tessuti ricchi di collagene e possono essere di origine animale (xenograft) o umana (allograft), queste ultime sono principalmente ottenute dal sistema fasciale. Per questo motivo i tessuti fasciali vengono caratterizzati meccanicamente, valutandone il ruolo funzionale in situ in interazione con le circostanti strutture biologiche. Uno specifico modello visco-iperelastico e fibrorinforzato viene utilizzato allo scopo di interpretare il comportamento meccanico dei tessuti biologici, caratterizzati da proprietà di anisotropia, grandi deformazioni e fenomeni dipendenti dal tempo. I parametri costitutivi vengono definiti attraverso la minimizzazione di una funzione costo che esprime la differenza tra dati sperimentali e dati numerici. La tecnica di ottimizzazione, basata sull’algoritmo di ottimizzazione del Simulated Annealing, porta all’individuazione di un set di parametri costitutivi che vengono adottati nella formulazione costitutiva, successivamente implementata nel modello numerico, allo scopo di ottenere un’adeguata descrizione del comportamento meccanico del tessuto in situ.

Analisi numeriche sul compartimento anteriore della gamba vengono utilizzate per lo studio della meccanica dei tessuti fasciali di questo distretto. Il compartimento anteriore è di particolare

interesse clinico a causa delle diverse patologie a carico di tale regione come, ad esempio, la sindrome compartimentale.

La mesh chirurgica Permacol™ viene studiata come esempio di xenograft e caratterizzata attraverso analisi sperimentale e modellazione costitutiva. Tale mesh, comunemente utilizzata nella ricostruzione della parete addominale, è ottenuta da derma suino debitamente decellularizzato e trattato al fine di ottenere cross-links.

La mesh Bard® Soft viene studiata in quanto esempio di mesh sintetica leggera in polipropilene, caratterizzata da elevata porosità.

L'analisi meccanica di diversi tipi di mesh è fondamentale per la definizione del modello numerico della parete addominale erniata e virtualmente riparata. La ricostruzione della geometria della regione addominale viene effettuata attraverso immagini diagnostiche (MR) e dati di letteratura. Nel testo viene specificata la formulazione costitutiva adottata per la descrizione dei diversi tessuti componenti la regione addominale. Il modello numerico permette una prima valutazione del comportamento meccanico globale della parete addominale integra in condizioni fisiologiche. Successivamente, nel modello, viene introdotta una porta erniaria di posizione e dimensioni compatibili con le evidenze cliniche. Tale difetto viene virtualmente riparato con mesh chirurgiche caratterizzate in diverso modo (biologica e sintetica). Lo scopo consiste nella valutazione dell'interazione meccanica tra mesh chirurgiche e i tessuti biologici, considerandone la compatibilità della risposta meccanica funzionale. Le analisi numeriche permettono di valutare il comportamento della parete addominale sana con quello della parete riparata confrontando i campi di tensione e deformazione di tessuti biologici e mesh chirurgica. Il modello numerico proposto fornisce una prima valutazione degli effetti, indotti dalla presenza della protesi, sul comportamento meccanico globale della parete addominale e fornisce gli strumenti per future valutazioni utili alla pianificazione chirurgica e alla configurazione della protesi.

Lo studio proposto si fonda su una forte base sperimentale, essenziale per lo svolgimento delle successive analisi numeriche.

INDEX

INTRODUCTION

Nowadays the increasing use of different kinds of meshes represents a clear trend in many surgical areas, such as gastrointestinal, urological and gynaecological. In particular, a very meaningful example of their application is represented by the abdominal wall repair and reconstruction. For this reason it is necessary meshes investigation and characterization under different aspects for the identification of suitable and effective solutions. The aim of this research is focused on the study of the interaction phenomena between surgical meshes and native biological tissues to assess their biomechanical compatibility, which represents a mandatory factor for successful substitutions. Surgical meshes can be classified either synthetic or biological depending on their origin, each one characterized by peculiar biochemical and mechanical features and, consequently, by different performances. Further, biological grafts that are derived from collagen-rich tissues can be drawn from animal (xenografts) or human (allograft) sources. These latter are mainly obtained from the fascial system stressing the importance on their mechanical characterization also considering their functional role in situ and their interaction with the surrounding structures. Fascial tissues are also involved in several tasks as transmission of forces and transpositions of loads among adjacent body regions and covers a fundamental mechanical role.

This study is carried out through an integrated experimental-numerical approach, adopted as general method of investigation. As pertains biological tissues, the investigation starts from accurate histological and morphometric analyses, while the study of synthetic surgical meshes begins with considerations about morphometrical characteristics. This preliminary step allows to define suitable loading protocols for mechanical tests aimed at the investigation of the viscoelastic properties of the tissues. This action is followed by the development of a constitutive model capable to supply a suitable interpretation of the material behaviour by means of a visco-hyperelastic anisotropic formulation, which properly describes its mechanical behavior characterized by nonlinear, anisotropic and viscoelastic response. The evaluation of the constitutive parameters is performed by means of optimization procedures through the minimization of a cost function expressing the difference between experimental and numerical data according to a stochastic-deterministic procedure.

The constitutive model is finally implemented in a finite element code and the numerical outputs are validated by means of the comparison with additional experimental data.

In this work, the numerical modelling is firstly addressed to the analysis of the mechanical characteristics of the human crural fascia taking into account its structural conformation by the reconstruction of the specific anatomical region of the anterior compartment. Numerical analyses allow to assess the tissue biomechanics under different loading conditions, letting possible to understand its effective behaviour.

Other materials as, a porcine xenograft and a synthetic patch, that are commonly used in abdominal wall surgery, are here characterized with the aim to analyse the abdominal wall reconstruction by means of different kinds of meshes.

The model of a healthy and herniated abdominal wall is here developed and its reconstruction is simulated exploiting the mechanical characterization of the above mentioned meshes. The performed numerical analyses have the purpose to supply a useful indirect tool to help the choice of the most suitable mesh. This study has a strong and direct correlation with the surgical planning and practice.

The first chapter deals with the different kinds of meshes, both synthetic and biological, commonly used in surgery. The attention is mainly focused on allografts drawn from human fascial system with the aim to provide information about tissue histological composition and function, with the preponderant objective of characterizing its biomechanical role.

The second chapter explains the experimental analysis performed on tissues by means of different mechanical tests. It is here reported the general constitutive formulation adopted for interpreting the mechanical behaviour of soft connective tissues and the optimization procedure for the identification of the constitutive parameters.

In chapter three the performed investigations about human crural fascia are reported, firstly with the development of the finite element model of a leg section and then with its extension to the three dimensional case with the reconstruction, detailed step by step, of the structure of an anterior compartment. Numerical analyses allow the definition of tissue mechanical characteristic and structural behaviour under different physiological conditions.

In chapter four it is detailed the development of the abdominal wall model and its different components. The wall reconstruction is analysed by means of a mesh, which is characterized in different ways. Firstly the mesh is assumed with the mechanical characteristics of the previously studied Permacol™ graft and then with those of a synthetic mesh (Bard® Soft mesh), letting possible the comparison between these different materials.

CHAPTER 1 TISSUE SUBSTITUTES

1.1 Introduction

Applications of surgical meshes represent a common practice in a variety of fields: in the substitution of parts of vessels and heart valves reconstruction in cardiac surgery, in the correction of the pelvic organ prolapse in uro-gynecologic interventions, in the reconstruction of tendons and ligaments, as well as in facial surgery. The principal and most widespread example of surgical application of these materials is represented by the abdominal wall reconstruction.

Independently of the kind of surgical intervention, the implanted materials in interaction with tissues and body fluids have to ensure a good degree of compatibility for successful interventions. Such compatibility is evaluated under different aspects, one of the firsts is represented by the consideration of meshes chemical and biocompatibility characteristics that are mainly related to their composition. The ideal mesh should be non-carcinogenic, chemically inert, stable in contact with body fluids, able to limit foreign body reaction, allergy or hypersensitivity reactions and resistant to infection [1].

Another fundamental aspect that has to be considered is represented by the biomechanical and functional compatibility of the implant in interaction and integration with the surrounding biological structures. It is known that, in order to achieve a successful and lasting substitution intervention, meshes have to mimic biomechanical properties of native tissues to provide a natural continuity in loads transposition between the implant and the host tissues. In particular, discontinuities in mechanical properties could lead to stress concentrations at the implant-tissue interface causing the endangerment of the surgical site mechanical functionality. As a matter of example, in the reconstruction of the abdominal wall the biological grafts should match the mechanical properties of host tissues to supply an efficient answer during the occurrence of mechanical limit conditions represented by intense abdominal pressure due to coughing or vomiting [2].

Several kinds of surgical grafts are commercially available and can be derived from different sources. They can be either synthetic or biological both characterized by specific biochemical and mechanical features that appoint different performances to the materials, making them more suitable for specific uses. Studies at disposal report that synthetic surgical meshes are associated to a number of complications due to the inadequate active interaction with biological tissues. Bacteria colonization can induce mesh infection or unwanted chronic inflammations, due to foreign body reaction, leading sometimes to mesh extrusion [3-5]. Other unwanted effects are represented by skin erosion, seroma formation, bowel obstruction or fistula formation [3]. All those events, also related to the biomechanical performance, have a strong impact on the implant functionality and can lead to its untimely endangerment. An alternative to synthetic mesh is represented by biological meshes that show better properties as pertain both the biochemical and biomechanical compatibility. Biological grafts derived from animals are called xenografts and originate from bovine and porcine sources, while allografts are meshes from human tissues.

Considerations about meshes biocompatibility are beyond the purpose of this work, which focuses its attention on the investigation of the mechanical characteristics of meshes considering the mechanical and anisotropic properties of the materials in relation to the specific surgical application.

1.2 Synthetic meshes

Permanent synthetic meshes are commonly adopted in the surgical procedure of the abdominal wall reconstruction. The polymeric materials used in synthetics manufacturing are polypropylene (PP), polyester, expanded polytetrafluoroethylene (ePTFE) and, more recently, polyvinylidene fluoride (PVDF). All the synthetic meshes are made of a polymeric fiber and their mechanical properties depend on both the material and the textile structure (Tab.1). Examples of possible textures of different commercially available surgical meshes are reported in Figure 1.

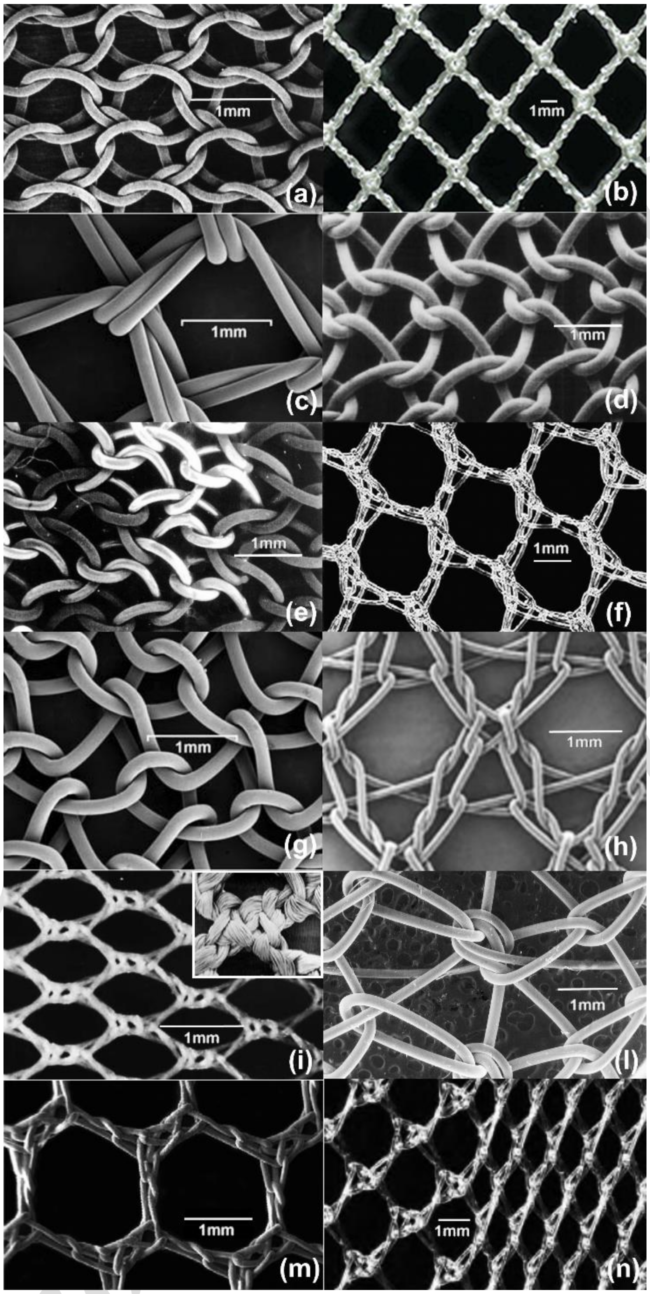

Figure 1 Textile structure of twelve commercially available synthetic meshes: Marlex® (a), Vypro (b), Prolene® (c), ProliteTM (d), Trelex® (e), Optilene® (f), SurgiPro® (g), Parietene® (h); Mersilene (i), Dynamesh IPOM (l), Infinit® (m); Dynamesh ENDOLAP (n) [6].

Polypropylene is synthetized by the polymerization of propylene and it is widely used for surgical mesh manufacturing because of its versatility. It is characterized by a high chemical resistance, burst strength and stretchability, high stress crack resistance and good stiffness and flexural retention. It presents fundamental properties to be used as an implantable material: it is biocompatible, hydrophobic, inert. Further, it shows a high resistance to biologic degradation highlighting a very scarce interaction with tissues enzymes [7]. The choice of PP in meshes manufacturing is also due to its contained cost coupled with its positive interaction when implanted allowing a strong tissues ingrowth and showing a strong durability over time [6]. According to mesh density they are classified into lightweight (LW), medium-weight (MW) and heavyweight (HW) when the density value is below 50 g/m^2, in the interval of 50 g/m^2 and 80 g/m^2, or above 80 g/m^2 respectively [6,8-10]. Among these, the LW density meshes are preferred to the other ones because of their flexibility which allows a better prostheses integration minimizing the inflammatory response and granulomas formation [6].

Polyesters are obtained by the synthesis reaction of alcohol with carboxylic acid. They are polymers characterized by the presence of the ester functional group in their main chain. Polyesters show a high degree of biocompatibility, they are non absorbable, hydrophilic and durable showing a good resistance to most chemicals [6].

Expanded polytetrafluoroethylene (ePTFE) is obtained by free-radical polymerization of tetrafluorethylene and it belongs to the category of the synthetic fluoropolymers. It shows high chemical and mechanical stability and it is not subjected to degradation when in contact with biological fluids. It is hydrophobic and it seems to provoke minimal inflammation reactions with a good resistance to infection [11].

Finally, Polyvinylidene fluoride (PVDF) is produced by the polymerization of vinylidene difluoride and it belongs to the category of the thermoplastic fluoropolymer. It is resistant to hydrolysis and degradation showing a good biostability, a low bending stiffness coupled with a minimum tissue reaction. It is one of the more recent materials used in meshes manufacturing and there are very few studies about its characterization even if the data at disposal confirm its suitability as biomaterial for prosthetic implants [12].

1.2.1 Meshes manufacturing

Synthetic meshes are usually manufactured starting from different kinds of polymeric fibers, whose arrangement determines the mechanical properties of the mesh itself. The fibers can be woven or knitted. Woven meshes contain fibers that are lined in parallel along a direction (i.e. the warp direction) while a second set of aligned fibers (i.e. the weft) pass through the first perpendicularly and, alternatively, over and under [6]. Because of the fabrication technique, these meshes are tightly packed and characterized by small pore size. Further, they usually show isotropic characteristics, since they have almost the same mechanical properties in the weft and warp directions [6].

Knitted meshes are manufactured by interlacing one or more fibers one-by-one, leading to a complex topology. A knitted fiber usually follows a looped path, in which the loops of one row have all been pulled through the loops of the row below it. Because of this peculiar structure, knitted meshes generally show anisotropic characteristics and vary in flexibility and membrane stiffness depending on the orientation [6]. Making a comparison with woven meshes, knitted meshes are generally more porous, flexible and weaker depending of textile conformation. Most of currently available prosthetics are actually knitted.

Different degrees of anisotropy can be achieved in meshes manufacturing by varying the textile processing and the texture itself. However the directions of anisotropy are often not indicated and, consequently, the positioning of the mesh during the surgery doesn’t reflect this information.

1.2.1.1 Meshes porosity and anisotropy

Two parameters are considered for the evaluation of mesh performances: porosity and anisotropy [6]. The porosity, defined as the ratio of pore area to the mesh total area, plays a fundamental role in biomechanical compatibility and tissue regeneration. Indeed, the pore size influences the possibility of bacteria colonization and host tissues ingrowth. When the pore size is too small (less than 10 μm) the mesh is more subjected to bacteria colonization which cannot be eliminated by neutrophils and macrophages greater in dimensions than the pore size. For the same reason the pore size should be large enough (greater than 75 μm) to allow the ingrowth host tissue and the neo-vascularization of the implant, reducing the physiological rejection response [13]. The anisotropy of the mesh is another essential parameter that has to be taken into consideration with the purpose to ensure the biomechanical compatibility with biological tissues that show an anisotropic behavior depending on their mechanical action.

1.2.2 Mechanical properties and testing procedures

It is known that mechanical properties of prosthetic implant represent a crucial factor in the determination of their performances. In the past, the attention was primarily focused on load to rupture and on the implant strength with the only requirements that the implant adequately supported the physiological loads. Then, it came to light that the consideration of only these parameters was not enough for an exhaustive evaluation of the prosthetics suitability. The deformation behavior represents another important parameter, which is now being considered because of the evidence that an excessive stiffness of the implants is associated with the occurrence of clinical complications [14]. Materials that present high stiffness compared to those of surrounding biological tissues are related with tissue erosion and exposure and with postoperative pain and discomforts [14]. On the other hand, too low mesh stiffness shows a poor supportive function [6]. These considerations introduce the importance of the concept of the evaluation of the tissue-implant interface, which plays a fundamental role in all biomaterial interaction. A mismatch between implant and tissues mechanical and anisotropic properties leads to inappropriate transmission of loads at the interface, causing the implant untimely endangerment associated to complications and recurrence risk [15]. Therefore, aiming to assess the necessary biomechanical compatibility and to help the selection of suitable implants, mechanical tests on prosthetics are required for the evaluation of tensile strength, stiffness, elastic and viscoelastic behavior, anisotropy and shrinkage.

At present, there is a lack in the legislation about the certification of synthetic surgical meshes. The International Organization for Standardization (ISO) and the American Society for Testing and Materials (ASTM International) have not yet pointed out specific standards and norms for prosthetics that are actually tested referring to existing standards for textile industry. Literature reports attempts to standardize the terminology and the techniques related to physical as well as biomechanical evaluation of surgical meshes [16, 17], suggesting the adoption of standardized mechanical tests as suture retention strength testing, tear resistance testing, uni-axial tensile testing, bi-axial testing and ball bursts testing.

1.2.2.1 Suture retention strength test

In this kind of mechanical test the sample has one extremity clamped into a grip while in the other extremity a standard wire is placed and pulled. The evaluated parameter consists in the peak force measured during the pulling process up to breakage. It measures the ability of the mesh to retain the suture and it represents an important parameter that has to be evaluated in preventing the failure of the implant by aneurysmal dilatation and rupture.

Figure 2 Suture retention testing [16].

1.2.2.2 Tear resistance testing

This mechanical test evaluates the resistance of a material to the propagation of a tear. During this test a standard tear is obtained by cutting the sample at one extremity to form two tabs. Each of the two tabs is clamped in a grip and the tensile test is performed by moving the grips in opposite directions. The peak force, the tearing force and the tearing strength are measured. The tear strength is recorder as the maximum load sustained by the mesh [16].

Figure 3 Tear resistance testing [16].

1.2.2.3 Uni-axial tensile testing

Dog bone shape specimen of standard dimensions are cut along different directions on the mesh according to the mesh orientation interstice with the aim to assess mesh anisotropic characteristics. Each specimen has one extremity clamped in a grip and it is tested in tension by means of a constant strain rate until mesh failure [16]. Stress-strain curves are obtained by dividing the recorded load by the specimen cross-sectional area against nominal strain. This kind of test allows to determine the ultimate tensile stress and strength and permits considerations about anisotropic characteristics of meshes.

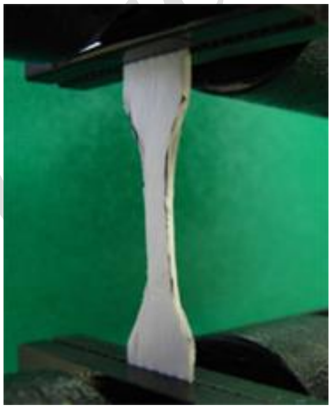

Figure 4 Uni-axial tensile testing [16].

1.2.2.4 Biaxial tensile testing

Biaxial tensile tests add additional information to simple uni-axial mechanical tests and they are adopted in order to reproduce a more physiological loading condition for implanted prosthetics, which is effectively multi-axial. Specimens are cut in standard cruciform shape and then tested along two perpendicular directions by applying the same loading conditions in both the directions (equi-biaxial tensile testing), or by loading the specimen differently along the above-mentioned directions (biaxial tensile testing) [6]. These kind of tests supply also useful information about anisotropic characteristics of meshes.

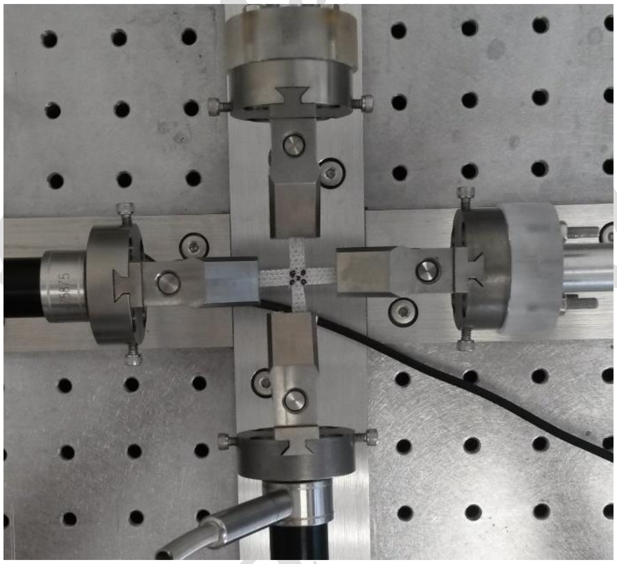

Figure 5 Biaxial tensile testing.

1.2.2.5 Ball burst testing

The specimen is clamped into two standard and circular stainless steel rings to prevent slipping during test. A standard stainless steel ball is then applied in compression at a constant rate up to mesh rupture. The evaluated parameters consist in the maximum force (bursting force) and the bursting index, calculated as the ratio between the bursting force and the mesh density, letting possible the evaluation of the mesh global mechanical response [6]. The ultimate tensile stress and strain are usually reported in terms of force for unit width and nominal strain [16].

Figure 6 Ball burst testing [16].

Table 1 groups a number of commercially available synthetic surgical meshes reporting their principal features: chemical composition, commercial name, manufacturer, pore size, density, thickness, tensile strength and the elastic modulus [6].

As reported, there are several commercially available synthetic surgical meshes with different mechanical properties and anisotropic characteristics. The best solution has not been identified yet, being strongly dependent on the specific kind of surgical intervention.

Chemical composition	**Commercial name**	**Manufacturer**	**Pore size [mm]**	**Density [g/m^2]**	**Thickness [mm]**	**Tensile strength$^{(a)}$ [N/cm]**	**Elastic modulus$^{(a)}$ [N/mm]**
HW PP	Marlex® Bard® Mesh	Bard	0.1 - 0.8	95	0.65	59 100 (l); 64 (t)	-
	Prolene®	Ethicon	1 - 2	109	0.6 mm	90	3.6 (l); 1.1 (t)
	Trelex®	Boston Scientific	0.6	95	-	-	7.7 (l); 3.3 (t)
	SurgiPro®	Covidien	0.5	84	0.57	39 (l); 47 (t)	1.3 (l); 1.4 (t)
LW PP	Vypro	Ethicon	3 - 5	27	0.4	16	-
	ProLite™	Atrium Medical Corp.	0.8 - 1	48	0.5	56	6.0 (l); 2.5 (t)
	Bard® Soft Mesh	Bard	2.4	-	0.69		
	Optilene®	B. Braun	2.8	84	0.53	-	-
	Parietene®	Sofradim	1.1	-	-	39 (l); 27 (t)	0.9 (l); 0.7 (t)
PET	Mersilene™	Ethicon	0.6 - 1	40	0.25 mm	19.5	1.17
ePTFE	Infinit®	WL Gore	2	70	-	-	19.4 (l); 1.0 (t)
PVDF	Dynamesh IPOM®	FEG Textiltechnik	-	-	-	11 (l); 47 (t)	0.3 (l); 1.9 (t)
	Dynamesh ENDOLAP®	FEG Textiltechnik	-	-	-	-	0.3 2.9 (b)

Table 1 Some studies (a) tested the specimens along two mutual orthogonal directions here indicated as longitudinal (l) and transversal (t). Data are reported for uniaxial tensile tests if not specified and for biaxial tensile tests (b) [7].

1.3 Biological meshes

Biological prostheses are obtained from collagen-rich tissues as skin, pericardium, intestinal submucosa and fascial tissues all belonging to the category of the connective tissues.

1.3.1 Connective tissues: composition and biomechanical functions

Connective tissues provide for a variety of functions, they play a fundamental role in mechanical support, movement, tissue fluid transport, cell migration, wound healing, and control of metabolic processes in other tissues. Their properties are determined primarily by the type, the amount, and the arrangement of the extracellular matrix (ECM), which mainly consists of 3 types of macromolecules: fibers, proteoglycans (PGs), and glycoproteins, each of which is synthesized and maintained by cells specific to the tissue type [18].

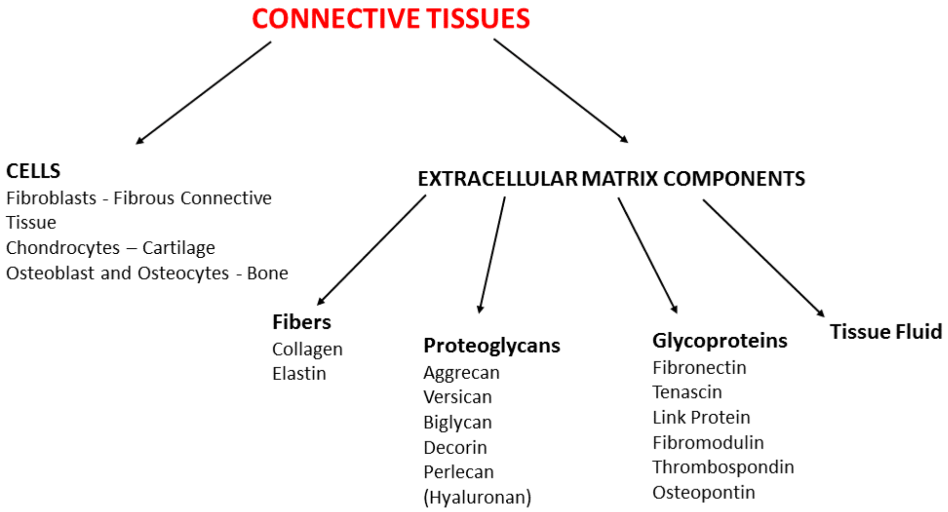

Figure 7 Principal components of connective tissue.

The fibrous components of the ECM are represented by collagen and elastin that are insoluble macromolecular proteins. Collagen presents a variety of forms and its main feature consists in its ability to resist tensile loads. In general, collagens show minimal elongation (less than 10%)

under tension. A proportion of this elongation is due to the straightening of fibers that are packed in various 3-dimensional arrays and it is not the result of true elongation of individual fibers. On the other hand, elastic fibers can increase their length by 150%, yet still return to their undeformed configuration [18].

The second component of the ECM is represented by the Proteoglycans (PGs), a group of soluble macromolecules that have both metabolic and structural roles. PGs occupy, with collagen, the interstitial spaces between the cells and attach to cell surfaces where they act as receptors. PGs play important mechanical functions including stabilization of collagen networks, hydration of the matrix, and the ability to resist to compressive forces, that is best exhibited by the PGs of articular cartilage. Hyaluronan (HA), is particularly important because it entrains large amounts of water and is abundant in hydrated soft loose tissues where repeated movement is required (eg, tendon sheaths and bursae) [18].

The third component of matrix molecules is represented by the glycoproteins that are ubiquitous in all CTs and have both metabolic and structural roles. Glycoproteins mechanical actions include providing linkage between matrix components and between matrix components and cells.

It comes to light that the mechanical properties of all the connective tissues, such as the ability to resist tension, compression, extensibility, and torsion, are determined by the proportions of the matrix components [18].

1.3.1.1 Collagens

Nineteen different types of collagens are recognized, all with individual and peculiar characteristics that serve specific functions in a variety of tissues. The common structural feature to all these collagen types is a triple helix region within the molecule. This section of the molecule provides the characteristic mechanical properties to withstand tensile loads which is typical of tendons and ligaments. The triple helix is made up of 3 polypeptide chains folded to form a ropelike coil. Each chain, called α-chain, is characterized by repeating sequences of 3 amino acids, glycine-X-Y. (Fig. 8). Specific collagen types are composed by a variety of α-chains and by variations in the combination of these latter. The helical complex, which resists tension, is further strengthened by intermolecular bonds between the α-chains of adjacent molecules [18].

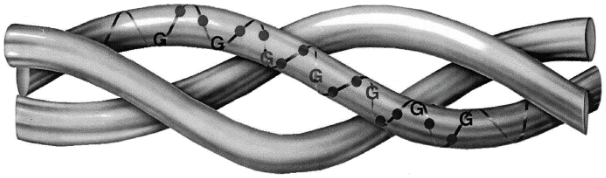

Figure 8 Collagen triple helix composed by the coil of three individual alpha chains. Within each chain, the amino acids are similarly arranged in a helix, with glycine (G) facing the center of the triple helix [18].

1.3.1.2 Elastin

Elastic fibers in the ECM allow tissues to withstand repeated stretching and deformation and to return to a relaxed initial state. The arrangement of elastin varies and depends on the strength and direction of forces acting on the tissue. The fibers may be organized in different ways depending on the type of tissue. In general, elastin contains two amino acids, the desmosine and the isodesmosine, which form cross-linkages between adjacent tropoelastin chains and are important in appointing the elastic properties to elastin (Fig. 9). The quantity of elastin found within the tissue usually reflects the amount of mechanical strain imposed on it and the requirement for reversible deformation [18].

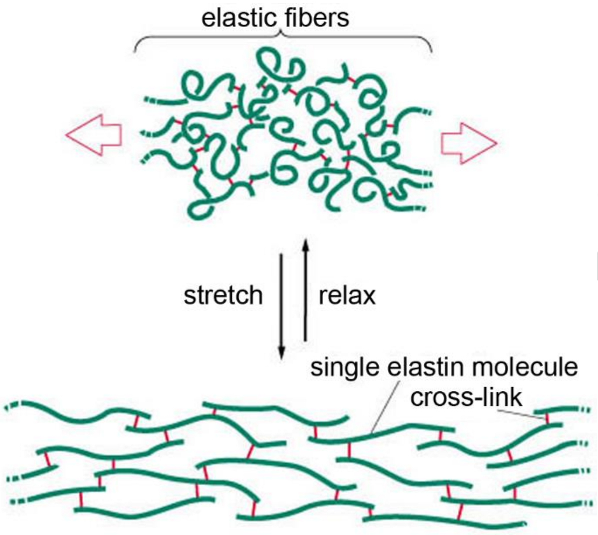

Figure 9 Structural composition of elastin and the exemplification of its mechanical behavior under uni-axial stretching. Because each elastin molecule in the network can expand and contracts as a random coil, the entire network can stretch and recoil like a rubber.

1.3.1.3 Proteoglycans

The Proteoglycans are characterized by a core protein covalently attached to one or more sulphated glycosaminoglycan (GAG) side chains. The core proteins are specific to each of the PG types showing a certain degree of variability in size. Similarly, there are various GAG chains that are composed of repeating disaccharide units, whose type and number determine the properties of the PG. All GAGs are negatively charged and attract ions, creating an osmotic imbalance that results in the PG-GAG absorbing water from surrounding areas [18]. This action helps to maintain the hydration of the matrix. The percentage of GAG within connective tissues varies depending on mechanical load: tissues that are subjected to compressive forces, as in articular cartilage, show a large PG content (about 10% of the dry weight of the tissue). On the other hand, in tension-resisting tissues such as tendons and ligaments, PGs are found in small concentrations (about 0.2% of dry weight) [18]. Further, PGs play a role in regulating cell activity, in acting as a co-receptor providing support, in assisting cellular differentiation. Among the PGs: aggrecan, versican, biglycan, decorin, perlecan, hyaluronan.

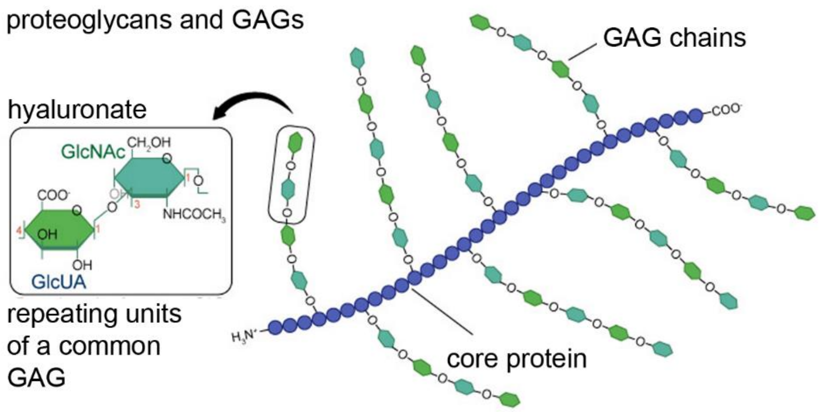

Figure 10 Common structure of PGs and GAG.

1.3.1.4 Glycoproteins

Glycoprotein are soluble, multifunctional, multidomain macromolecules. They are integral to stabilizing the surrounding matrix and linking the matrix to the cell without performing mechanical functions. They are involved in the regulation of many functions, as enhancing cell motility, producing changes in cell shape, and stimulating cell proliferation and differentiation. They are also involved in the modulation of cell attachment to matrix component and in the stabilization of PG aggregates. Among the glycoproteins: fibronectin, tenascin, laminin, link protein, thrombospondin, osteopontin, and fibromodulin [18].

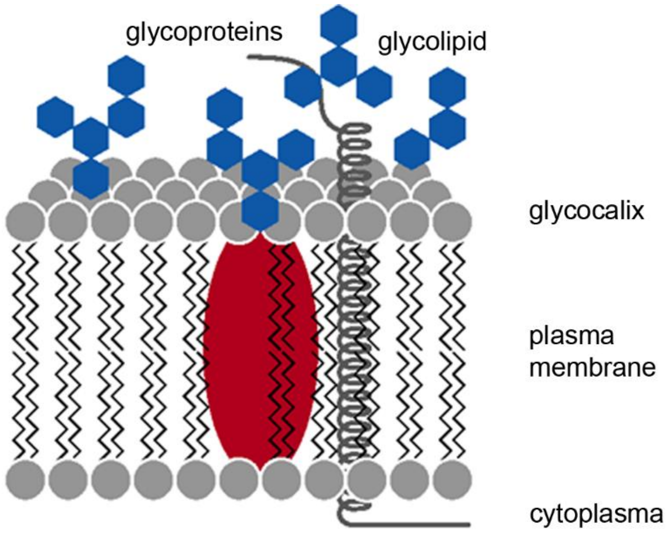

Figure 11 Example of structure and location of glycoproteins in the membrane cells.

1.3.2 Biomeshes processing

Biological tissues are treated to remove fat deposits, hair follicles, sweat glands and cells through decellularization processes, obtaining a scaffold mostly composed by collagen and elastin [19]. In spite of these treatments, source of growth factors remain in the structure attracting endothelial cells and, consequently, fibroblast, which release additional chemoattractors that regulate the migration of other structural cells. The three-dimensional structure and the physiological porosity of the biological scaffold promote tissue ingrowth while, at the same time, the mesh degrades in the remodeling processes [20]. Decellularization procedures could be followed by additional manipulations: some implants can be dried or lyophilized for storage. These processes can have consequences on mesh properties by varying the pore size as well as the rehydration rate that influences the infiltration and the vascularization capacity of the implant by the host [21]. An additional possible treatment consists in manipulations with chemical reagents interacting with specific functional groups, creating cross-links that give stability to the collagen and leading to an improvement of mesh durability by delaying the scaffold degradation [3]. Most of these products undergo to sterilization processes that include gamma radiation, ethylene oxide, or hydrogen peroxide with the aim to remove virus and bacteria and to supply a safe material. The advantage, with respect to synthetic materials, consists in avoiding acute and/or chronic infection and chronic inflammation. Further, biomeshes induce a minimal inflammatory response, minimal adhesion formation and low risk of infection in contaminated or potentially contaminated situation [21].

Depending on the origin of the graft it is possible to identify two kinds of biomeshes: xenografts, that are from animal derivation, and allografts, usually derived from humans. Xenografts are derived from mammalian tissues, including dermis, pericardium and small intestinal submucosa; they usually originate from bovine and porcine sources. Allografts are mainly derived from skin and fascial tissues and most of them are aseptically processed and treated with antibiotics. The physical and the mechanical properties of all these materials depend on the tissue source and on the method of processing, crosslinking and sterilization. The physical dimensions of the final device are strongly related with those of the source material: tissues like Permacol™ or SurgiMend®, that are derived from porcine and bovine dermis, are available in sheets up to 25 by 40 cm, while human equivalents are smaller in sizes, with consequences on the possible applications. The thickness of biological grafts ranges from about 0.5 mm to 4 mm and it is directly related to material mechanical properties because thicker materials show an increased load-carrying capacity [22]. The greater advantage of these prosthetics consists in their ability to supply a reinforcement action without the stress-shielding or the material property mismatch problems usually associated with synthetics that are often orders of magnitude stiffer than native tissues [22]. There are several typologies of commercially available biomeshes that differ for their origin and for the undergone manufacturing processes that lead to materials with specific mechanical features whose suitability has to be evaluated in correlation with the specific surgical procedure (Table 2).

Brand Name	Company	Type	Source	Crosslinking	Sterilization	Thickness [mm]	Tensile strength(a) [MPa]	Bursting force [N/cm]
Alloderm®	LifeCell	Dermis	Human	No	No	2.02 ± 0.041	20.32 ± 0.84	1028 ± 199.1
Allomax™	CR Bard	Dermis	Human	No	Yes	1.29 ± 0.036	14.36 ± 0.82	290.8 ± 58.28
Collamend™	CR Bard	Dermis	Porcine	Yes	Yes	1.22 ± 0.013	11.48 ± 1.75	110.3 ± 7.8
FlexHD™	MTF	Dermis	Human	No	No	1.15 ± 0.043	14.36 ± 2.66	929.5 ± 193.9
Periguard®	Synovis	Pericardium	Bovine	Yes	Yes	0.47 ± 0.027	21.51 ± 1.59	99.05 ± 16.75
Permacol™	Covidien	Dermis	Porcine	Yes	Yes	0.91 ± 0.008	8.22 ± 1.38	66.23 ± 10.82
Strattice®	LifeCell	Dermis	Porcine	No	Yes	1.76 ± 0.012	9.92 ± 1.14	270.5 ±48.91
Surgimend®	TEI	Dermis	Bovine fetal	No	Yes	1, 2, 3 or 4 mm	20.00	-
Surgisis®	Cook	Intestinal submucosa	Porcine	No	Yes	1.37 ± 0.036	2.53 ± 0.25	200 ± 4.74
Veritas®	Synovis	Pericardium	Bovine	No	Yes	0.8 ± 0.017	9.38 ± 1.92	128.6 ± 8.52
XenMatrix™	CR Bard	Dermis	Porcine	Yes	Yes	1.95 ± 0.012	11.95 ± 0.8	377 ± 41.34

Table 2 Commonly available biological meshes: a comparison of the principal characteristics.

1.3.3 Allograft from fascial system

Within the biological meshes, particular attention is paid to allografts from human fascial system that are commonly used in several reconstructive surgical interventions. As matter of example, grafts of human fascia lata are widely exploited in the abdominal wall repair which represent the best known application of this prosthetics. Fascia lata is successfully used also for the substitutions of part of vessels and heart valves reconstruction in cardiac surgery [23], in the reconstruction of tendons and ligaments [24], in the correction of the pelvic organ prolapse in uro-gynecologic interventions [25] and in facial surgery [26]. Allografts are obtained, upon agreement, from expired patients that meet donor criteria. The tissues undergo different kinds of processing following the general step by step procedure above described for the biomeshes manufacturing. Finally grafts from fascial system are frozen to minus eighty degrees Celsius and stored in special commercial freezers that maintain those temperatures where they can last for approximately five years.

An in-depth analysis, as pertains the mechanical characteristics of the human fascial system, is therefore of interest aiming to understand its biomechanical role in relation with its histological and morphometrical conformation. Further, the investigation of its mechanical properties will help in the choice of its best use as allograft source for specific surgical procedures.

1.3.3.1 The fascial system: histological analysis

Within the fascial system it is possible to describe two different structures: the superficial fascia and the deep fascia known also as fascia profunda.

The superficial fascia is a structure composed by fibroelastic tissue that divides the hypodermis into two distinct layers: the superficial and the deep layers. The superficial layer is interposed between the dermis and the superficial fascia. It is inside the retinaculum cutis superficialis, formed by vertical septa, and the subcutaneous adipose tissue. The deep layer is interposed between the superficial and deep fasciae. It is composed by loose connective tissue and adipose cells. Within the deep layer there are oblique septa forming the retinaculum cutis profondus [27].

More attention is given to the deep fascia of the human fascial system that is a connective tissue composed of two or three dense layers of parallel collagen fibers bundles (Fig. 13a). The number of the layers depends on the considered anatomical region. The collagen fibers show an undulating arrangement, which is a common feature of all the connective tissues. Each dense connective tissue layer is separated from the adjacent one by a thinner layer of loose connective tissue that allows the mutual sliding between different strata [27].

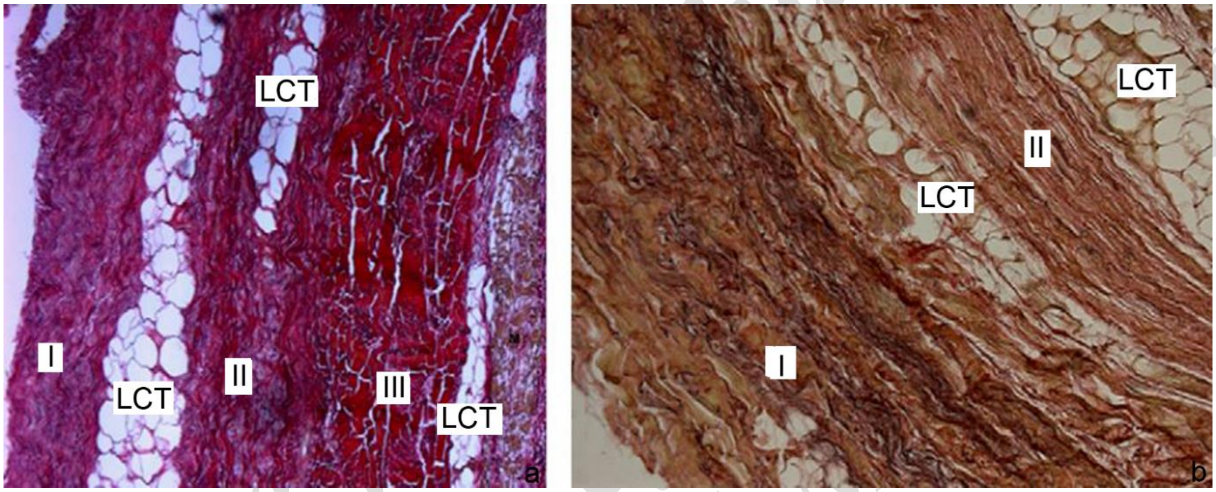

Figure 12 Both the crural fascia, on the left, and the brachial fascia, on the right are composed of different layers of collagen fiber bundles separated by a thin layer of loose connective tissue (LCT) [27].

Adjacent layers show different orientations of their collagen fibers and, even in this case, the angle between the fibers depends on the specific anatomical region and reflects the mechanical action required to the tissue (Fig. 13b). In general it is possible to observe that this type of multi-layered structure permits a certain degree of stretch plus a capacity to recoil and ensures that the deep fascia response to loading varies according to direction. Further, this particular structural conformation leads to a complex mechanical response of these tissues, which includes nonlinear and anisotropic stress-strain behavior.

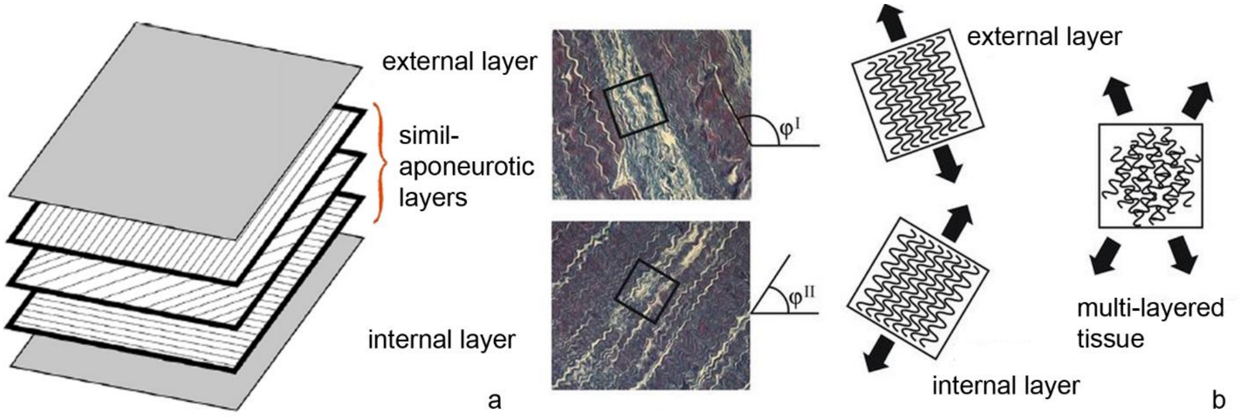

Figure 13 Schematization of the deep fasciae: the internal and external dense layers and the interposed median layers with an aponeurotic aspect [27] (a). Schematization of the multi-layered and fiber-reinforced structure of the fascia[28] (b).

In the deep fascia it is highlighted the presence of many elastic fibers. Further, fascia is richly innervated, and abundant free and encapsulated nerve endings are recognized (including Ruffini and Pacinian corpuscles). Some of the nerve fibers, mainly present around the vessels, are adrenergic and are involved in controlling local blood flow. Other fibers as free nerve endings, Ruffini and Pacinian corpuscles may have a role in proprioceptive functions [29].

1.3.3.2 The fascial system: functions and biomechanical role

The deep fascia, spanning the whole body, contains and separates groups of muscles into well-defined spaces called compartments. The deep fascia plays also an integration role of these compartments being able to transmit tension, generated by muscles, at a distance, connecting different segments of the body, participating in peripheral motor coordination. Each segment of the limbs has its own characteristic compartments that separate functional groups of muscles with distinctive embryological origins, blood and nerve supplies. The compartments are usually named according to the actions of their contained muscles (flexors, extensors, evertors, adductors) or according to their anatomical position (anterior, posterior, medial, lateral) [29].

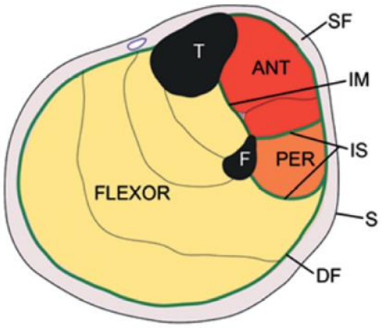

Figure 14 Schematization of a transverse thigh section showing the relative positions of the superficial (SF) and deep fascia (DF) in relation to the skin (S) and muscles. The deep fascia, in association with the bones (tibia T and fibula F) and intermuscular septa (IS) forms a series of compartments: peroneal (PER), flexor (FLEXOR) and anterior compartment (ANT). IM represents the interosseous membrane [29].

The fascial intermuscular septa are usually attached to periosteum and act as a connection between fascial tissues and bone structures. It is possible to observe different degrees of interaction between the fascia and the underlying enwrapped muscles depending on the number of myofascial expansions, on the density of intramuscular septa and on the number of muscle fibers that, inserting on the fascia, keep firmly attached the muscular and fascial components. According to the anatomical investigated region it is possible to recognize morphological and functional differences in the deep fascia. As matter of example, it is possible to compare the pectoral fascia to the fascia lata of thigh: the first one appears as a thin lamina, strongly adherent to the muscle, while the second one appears as a thick, whitish layer of connective tissue, similar to an aponeurosis, increasing in thickness in a proximal to distal direction [30]. Further, it is possible to observe an almost complete fusion between the pectoral fascia and the underlying pectoral major muscle (Fig. 15a), while an almost complete independence is highlighted between fascia lata and the thigh muscles (Fig. 15b).

Figure 15 Different muscles expansions are evident between the pectoral major muscle on the right and its fibrous expansions extended into the ipsilateral and contralateral rectus abdominis sheaths (a). Fascia lata that appears to be easily separable from all the muscles of the thigh (b) [30].

The observed different relationships between deep fasciae and muscles suggest that fascial tissues are stretched in a more precise manner in the pectoral fascia than in the fascia lata, with different activation of the proprioceptors embedded in the tissues. The strong relationship between the deep muscular fascia and muscles could give evidence of the deep fascia importance in the peripheral motor coordination and dynamic proprioception [30].

Another important function of deep fascia in the limbs consists in its capacity to act as a restraining envelope for muscles lying deep to them. When these muscles contract against a thick and resistant fascia, the thin-walled veins and lymphatics within the muscles are squeezed and their unidirectional valves ensure that blood and lymph are directed towards the heart according to fascia an important role in helping blood circulation [29].

All these features make the deep fascia structure a complex and active system playing a fundamental role in a number of physiological tasks. Further, the above mentioned characteristics can have consequences that should be considered in the use of these tissues as substitutes.

CHAPTER 2 MECHANICAL CHARACTERIZATION OF SOFT CONNECTIVE TISSUES

2.1 Introduction

The biomechanical characterization of soft tissues consists in the correlation of the tissue structure with a suitable numerical model. This is performed by following a step by step procedure whose schematization is reported in Figure 16.

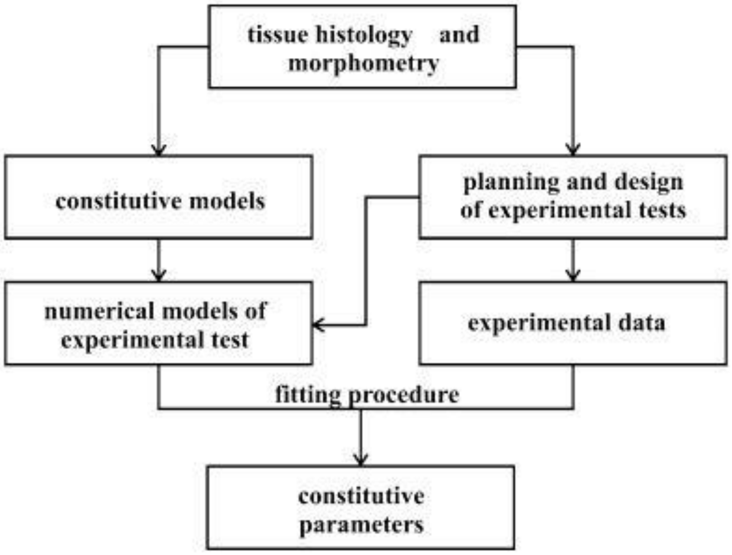

Figure 16 Definition of a constitutive model and adaptation to experimental data [31].

Starting from anatomical results, the functional behavior of soft connective tissues is considered, from a mechanical point of view, at the scale level of the tissue by means of a phenomenological constitutive model. This approach considers the tissue as a homogeneous material whose macroscopic behavior (expressed in terms of strength, stiffness, etc.) is the result of complex mechanical responses of the different tissue subcomponents and of their interaction phenomena.

Further, soft tissues are in general anisotropic materials, because of the presence of collagen fibers having specific spatial orientation that appoints to the tissue a mechanical response depending on the loading direction. For this reason, with the aim to ensure a characteristic of micromechanical consistency, a constitutive model have to be defined according to the evaluation of the tissue microstructural conformation by means of accurate histomorphometric analyses. The typical mechanical response of a tissue reinforced by fibers is a progressive increase of stiffness with strain, which is related to the crimped conformation of the fibers within the unloaded tissue [31]. A qualitative example of the anisotropic mechanical response to a uni-axial tensile condition of a tissue reinforced by a family of collage fibers is reported in Figure 17.

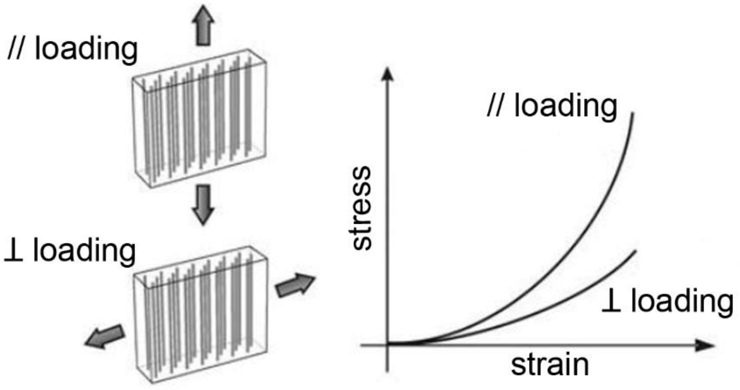

Figure 17 Loading of a sample in direction aligned and perpendicular to the collagen fibers and consequent qualitative mechanical response in terms of stress versus strain [31].

The structural characteristics of the tissue are interpreted by means of the definition of an appropriate constitutive model, which depends on a number of constitutive parameters. On these basis it is possible to plan the number and the type of the mechanical tests. Then, the comparison between the experimental data and the numerical results obtained via simulated tests, based on the hypothesized model, allows to fit the constitutive model to the effective tissue mechanical behavior.

2.2 General constitutive formulation for connective tissues

The constitutive model of a material describes the relationship between stress and strain history by means of a specific mathematical formulation. Starting from a deep knowledge of the material microstructural conformation it is possible to define suitable constitutive laws that properly describe its mechanical behavior. For the discussion of material behavior and properties it is fundamental the concept of objectivity that leads to the principle of material frame indifference, which affirms that the material properties must be independent of observer (condition of material objectivity). The second aspect that has to be taken into consideration deals with the symmetry properties of a material body that are used for a classification of the material body itself. The conditions of material symmetry and material objectivity represents the two major considerations in deducing the restrictions imposed on constitutive equations for a given class of materials. Furthermore, constitutive theories of materials are completed with thermodynamic considerations. The entropy principle of continuum thermodynamics requires that constitutive laws are consistent with the entropy inequality for any thermodynamic process, leading to an imposition of additional restrictions on constitutive equations.

2.2.1 Formulation of constitutive models for biomeshes

In modeling soft tissue the characteristics due to their structural conformation entail large deformations and displacements, with high non-linearity, time dependent behavior and strong anisotropic characteristics [32]. Soft tissues are usually modeled by means of an almost incompressible ground matrix reinforced by embedded collagen fibers whose local distribution establishes peculiar material symmetry characteristics [33]. The presence and the orientation of the collagen fibers are responsible of the strong non-linear behavior of these tissues undergoing different loading conditions. This characteristic can be modeled, in a first approximation, by means of hyperelastic formulations that describe the tissue first instantaneous response. The internal rearrangements of the material structural conformation, due to external mechanical actions, develop over time until the achievement of a thermodynamic balance state. This time-dependent behavior of soft tissue must be described by means of specific visco-hyperelastic formulations [32].

The second principle of the thermodynamics affirms that, during a generic mechanical action on a body, the work of the internal stresses must be higher or equal to the energy which is reversibly stored within the material. This means that the mechanical energy that can be given back by a material is at least equal, as in the case of hyperelastic materials, to the mechanical work developed on the material itself. This entail a general dissipative behavior of materials in which, part of the performed mechanical work is dissipated in heat or in irreversible changes of their structural conformation through damage, viscous and plastic phenomena. This concept is formalized by means of the Clausius-Duhem dissipative inequality [34]:

$$D_{\text{int}} = \frac{1}{2}\mathbf{S} : \dot{\mathbf{C}} - \dot{\psi} \geq 0 \tag{2.1}$$

D_{int} represents the rate of the internal dissipation, **S** is the second Piola-Kirchhoff stress tensor, **C** represents the right Cauchy-Green strain tensor and ψ is the Helmholtz free energy function. This latter expresses the fraction of the work, developed by the internal stresses, that is stored within the material point in a reversible way specifying its current mechanical state. In general, the mechanical state of a material point is determined by its strain history. This implies that the Helmholtz free energy function depends both on the current strain state and on dissipation phenomena that develop during the strain history:

$$\psi = \psi\left(\mathbf{C}, \mathbf{x}^{i}\right) \tag{2.2}$$

being $\mathbf{x}^{\mathbf{i}}$ the internal variables associated to the development of dissipation phenomena. Starting from equation (2.1) and (2.2) it is possible to define the rate of the internal dissipation as follow:

$$D_{\text{int}} = \left(\frac{1}{2}\mathbf{S} - \frac{\partial \psi}{\partial \mathbf{C}}\right) : \dot{\mathbf{C}} - \frac{\partial \psi}{\partial \mathbf{x}^i} \cdot \dot{\mathbf{x}}^i \geq 0 \tag{2.3}$$

Inequality 2.3 must always be satisfied $\forall\ \mathbf{C}, \dot{\mathbf{C}}, \mathbf{x}^i, \dot{\mathbf{x}}^i$ according to the principle of universal dissipation, letting possible to express the stress and the rate of internal dissipation as follows:

$$\mathbf{S}\left(\mathbf{C}, \mathbf{x}^i\right) = 2\frac{\partial \psi\left(\mathbf{C}, \mathbf{x}^i\right)}{\partial \mathbf{C}} \tag{2.4}$$

$$D_{\text{int}} = -\frac{\partial \psi}{\partial \mathbf{x}^i} \cdot \dot{\mathbf{x}}^i \geq 0 \tag{2.5}$$

For the definition of the constitutive laws it is necessary to correlate the Helmholtz free energy to the current strain state and to the internal variable whose evolution over time must satisfy inequality 2.5 during the generic stress-strain path. Furthermore, describing the strain state by means of the right Cauchy Green strain tensor **C**, which does not depend on rigid body motions, the principle of frame indifference is satisfied [35].

2.2.2 Material symmetry

In general, symmetries of the material point structural conformation are reflected by symmetries in its mechanical properties. Material symmetries are characterized by symmetry groups $\mathcal{G}_{\mathbf{Q}}$ that impose restrictions on the form of the strain energy function. Any orthogonal transformation member of the symmetry group of the material does not produce any change on the strain energy function when applied to the material in the natural state (prior any deformation process) [36].

A material shows an isotropic behaviour when the sub-components of the material point are equally distributed and its mechanical properties result to be independent with respect to any specific direction. In this particular case the Helmholtz free energy function have an isotropic behaviour and the definition of the current strain state can be achieved by means of the three principal invariants of the right Cauchy-Green strain tensor defined as follow [34]:

$$I_1 = tr(\mathbf{C}),\ I_2 = 1/2\left[I_1^2 - tr\left(\mathbf{C}^2\right)\right],\ I_3 = J^2 = det(\mathbf{C}) \tag{2.6}$$

being $J = det\ (\mathbf{F})$ the deformation Jacobian and **F** the deformation gradient. This latter is the second order tensor which maps line elements in the reference configuration into line elements (consisting of the same material particles) in the current configuration.

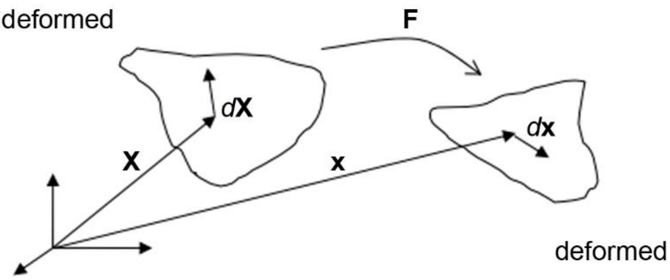

Figure 18 The deformation gradient acting on a line element.

The material point in the current configuration can be expressed as $\mathbf{x} = \boldsymbol{\varphi}(\mathbf{X}, t)$ and the deformation gradient is defined as follow:

$$\boldsymbol{F} = \frac{\partial \boldsymbol{\varphi}(\mathbf{X})}{\partial \mathbf{X}} = \begin{bmatrix} \partial x_1/\partial X_1 & \partial x_1/\partial X_2 & \partial x_1/\partial X_3 \\ \partial x_2/\partial X_1 & \partial x_2/\partial X_2 & \partial x_2/\partial X_3 \\ \partial x_3/\partial X_1 & \partial x_3/\partial X_2 & \partial x_3/\partial X_3 \end{bmatrix} \tag{2.7}$$

If the material sub-components are not equally distributed but follow a preferential direction of distribution, the material behavior is characterized by anisotropy and its mechanical properties change according to the considered direction. As matter of example, in soft biological tissues, the presence of preferentially oriented collagen fibers embedded in an anisotropic ground matrix, appoints strong anisotropic characteristics to these materials [33].

Taking into consideration biological structures as tendons, ligaments and fascial tissues in particular districts, as the plantar fascia, it is possible to observe that the collagen fibers are preferentially oriented along one direction appointing to the material a transversal isotropic symmetry (Fig. 22). Further, it is possible to recognize the fibers distribution in the undeformed configuration which is usually described by means of a unit vector $\mathbf{a}_0$ that is locally tangent to the fibres. The plane β, that is normal to $\mathbf{a}_0$, is the isotropic plane in which the mechanical properties are the same along any considered direction.

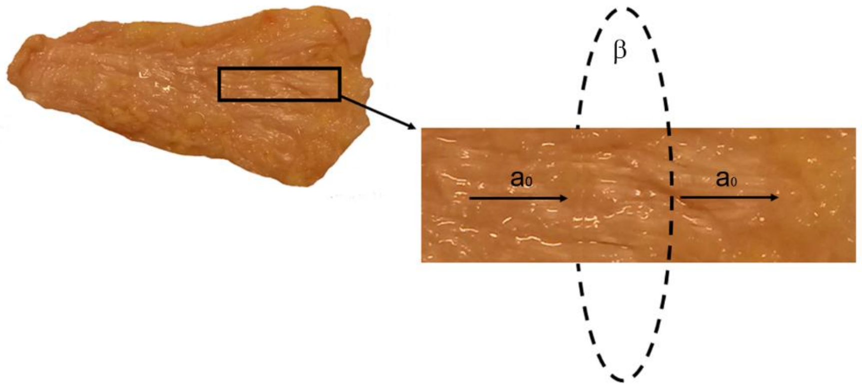

Figure 19 Plantar fascia is a typical example of transversal isotropic fascial tissue. On the right, the magnification allows to recognize the initial disposition of the collagen fibers and the tangent unit vectors a_0 are highlighted. β is the isotropic plane which is normal to a_0.

The group of symmetry is expressed as follow:

$$\mathcal{G}_{\mathbf{Q}} = \left\{ \mathbf{Q} \in Orth^{+} \mid \mathbf{Q}\mathbf{a}_0 = \mathbf{a}_0 \right\} \tag{2.8}$$

and includes the orthogonal transformations around $\mathbf{a}_0$. Exploiting the structural conformation due to the oriented collagen fibres, it is possible to define additional two invariants, called structural invariants, for the description of the current strain state [33]:

$$I_4 = \mathbf{a}_0 \cdot \mathbf{C}\,\mathbf{a}_0 = \lambda^2,\; I_5 = \mathbf{a}_0 \cdot \mathbf{C}^2\,\mathbf{a}_0 \tag{2.9}$$

The physical meaning of these two invariant can ben exemplified by considering a simple shear deformation for two different fibres spatial orientation: in the first configuration fibres are aligned in the share plane (fig. 23a), while in the second configuration fibres are aligned perpendicular to the shear plane (Fig. 23b).

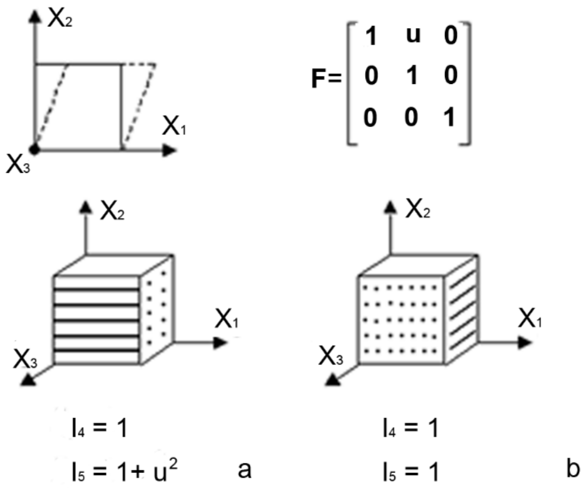

Figure 20 Effects of a pure shear deformation in the plane (X1, X2) on the I4 and I5 in the case of two different alignments of the fibers.

By computing the structural invariants I_4 and I_5 it is possible to see that the fourth invariant is constant in both cases and it expresses the square of stretch along the preferential direction λ, while the fifth invariant varies according to the fibers disposition and can be used to expresses the influence of the shear deformation on the fibers behavior.

More complex fibres distributions and consequently symmetric properties will be taken into account in the specific sections pertaining to crural fascia.

2.2.3 Hyperelastic constitutive models

Hyperelastic constitutive laws are usually used to model materials that show a pure elastic response when subjected to very large strains. They account both for nonlinear material behavior and large shape changes. In other words, hyperelastic materials have an internal dissipation that is always equal to zero for any choice of the stress-strain path, this entails that the rate of the internal dissipation is null [37]:

$$D_{\text{int}} = -\frac{\partial \psi}{\partial \mathbf{x}_i} \cdot \dot{\mathbf{x}}_i = 0 \qquad \forall\ \mathbf{C}, \dot{\mathbf{C}}, \mathbf{x}_i, \dot{\mathbf{x}}_i \tag{2.10}$$

where ψ is the Helmholtz free energy function and $\mathbf{x}_\text{i}$ are the internal variables associated, in this case, to the development of dissipation phenomena. The work of internal stresses results to be independent on the stress-strain path [38] and the Helmholtz free energy function represents a potential of the strain state, usually called strain energy function, which can be expressed as follow:

$$\psi = W(\mathbf{C}) \tag{2.11}$$

Starting from the strain energy function it is possible to compute the stress-strain relation:

$$\mathbf{S}(\mathbf{C}) = 2\frac{\partial W(\mathbf{C})}{\partial \mathbf{C}} \tag{2.12}$$

The specific strain energy function is usually defined accounting for the material structural conformation and experimental data from mechanical tests.

2.2.3.1 Isotropic hyperelastic model

Isotropic hyperelastic material have a strain energy function that must be invariant to reference system. Hence, it can be formulated by means of the three principal invariants of the right Cauchy-Green strain tensor:

$$W(\mathbf{C}) = W(I_1, I_2, I_3) \tag{2.13}$$

It follows that the stress-strain relation can be expressed, by exploiting equations (2.12) and (2.13) as:

$$\mathbf{S} = 2\frac{\partial W}{\partial \mathbf{C}} = 2\sum_{i=1}^{3}\frac{\partial W}{\partial I_i}\frac{\partial I_i}{\partial \mathbf{C}} \tag{2.14}$$

being the derivatives of the principal invariants:

$$\frac{\partial I_1}{\partial \mathbf{C}} = \mathbf{1}, \quad \frac{\partial I_2}{\partial \mathbf{C}} = I_1\mathbf{1} - \mathbf{C}, \quad \frac{\partial I_3}{\partial \mathbf{C}} = I_3\mathbf{C}^{-1} \tag{2.15}$$

where **1** represents the rank two unit tensor.

Most biological soft tissues present a water content of more than 70%. For this reason, they hardly change their volume (isovolumetric) even if load is applied, and they behave like almost incompressible materials [34]. The incompressibility assumption is applicable to most of the biological soft tissues and it has been confirmed experimentally, at least in the tensile state, in a number of studies [33, 39]. The reasonable assumption of the incompressibility leads to a reformulation of the strain energy function and, consequently, of the stress response allowing to split the term related to the response of the isotropic matrix in the sum of two contributions: a volumetric (W_{mv}) and an iso-volumetric (W_{mi} , volume-preserving) part. The strain energy function can be rewritten as:

$$W_m\left(I_1,I_2,I_3\right)=W_{mv}\left(I_3\right)+W_{mi}\left(\tilde{I}_1,\tilde{I}_2\right) \tag{2.16}$$

The modified invariants $\tilde{I}_1,\tilde{I}_2$ are obtained by substituting the right Cauchy-Green strain tensor with its iso-volumetric part, defined as $\tilde{\mathbf{C}} = I_3^{-1/3}\mathbf{C}$.

2.2.3.2 Fiber-reinforced hyperelastic model

Considering the above mentioned example of transversal isotropic symmetry consisting in a tissue reinforced by a family of collagen fibers with a preferential orientation, it is possible to express its strain energy function by means of five invariants: the three principal invariants of the right Cauchy-Green strain tensor and the structural invariants I_4,I_5.

$$W\left(\mathbf{C}\right)=W\left(I_1,I_2,I_3,I_4,I_5\right) \tag{2.17}$$

The number of the invariants and the complexity of the strain energy function increase when considering additional families of collagen fibers reinforcing the tissue.

The stress response is computed as:

$$\mathbf{S}=2\frac{\partial W}{\partial \mathbf{C}}=2\sum_{i=1}^{5}\frac{\partial W}{\partial I_i}\frac{\partial I_i}{\partial \mathbf{C}} \tag{2.18}$$

And the derivatives of the fourth and fifth invariant are computed as follow:

$$\frac{\partial I_4}{\partial \mathbf{C}}=\mathbf{a}_0\otimes\mathbf{a}_0,\ \frac{\partial I_5}{\partial \mathbf{C}}=\mathbf{a}_0\otimes\mathbf{C}\mathbf{a}_0+\mathbf{C}\mathbf{a}_0\otimes\mathbf{a}_0 \tag{2.20}$$

In general, the mechanical behaviour of soft biological tissues is due to the contribution of the mechanical response of the ground matrix (W_m) and of the fibrous components (W_f). This fact allows to consider the strain energy function as the result of an additive contribution of the above mentioned terms:

$$W\left(I_1, I_2, I_3, I_4, I_5\right) = W_m\left(\tilde{I}_1, \tilde{I}_2, I_3\right) + W_f\left(\tilde{I}_4, \tilde{I}_5\right) \tag{2.21}$$

Exploiting the incompressibility constraint it is possible to rewrite (2.21) highlighting the decomposition of the ground matrix response into a volumetric (W_{mv}) and isovolumetric (W_{mi}) part as follow:

$$W\left(I_1, I_2, I_3, I_4, I_5\right) = W_{mv}\left(I_3\right) + W_{mi}\left(\tilde{I}_1, \tilde{I}_2\right) + W_f\left(\tilde{I}_4, \tilde{I}_5\right) \tag{2.22}$$

The same addictive decomposition is reflected in the expression of the stress:

$$\mathbf{S} = \mathbf{S}_{mv} + \mathbf{S}_{mi} + \mathbf{S}_f \tag{2.23}$$

2.2.4 Visco-hyperelastic model

Viscoelastic materials exhibit gradual deformation and recovery when they are subjected to loading and unloading. Polymer plastics and almost all biological materials belong to this particular category of materials whose mechanical response is dependent upon how quickly the load is applied or removed. The extent of the deformation depends on the rate at which the deformation-causing loads are applied. This time-dependent material behavior is called viscoelasticity. The viscosity is a fluid property and is a measure of resistance to flow, while the elasticity is a solid material property. A viscoelastic material possesses both fluid and solid properties. Viscoelastic characteristics depend directly on the development of internal structural conformation rearrangements that develop while the material is loaded. Microstructural rearrangements comprise, as matter of example, fluid fluxes through the solid skeleton or the sliding of macromolecules and can be observed, from a phenomenological point of view, through creep, stress relaxation and hysteresis phenomena. These microstructural rearrangements are usually modeled by means of a suitable number of viscoelastic processes defined by means of internal variables $\mathbf{q}^{\mathbf{i}}$ that characterize the material stress-strain evolution over time. The Helmholtz free energy function can be rewritten, for a visco-hyperelastic material, by taking into consideration the time-dependence:

$$\psi = \psi\left(\mathbf{C}, \mathbf{q}^{i}\right) \tag{2.24}$$

In the study of viscoelasticity, materials are often represented by mechanical models consisting of viscous dashpots and elastic springs. These latter are perfectly linear elastic and massless and are used to represent the elastic behavior, while viscous dashpots describe the fluid behavior extending at a rate proportional to the applied stress divided by the element viscosity [40]. A commonly adopted approach consists in modeling a material viscoelastic behavior by means of the Zener rheological model, which consists in the parallel connection of an equilibrium spring and a suitable number of viscoelastic processes (Fig. 24).

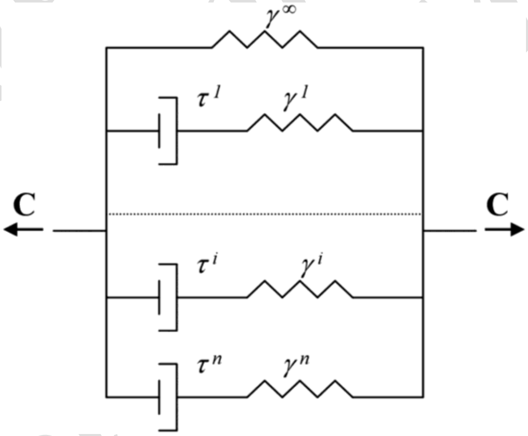

Figure 21 Zener rheological model [41].

Each viscous branch is characterized by a relaxation time τ^{i} and a relative elastic stiffness γ^{i}. The relative stiffness represents the instantaneous stiffness offered by the viscous branch. All the relative stiffness must satisfied the following equation:

$$\gamma^{\infty} + \sum_{i=1}^{n} \gamma^{i} = 1 \tag{2.25}$$

being γ_j^{∞} the relative stiffness of the equilibrium spring expressing the material stiffness at the thermodynamic balance when the viscous phenomena can be considered as completely developed [41]. The Helmholtz free energy function can now be rewritten as a sum of different contributions:

$$\psi\left(\mathbf{C},\mathbf{q}^{i}\right) = W^{\infty}\left(\mathbf{C}\right) + \sum_{i=1}^{n} \psi^{i}\left(\mathbf{C},\mathbf{q}^{i}\right) \tag{2.26}$$

W^{∞} represents the hyperelastic potential which characterizes the mechanical contribution of the equilibrium spring, while the sum of ψ^{i} defines the behaviour of the viscous branches.

The Helmholtz free-energy function can be assumed in the following specific form:

$$\psi^{i}\left(\mathbf{C},\mathbf{q}^{i}\right) = W^{i}\left(\mathbf{C}\right) - \frac{1}{2}\mathbf{q}^{i} : \mathbf{C} \tag{2.27}$$

where W^{i} is a stored energy function which is related to the instantaneous hyperelastic response in the absence of viscous processes, while the summary at the second term represents the total energy dissipated during the development of the viscous phenomena [41].

It is possible to obtain the evolution law of the internal parameters by imposing a strain compatibility condition on the whole Zener model and a stress equilibrium condition on every single viscoelastic branch reaching the following equation [41]:

$$\dot{\mathbf{q}}^{i} + \frac{1}{\tau^{i}}\mathbf{q}^{i} = 2\frac{\gamma^{i}}{\tau^{i}\gamma^{\infty}}\frac{\partial W^{\infty}}{\partial \mathbf{C}} \tag{2.28}$$

The above system of first-order ordinary differential equations, with the introduction of the condition of null initial relaxed stresses ($\lim_{t \to 0} \mathbf{q}_i = \mathbf{0}$), can be solved in the following convolution integral [41]:

$$\mathbf{q}^i(t) = \frac{\gamma^i}{\gamma^\infty \tau^i} \int_0^t \exp\left(-\frac{t-s}{\tau^i} \right) \mathbf{S}^\infty(s)\, ds \tag{2.29}$$

It is also possible to calculate the stress-strain relationship from equation 2.27 as follow:

$$\mathbf{S}\left(\mathbf{C}, \mathbf{q}^i\right) = 2\frac{\partial W^\infty}{\partial \mathbf{C}} + \sum_{i=1}^{n} \left[2\frac{\partial W^i}{\partial \mathbf{C}} - \mathbf{q}^i \right] = \mathbf{S}^\infty(\mathbf{C}) + \sum_{i=1}^{n} \mathbf{S}^i\left(\mathbf{C}, \mathbf{q}^i\right) \tag{2.30}$$

2.3 Constitutive parameters identification

The constitutive parameters evaluation consists in the identification of the set of parameters which supply the best fit of the experimental data. This procedure is usually performed by means of an inverse analysis of the constitutive model and follows a combined experimental and computational approach. The inverse analysis assumes that stress history is given and it attempts to estimate parameter values which would provide the best fit to the given stress history [42]. Geometrically simple specimens and appropriate boundary conditions are required to generate the most homogeneous stress-strain fields possible during mechanical tests. These conditions allows the adoption of analytical formulation for the description of the experimental tests. Constitutive parameters are then identified by means of the optimization of a cost function which expresses the discrepancy between experimental data and analytical model results and can be assumed as follow:

$$\Phi(\mathbf{p}) = \left\{ \frac{1}{\mathrm{N}} \sum_{\mathrm{i}=1}^{\mathrm{N}} \left[\mathrm{S}^{\exp}\left(\mathrm{t}_\mathrm{i}, \lambda_\mathrm{i}\right) - \mathrm{S}\left(\mathbf{p}, \mathrm{t}_\mathrm{i}, \lambda_\mathrm{i}\right) \right]^2 \right\}^{1/2} \tag{2.31}$$

where S are the values of the stress deduced from the constitutive model and S^{exp} the corresponding experimental values. The scalars t_i and λ_i are the N time instants of evaluation of the stress and the related values of the stretch, respectively, while **p** is a vector containing the set of the constitutive parameters.

The optimum set of constitutive parameters is defined by means of the optimization procedure of the Simulated Annealing (SA). This technique lets possible to overcome problems arising from the presence of finding local minima of the error function when it shows multimodal behavior. The SA can be seen as a process which, given a specific neighborhood structure, attempts to move from the current solution to another one of its neighbors [43]. SA starts from an initial solution and generates a new solution S' in the neighborhood of the current solution S. Subsequently it is computed the change in the objective function value, Δ=C(S') - C(S). In minimization problems, if $\Delta < 0$, transition to the new solution is accepted and the process is called downhill move. If $\Delta \geq 0$ the transition to the new solution is accepted with a probability usually computed by the function $e^{\frac{-\Delta}{T}}$ being T the temperature which is a control parameter [43]. In this way SA can avoid to stop at a local minimum in its search for the global minimum thanks to the possibility of uphill moves (transitions that increase objective function values). SA repeats this process L times at each temperature, where L is the epoch length that is a predefined control parameter. The parameter T is incrementally decreased by a cooling function as SA progresses, until a defined stopping condition is satisfied [43]. The typical procedure of SA can be summarize as follow:

1. Chose an initial solution S
2. Select a positive value for the initial temperature T and set the epoch count k = 1
3. Repeat the following L times
    - Generate a neighborhood solution S' of S
    - Compute Δ = C(S') - C(S)
    - If Δ < 0 let S be S' (downhill move)

  - If $\Delta \geq 0$ let S be S' with probability $e^{\frac{-\Delta}{T}}$ (uphill move)

4. If the stopping condition is satisfied, stop. Otherwise, let $T_i + 1 = F(T_i)$, i = i+ 1, and go to step 3. T_i and F represents the temperature at the ith epoch and the cooling function, respectively

When implementing the SA procedure it is necessary to set up an annealing schedule or cooling schedule. Such a schedule is characterized by the initial temperature (T), the cooling function (F), the epoch length (L), and a stopping condition [43]. Further, several annealing parameters are needed to specify a cooling schedule. As matter of example, often a SA algorithm uses as stopping condition the achievement of a predetermined maximum count M, so a specific value of the parameter M is needed.

The choice of suitable annealing parameters is important to achieve a satisfactory solution containing the computational costs. For this reason some criteria are indicated for the selection of these parameters. The initial temperature (T_i) should be chosen equal to an additional parameter P_i, called the initial acceptance probability that represents the fraction of accepted uphill transitions in a trial run of the annealing process. In this scheme, a certain number of transitions are made and the average increase in the objective function values δ is calculated with uphill transitions only. Then the current temperature T is calculated from the equation $T_i = \frac{\delta}{\ln(P_i)}$ [43]. Further, the value of the epoch length L can be set to be proportional to the size of the problem instance or to the number of neighborhood solutions of a given solution, or, if the total number of trials is fixed, L can be set to be proportional to the total number of trials. Finally, as stopping condition, the SA can be terminated when the epoch count L reaches a predefined maximum count M, or when the total number of trials made so far reaches a predefined limit K [43].

The validation of the constitutive parameters obtained from the above-mentioned optimization procedure is performed by means of comparison with additional experimental data. In the specific, these parameters are included in numerical analyses simulating the experimental mechanical tests and the numerical outputs are compared with experimental data to assess parameters reliability.

2.4 Experimental analysis

Experimental loading protocol are defined starting from the evidences drawn from the tissues histological and morphometrical analyses.

All the experimental tests are performed within the laboratories at disposal at the Centre for Mechanics of Biological Materials.

Several kinds of tests can be set up for the investigation of tissues mechanical properties. Uni-axial (Fig. 24b) and bi-axial tensile tests (Fig. 24c), already described in the previous chapter, are performed with the purpose to investigate tissues elastic properties.

2.4.1 Experimental setup

The experimental set-up is the Planar Biaxial TestBench® Test System (Bose ElectroForce®) which consists in four linear motors mounted on a horizontal baseplate in cross disposition (Fig. 24a). All the actuators have an excursion of ± 6.5 mm; two of them can develop a force of 400 N, while the other two a force of 200N. All the forces developed while performing mechanical tests, are recorded by means of load cells mounted near the grips that hold the specimen during the tests. According to the specimen dimensions and strength, load cells with different ranges are used. Loading protocols are set up by means of a dedicated software (WinTest® Controls) that provides waveforms generation and data acquisition. The sampling frequency can be tuned in different way according to the kind of test, to the protocol length and to the operator needs. Data are recorded in terms of the actuators displacements (mm) and developed forces (N). An additional camera, controlled by means of the same software system, allows the recording of the deformation computed on a system of five markers placed on the specimen at the beginning of the test (Fig. 24b, c).

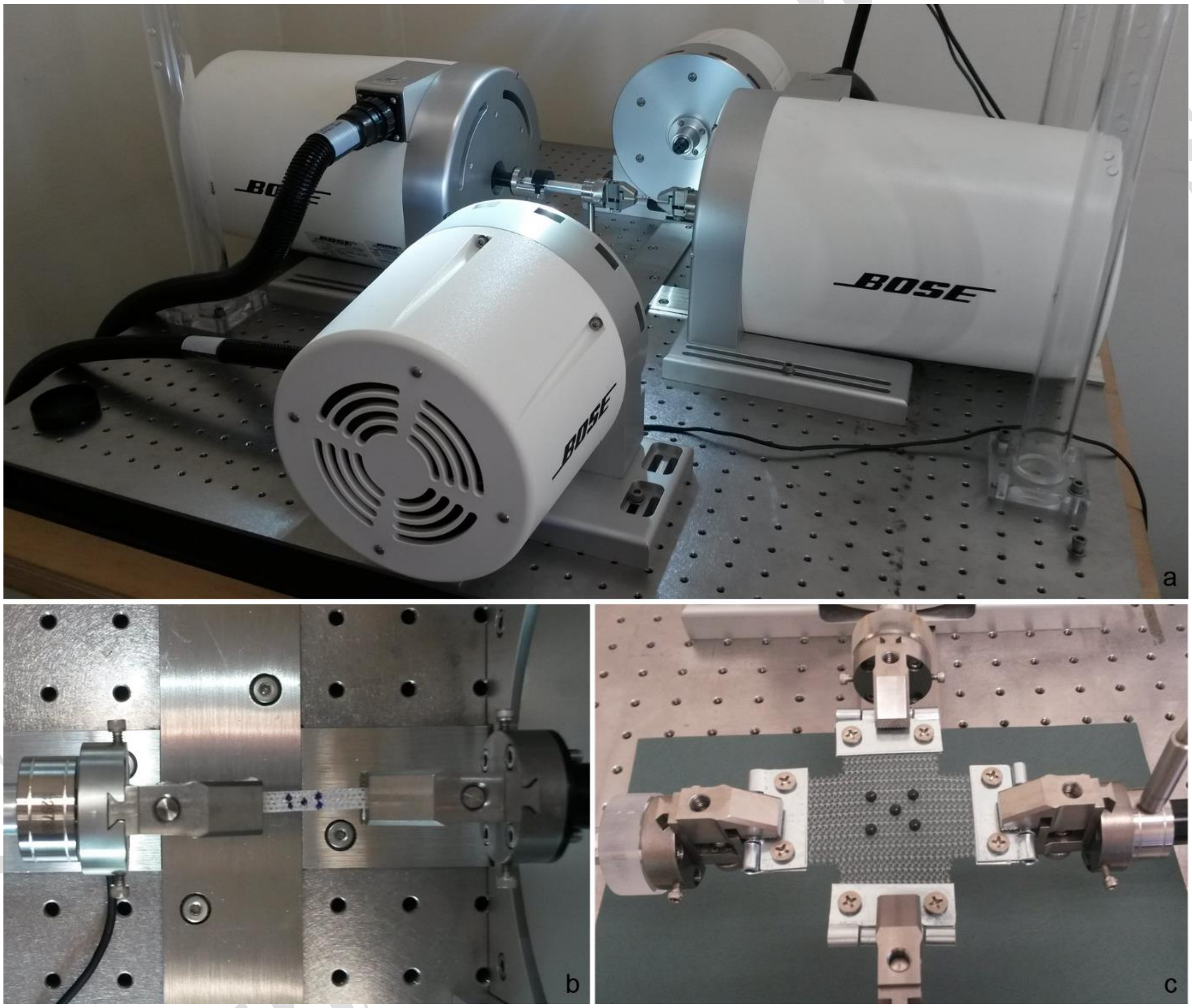

Figure 22 The Planar Biaxial TestBench® Test System (Bose ElectroForce®) (a). Uni-axial (b) and bi-axial (c) configurations; both the samples are marked for the deformations acquisition by means of the dedicated camera.

2.4.2 Material testing

2.4.2.1 Creep test

Creep tests represent a method for the quantification of the viscous properties of a material. These tests consist in an almost instantaneous application of an external force to the specimen. This force is then maintained over a chosen time interval and the deformation of the specimen is monitored over the time until the deformation value reaches an asymptotic stabilization, which means the complete development of the viscous phenomena that characterize the tissue.

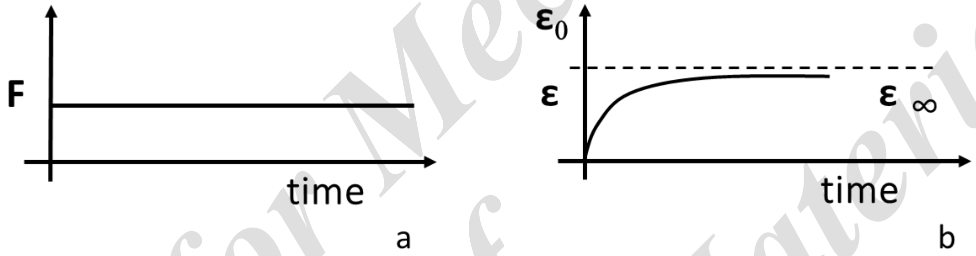

Figure 23 Qualitative schematization of the creep test: the constant force applied over time is shown in a, while the evolution of the deformations is reported in b. The term ε_{∞} is referred to the thermodynamic balance where the viscous phenomena are completely developed.

2.4.2.2 Stress relaxation test

Uni-axial stress relaxation tests are usually performed by applying to the specimen an almost instantaneous deformation that is kept over a chosen time interval that is usually, in the case of soft connective tissues, of the magnitude order of hundreds of seconds. During this time the evolution of the recorded forces is monitored until they reach an asymptotic stabilization. Stress is computed, as described in the previous chapter, by dividing the recorded load by the specimen cross-sectional area. The evolution of the stress over the time is usually expressed in normalized terms by dividing the current stress value by the initial stress peak.

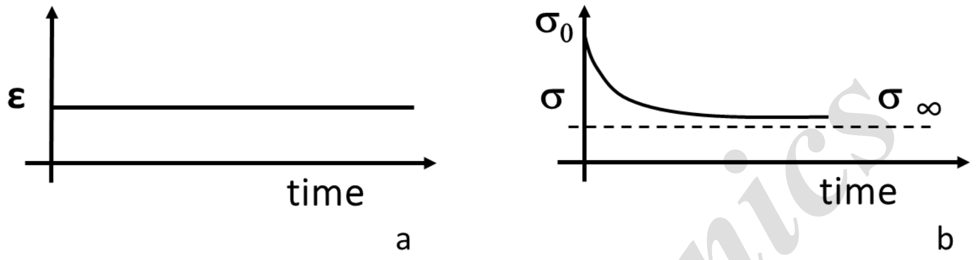

Figure 24 Qualitative schematization of the stress relaxation test: the constant deformation applied over time is shown in a, while the stress evolution is reported in b. The term σ_∞ is referred to the thermodynamic balance where the viscous phenomena are completely developed.

CHAPTER 3 BIOMECHANICAL ANALYSIS OF THE CRURAL FASCIA

3.1 Introduction

The purpose of this research consists in the evaluation of *in situ* biomechanical functionality and properties of the fascial tissue with the aim to assess its suitability when used as biomesh. For this reason the crural fascia, located in human lower limb, has been considered and analyzed. It creates three compartments enwrapping and separating different groups of muscles [27,29]. According to their location, it is possible to define an anterior, a lateral and a posterior compartment. The anterior compartment includes four muscles: tibialis anterior, extensor digitorum longus, extensor hallucis longus and peroneus tertius. The lateral compartment envelopes peroneus longus and brevis muscles. The posterior compartment contains superficially the grastrocnemius and the soleus muscles, while internally the popliteus, the flexor digitorum longus, the flexor hallucis longus, and the tibialis posterior (Fig. 25). Because of its conformation, composition and continuity the crural fascia plays a fundamental role in different aspects of leg biomechanics, being involved in muscles contraction coordination and loads transposition [44].

The choice of this particular district is due to due to the fact that the anterior compartment represents one of the most investigated region for clinical purposes, being affected from several different painful pathologies as the compartment syndrome. Therefore, it represents the compartment for which there are more data at disposal [44].

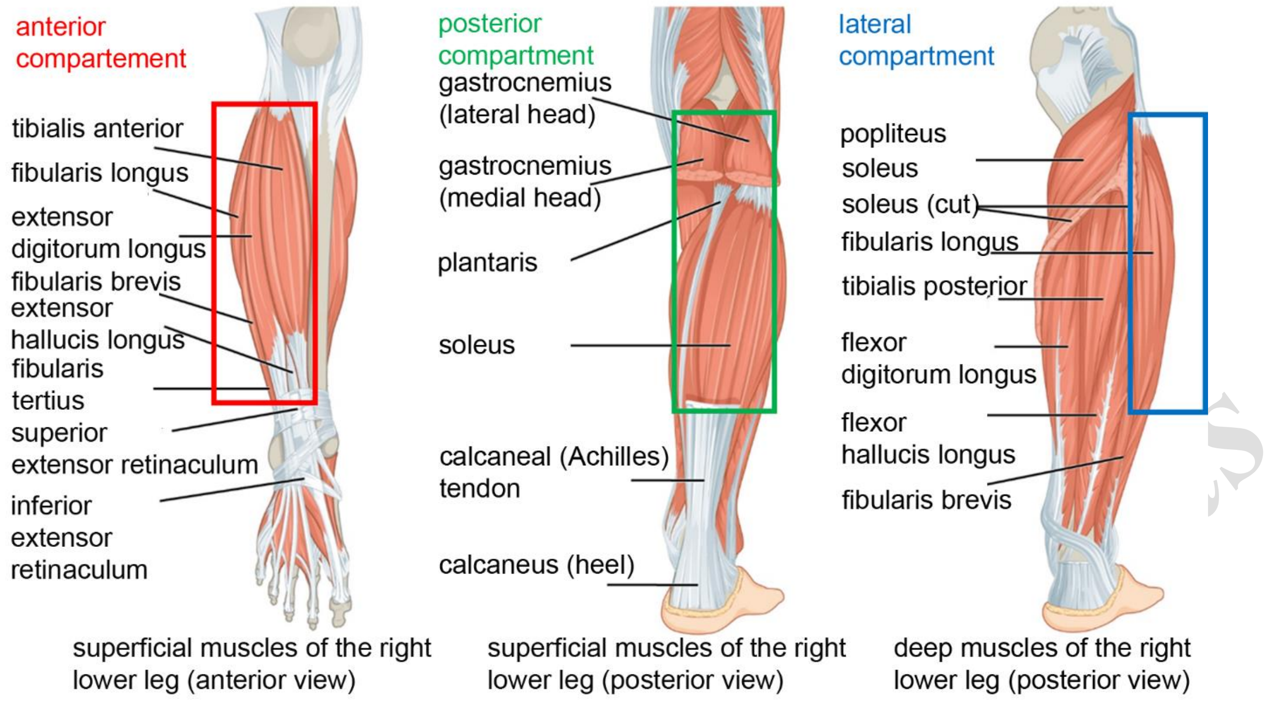

Figure 25 Muscles of the lower limb. Starting from the left, the anterior, the posterior and the lateral compartments are respectively highlighted.

The evaluation of crural fascia biomechanics is here firstly performed by the developing of a two-dimensional finite element model of a lower limb section. This latter considers the variation of the intracompartmental pressure with the change of the anterior compartment volume in combination with other parameters, such as the fascia stiffness and the level of its stretch along the proximal-distal direction. Then, with the aim to consider the effective structure of the anterior compartment, the model is upgraded to the three-dimensional case allowing a more feasible evaluation of the muscle-fascia interaction phenomena.

3.2 Crural fascia histology and morphometry

The crural fascia is composed of two dense connective tissue layers separated by an interposed thin layer of loose connective tissue. Previous experimental investigations highlighted that dense layers can have a mean thickness of 277.8 µm (SD = 86.1 µm) and the global fascia thickness is about 783.8 µm (SD = 34.5 µm) [27]. Each layer of dense tissue is reinforced by a family of collagen fibers that are oriented along a specific direction, forming an angle of about 74° with the fibers of the adjacent layer. Further, these fibers show a symmetrical disposition with respect to the proximal-distal direction having an orientation of $\alpha = \pm 37°$ (Fig. 26). This particular structural conformation appoints strong anisotropic characteristics to the material [45].

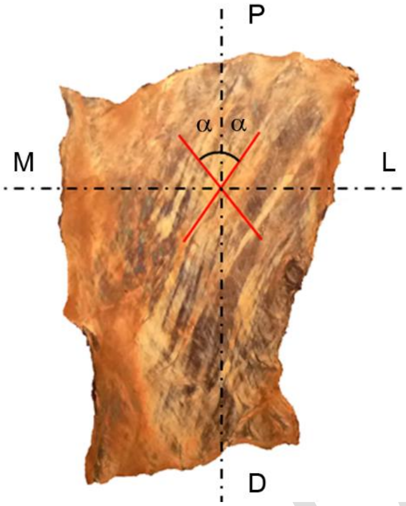

Figure 26 Fiber disposition as they appear at the examination with polarized light forming an angle $\alpha = \pm 37°$ with respect to the proximal-distal direction.

3.3 Experimental tests

3.3.1 Specimens preparation

Experimental tests are performed on different regions of crural fascia taken from the same frozen adult donor (male, age 67, weight 74.8 Kg, height 165.1 cm). Portions of crural fascia are dissected from the anterior compartment of the right and the left leg. The samples are frozen and kept at a temperature of -20° C until 20 minutes before the experimental test when they are immerged in a saline solution (PBS, phosphate buffered solution) at a temperature of about 20° C. PBS solution has the double effect of preserve samples hydration and speed up the unfrozen process [46]. Then, samples of crural fascia are cut into smaller specimens along the proximal-distal (longitudinal) and medial-lateral (transversal) directions obtaining a total of 17 specimens. Each specimens is identified by means of an alphanumeric code according to the cut direction (L = longitudinal, T = transversal) and its position is kept on a map of the original piece of tissue as shown in Fig. 27a. The specimens have rectangular shape, length about 25-30 mm and width about 3 mm. The effective dimensions are evaluated through image analysis of pictures taken with a digital camera (Fig. 27 b, c).

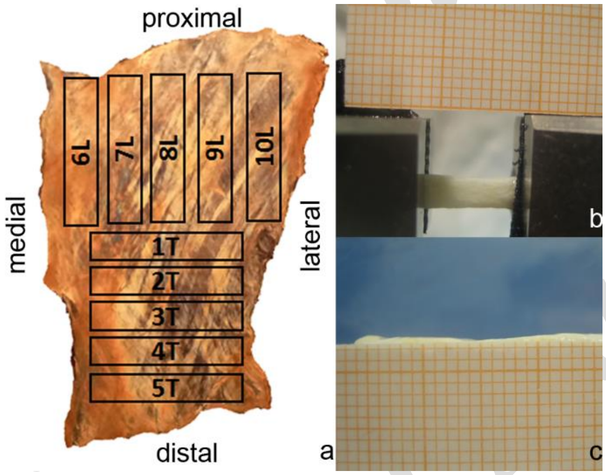

Figure 27 Map of the specimens cut along the proximal-distal direction (longitudinal, L) and along the Medial-Lateral direction (transversal, T) is reported on the left (a). Typical images used for the measure of specimens effective width (b) and thickness (c).

Then, the specimens are fixed to the grips of the experimental apparatus by means of patches of Velcro in order to avoid any slipping. The specimens are marked on their thickness in the proximity of the grip with the aim to evaluate possible slidings with respect to the grips during each test. The instrument is configured in order to impose a uni-axial loading. The free length between the grips is kept at a constant value of 10 mm (‘gauge length’), ensuring an aspect ratio (length/width) of about 3 to 1. All the tests are developed with displacement control with precision of 0.002 mm [46].

3.3.2 Mechanical tests

For the independent evaluation of the elastic instantaneous response and the time-dependent response, due to viscous phenomena, two different experimental protocols are set up and performed. Both protocols start with 10 cycles of sinusoidal preconditioning in the nominal strain range of 0-5% at the frequency of 1 Hz followed by a rest period of 60 seconds. Preconditioning represents a common practice in experimental tests on biological tissues; it has the purpose to give the same starting condition for the load history to all the specimens tested and, therefore, to obtain a stable mechanical response in the preliminary phase [46].

3.3.2.1 Protocol for the elastic properties evaluation

Three sets of five loading-unloading cycles are applied at the increasing nominal strain of 7%, 9% and 11% respectively. Each cycle is performed at strain rate of 120%/s and is separated from the following one by a rest period of 60 seconds. The number of five cycles per set is chosen on the basis of experimental evidences that show a stabilization of the tissue mechanical response after such a number of loading-unloading cycles [46].

3.3.2.2 Protocol for the viscous properties evaluation

Three consecutive stress relaxation tests at a nominal strain of 7%, 9% and 11% respectively are performed on the specimens. Each test spans a time interval of 240 seconds during which it is possible to evaluate the stress relaxation processes. At its end, the specimen is unloaded in 30 seconds. Each test is separated from the next one by a rest period of 60 seconds. The nominal strain level is applied almost instantaneously at the strain rate of 120%/s; this high strain rate is chosen with the aim to avoid any time dependent phenomenon during the initial loading ramp [46].

Both this protocols end with a ramp-to-failure consisting in an elongation at the strain rate of 120%/s in order to evaluate the ultimate stress and the failure strain.

The load-displacement data recorded are processed to calculate stress-strain values. The nominal strain is computed as the current lengthening of the sample divided by the initial grip-to-grip length. The Cauchy stress is computed as the force divided by the current value of the specimen deformed cross-sectional area. This latter is calculated dividing the value of the initial undeformed cross-sectional area by the strain value, exploiting the volume conservation constraint [46].

3.4 Fascia constitutive modeling

The considered mechanical conditions are characterized by a physiological range of strains. Further, the intracompartmental pressure acts as a steady state condition. For these reasons, it is possible to describe the mechanical response of the crural fascia by means of a hyperelastic constitutive model. Because of the presence of two families of specifically oriented collagen fibers a fiber-reinforced constitutive model is assumed. According to histological analyses, collagen fibers are considered to be mechanically equivalent highlighting a weak interaction between fibers disposed on adjacent layers. Starting from these considerations it is possible to assume a strain energy function depending on a limited number of invariants:

$$\mathrm{W} = \mathrm{W}\left(\mathrm{I}_1, \mathrm{I}_3, \mathrm{I}_4, \mathrm{I}_6\right) + \mathrm{U}\left(\mathrm{J}\right) \tag{3.1}$$

The invariants definition is recalled from the previous chapter with the addition of another structural invariant (I_6) which depends on the initial collagen fibers disposition:

$$\mathrm{I}_3 = \mathrm{J}^2 = \det\left(\mathbf{C}\right), \quad \mathrm{I}_4 = \mathbf{C}:\left(\mathbf{m}_0 \otimes \mathbf{m}_0\right), \quad \mathrm{I}_6 = \mathbf{C}:\left(\mathbf{n}_0 \otimes \mathbf{n}_0\right) \tag{3.2}$$

The fiber disposition is defined by the unit vectors $\mathbf{m}_0$ and $\mathbf{n}_0$, respectively. Exploiting biological tissue incompressibility constrain and the additive contribution of the ground matrix and of the collagen fibers, it is possible to consider the following specific strain energy function [45]:

$$\begin{aligned} W = {} & \frac{k_v}{2}\left(J^2 - 2\ln J\right) + \frac{\mu}{2}\left(\tilde{I}_1 - 3\right) + \frac{k_m}{2\alpha_m}\left\{\exp\left[\alpha_m\left(\tilde{I}_1 - 3\right)\right] - \alpha_m\left(\tilde{I}_1 - 3\right) - 1\right\} + \\ & + \frac{k_f}{2\alpha_f}\left\{\exp\left[\alpha_f\left(\tilde{I}_4 - 1\right)\right] - \alpha_f\left(\tilde{I}_4 - 1\right) - 1\right\} + \\ & + \frac{k_f}{2\alpha_f}\left\{\exp\left[\alpha_f\left(\tilde{I}_6 - 1\right)\right] - \alpha_f\left(\tilde{I}_6 - 1\right) - 1\right\} \end{aligned} \tag{3.3}$$

where k_v is the bulk modulus, μ, k_m and α_m are terms related to the mechanical response of the ground matrix, while k_f and α_f are related to collagen fibers. The terms α_m, α_f are dimensionless and account for the non linear response of the ground matrix and oriented collagen fibers, while μ, k_m and k_f are stress-like parameters. The exponential terms of equation (3.3) are enabled only in the case of a tensile strain with the aim to account for the null contribution of the fibers in compression. It is possible to obtain the stress in terms of the second Piola-Kirchhoff stress tensor:

$$\mathbf{S} = 2\frac{\partial W}{\partial \mathbf{C}} = Jp\mathbf{C}^{-1} + \tilde{\mathbf{S}}_m + \tilde{\mathbf{S}}_f \tag{3.4}$$

being $p = k_v\left(J - \frac{1}{J}\right)$ the hydrostatic pressure, while the two tensors of the right hand side are given by [45]:

$$\begin{aligned} \tilde{\mathbf{S}}_m & = \left\{\mu + k_m \exp\left[\alpha_m\left(\tilde{I}_1 - 3\right) - 1\right]\right\}\left[\mathbf{I} - \frac{I_1}{3}\mathbf{C}^{-1}\right] \\ \tilde{\mathbf{S}}_f & = k_f\left\{\exp\left[\alpha_f\left(\tilde{I}_4 - 1\right)\right] - 1\right\} J^{-2/3}\left[\mathbf{n}_0 \otimes \mathbf{n}_0 - \frac{I_4}{3}\mathbf{C}^{-1}\right] + \\ & \quad + k_f\left\{\exp\left[\alpha_f\left(\tilde{I}_6 - 1\right)\right] - 1\right\} J^{-2/3}\left[\mathbf{m}_0 \otimes \mathbf{m}_0 - \frac{I_6}{3}\mathbf{C}^{-1}\right] \end{aligned} \tag{3.5}$$

3.5 Parameters identification

The constitutive model is fitted to the experimental mechanical response of the tissue accounting for uni-axial independent tensile tests along the proximal-distal (P-D) and the medial-lateral (M-L) directions that are the symmetric axes with respect to the initial fibers disposition. A uni-axial stress condition is considered to be a suitable approximation of the mechanical state because of the adopted specimens aspect ratio. The kinematics constraint of incompressibility is exploited to obtain non null stress components as a function of the stretches in the membrane plane. The stress component along the loading direction is deduced from the nominal stress P as S=P/λ, where λ represents the stretch along the elongation direction [45]. The unit vectors $\mathbf{m}_0 = (\cos\alpha, \sin\alpha, 0)$ and $\mathbf{n}_0 = (\cos\alpha, -\sin\alpha, 0)$ define the collagen fibers orientation in the initial configuration, being α the fiber angle of 37° in the P-D direction. The adopted constitutive formulation depends on a set of five parameters $\boldsymbol{\eta} = (\mu, k_m, \alpha_m, k_f, \alpha_f)$. Then, the optimum set η_{opt} is obtained by means of the minimization of a scalar function that defines the error between experimental data and numerical results:

$$\Phi(\boldsymbol{\eta}) = \left\{\left[\Phi_{P-D}(\boldsymbol{\eta})\right]^2 + \left[\Phi_{M-L}(\boldsymbol{\eta})\right]^2\right\}^{1/2} \tag{3.6}$$

where the two terms $\Phi_{P-D}(\boldsymbol{\eta})$ and $\Phi_{M-L}(\boldsymbol{\eta})$ are expressed as follow:

$$\Phi_{P-D}(\boldsymbol{\eta}) = \frac{1}{N_{P-D}} \sum_{i=1}^{N_{P-D}} \left[1 - S_{1,i}^{exp}\left(\lambda_{1,i}^{exp}\right) \big/ S_1\left(\boldsymbol{\eta}, \lambda_{1,i}^{exp}, \lambda_{2,i}\right)\right]^2 \tag{3.7}$$

$$\Phi_{M-L}(\boldsymbol{\eta}) = \frac{1}{N_{M-L}} \sum_{i=1}^{N_{M-L}} \left[1 - S_{2,i}^{exp}\left(\lambda_{2,i}^{exp}\right) \big/ S_2\left(\boldsymbol{\eta}, \lambda_{1,i}, \lambda_{2,i}^{exp}\right)\right]^2 \tag{3.8}$$

$N_{P\text{-}D}$ and $N_{M\text{-}L}$ are the number of experimental values $\left(S_{j,i}^{exp}, \lambda_{j,i}^{exp}\right)$ for the two independent tensile tests in the P-D and M-L direction, respectively. The membrane stretch perpendicular to the loading direction is obtained, for each couple of experimental values, by imposing a null value of the corresponding stress component [45].

3.6 Two dimensional FEM model of a lower limb section

The transversal segment of the lower limb at the medial third is modeled on the basis of anatomical data, detailing the different regions, i.e. bones, muscle compartments, vein, fascial systems, fat and skin (Fig. 28). A relative simple connection of the crural fascia with surrounding structures, in particular with enwrapped muscles, characterizes this section. Because of the mechanical conditions analyzed and the geometrical characteristics of the anatomical district, a two-dimensional model that assumes an imposed strain in the proximal-distal direction is considered as a reasonable approximation. The Finite Element model is created with Abaqus/CAE (Dassault Systémes), using two-dimensional plane strain elements, with a hybrid formulation for soft tissues that show an almost incompressible behavior. With the aim to describe the possible sliding of the deep fascia with surrounding tissues, namely muscles and fat tissues, frictionless contact conditions are here considered [45].

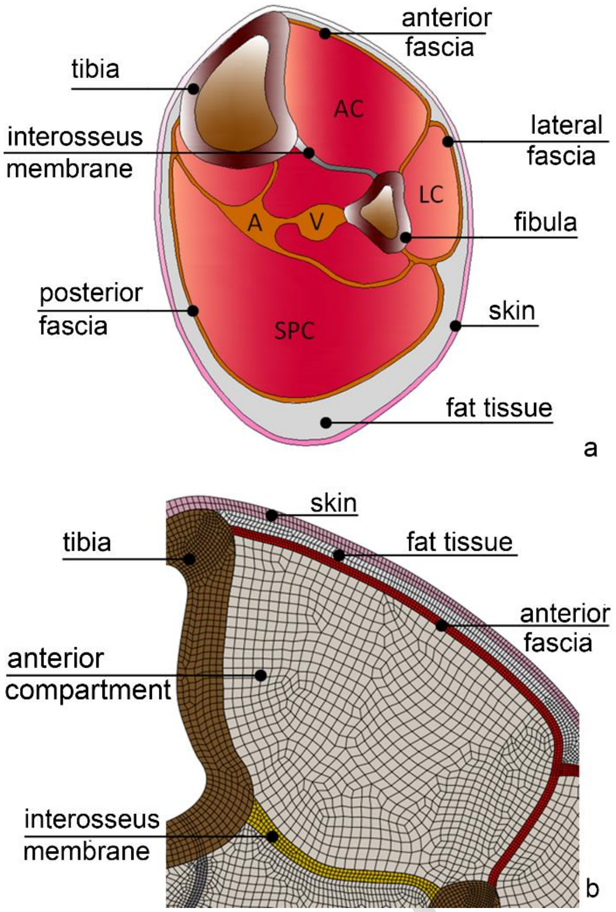

Figure 28 Representation of the transversal section (a) of the lower limb: AC is the anterior compartment, LC is the lateral compartment, while SPC is the superficial posterior compartment. V represents the vein and A the artery. Details of the corresponding two-dimensional finite element model of the anterior region are reported in (b) [45].

3.6.1 Constitutive models for lower limbs tissues

The crural fascia is modeled adopting the hyperelastic and fiber-reinforced constitutive formulation previously described, while the other tissues are defined according to data from the literature. The tibia and fibula cortical bone is modeled as an orthotropic and linear elastic material [47]. The interosseous membrane, which connects tibia and fibula, is considered as linear elastic characterized by a Young’s modulus of 600 MPa and a Poisson’s ratio of 0.3 [48].

Skin [49] and fat tissues [50] are modeled as linear elastic incompressible materials with Young's modulus of 0.02 MPa and 0.00321 MPa, respectively. The properties of blood vessels and their surrounding soft envelopment are homogenized, as a reasonable approximation, assuming the elastic mechanical properties of the fat. Muscles are modeled as poro-elastic material characterized by a shear modulus of 0.0083 MPa [51].

3.6.1.1 Notes about the muscle poro-elastic formulation

Muscles are described as a fully saturated medium according to the principle of effective stress [52]:

$$\begin{aligned} \boldsymbol{\sigma}_s &= \boldsymbol{\sigma}_{s,eff} - \alpha p \mathbf{I} \\ \boldsymbol{\sigma}_f &= -p\mathbf{I} \end{aligned} \tag{3.9}$$

being σ_s the total stress, $\sigma_{s,eff}$ the effective stress and σ_f the stress on the fluid phase. **I** represents the second rank order tensor, the scalar p is the hydrostatic pressure and α is the solid volume to fluid volume ratio. The mechanical response of the solid skeleton is assumed to behave following an isotropic elastic law defined by the neo-Hookean form of the strain energy function defined below [52]:

$$W = \frac{\mu}{2}\left(\tilde{I}_1 - 3\right) + \frac{1}{D}\left(\sqrt{I_3} - 1\right)^2 \tag{3.10}$$

μ is the initial shear modulus and D is the inverse of the initial bulk modulus. Any effect of the anisotropy induced by a specific spatial disposition can be considered negligible because the analyses do not refer to contraction states of the muscle fibers. Therefore, the assumption of isotropy for the solid skeleton is reasonable.

The muscles volume increase is achieved by imposing a homogenous pore pressure in each muscle compartment. According to Darcy's law that describes the relative velocity of the fluid phase [52]:

$$k\nabla p = \mathbf{v}_{s,eff} - \mathbf{v} \tag{3.11}$$

as proportional to the permeability k , there is no flux of fluid phases, so it is not necessary a permeability experimental datum.

3.6.2 Loading and boundary conditions

The internal edges of fibula and tibia are considered fixed. The local change of anterior compartment is obtained by imposing a change of the pore pressure, considering impervious contact surfaces between fascial tissues and underlying muscles. A basal condition is achieved by applying an intracompartmental pressure of 15 mmHg, which is in the range of physiological values [53]. The considered loading condition starts from the basal state and increases the pore pressure within the anterior compartment to determine a maximum intracompartmental pressure of 120 mmHg. The intracompartmental pressure in the lateral and posterior compartments is kept at 15 mmHg. The range of pressure considered includes the maximum intracompartmental pressure (100 mmHg) reported in the case of compartment syndrome.

3.6.3 Investigation of stiffening effects on fascial tissues

According to experimental data the stress-strain response of the fascial tissue is less variable along the circumferential direction than along the proximal-distal direction [46]. Therefore, specific analyses are developed to evaluate the effects of a stiffness change along the proximal-distal direction of the tissue on the global deformation of fascial structure and to quantify the intracompartmental pressure-volume relation.

Experimental stress-strain data for the fascial tissue of the anterior compartment are shown in Figure 29. It reports the tensile response along the proximal-distal direction, considering both the average (L mean) and the maximum (L max) stiffness response, and the medial-lateral direction, considering the average stress response (T mean). The corresponding stress-strain numerical curves, obtained from the constitutive model assumed for the fascia, are also reported. Two set of constitutive parameters are considered: the first set is referred to the average experimental stiffness of the fascial tissue along the proximal-distal direction (L mean), while the second accounts for the maximum experimental stiffness found during mechanical tests along the same direction (L max). In both cases the same average stiffness is assumed along the medial-lateral direction because of its limited variation up to 10% of nominal strain that is a strain value, which includes the maximum values for the investigated conditions [52]. The constitutive parameters obtained by the best fit of both mean and maxima data are reported in Table 3.

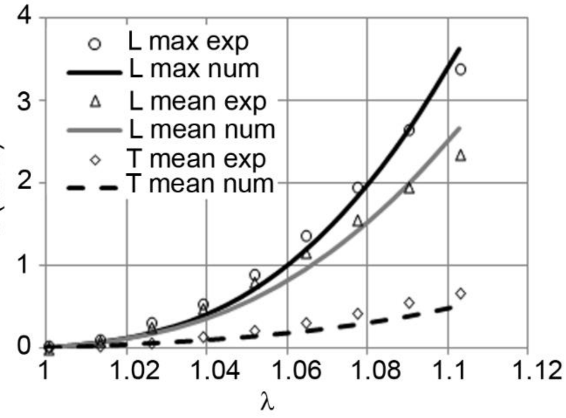

Figure 29 Stress-stretch behavior for the anterior crural fascia in terms of Cauchy stress versus stretch. The curves obtained by the numerical model are reported as solid lines, while open symbols represent experimental data for proximal-distal (L) and circumferential (T) direction [52].

	k_m (MPa)	α_m	k_f (MPa)	α_f
mean data	22.48	1.17	21.11	1.03
max data	25.69	1.15	28.47	1.5

Table 3 Constitutive parameters obtained by the best fit of the experimental tensile tests along proximal-distal and medial-lateral directions both considering the mean and the maxima data.

3.6.4 Investigation of the effects of fascial strain

Crural fascia mechanical response is considered for two values of strain imposed along the proximal-distal direction. This pre-strain condition is achieved by imposing a nominal strain of 1% and 2% whose effects are compared with the reference case of plane strain condition (null strain in the proximal-distal direction). The aim of the analyses consists in the evaluation of the fascia stiffening due to this imposed strain and the consequent effects in the interaction phenomena with the underlying muscular compartments. The constitutive model for the fascia is implemented in the finite element software by a user-subroutine modified to account for non-null values of strain imposed along the proximal-distal direction [52].

3.6.5 Numerical analysis and results

3.6.5.1 Effects of crural fascia stiffness

Figure 30 reports the effects of a stiffness change of the crural fascia along the proximal-distal direction evaluated at the intermediate value of intracompartmental pressure of 70 mmHg.

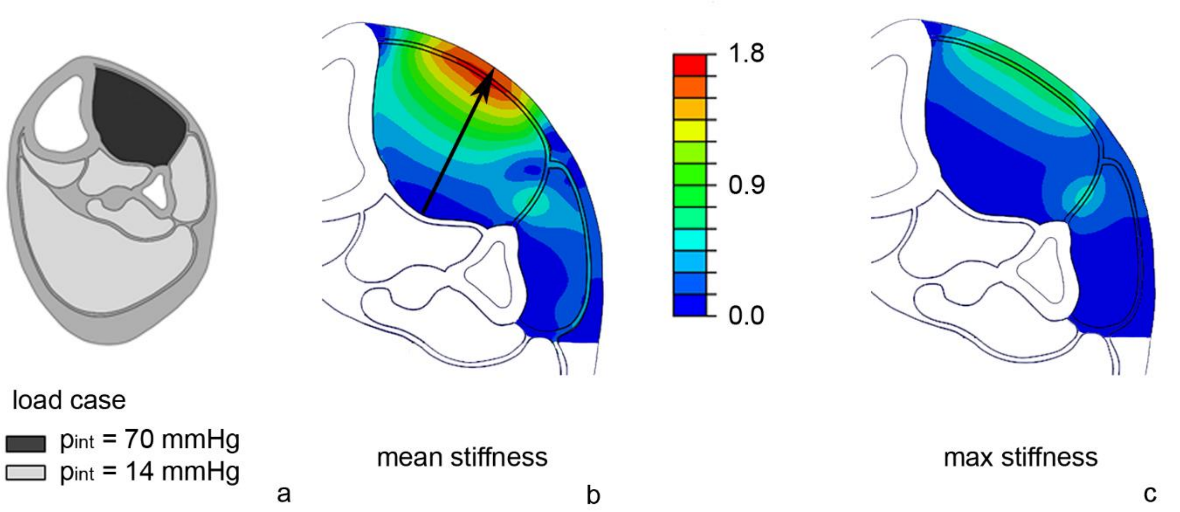

Figure 30 Magnitude displacements field (mm) induced by the intracompartmental pressures indicated in (a). The displacements are reported for the case of crural fascia with mean stiffness (b) and maximum stiffness (c) along the proximal-distal direction [52]. The arrow represents the direction for the experimental measurement of the volume variation, according to [54].

Figure 31a shows the relation between intracompartmental pressure and the relative change of the compartment area in the considered range of pressure that spans from 15 mmHg to 120 mmHg. The change of compartment area is normalized to an assumed basal value of 15 mmHg [52].

3.6.5.2 Effects of crural fascia proximal-distal strain

Figure 31b reports the anterior intracompartmental pressure versus the compartment area in the range of pressure of 15-120 mmHg for different values of strain imposed along the proximal-distal direction: 0 corresponding to a reference basal plane strain condition, 1% and 2% of nominal strain. In this case the change of compartment area corresponds to the change of compartment volume caused by the fixed value of strain imposed in the proximal-distal direction. The starting basal value of the anterior compartment area is 816.4 mm^2 at 15 mmHg and it is reduced to 801.4 mm^2 and 788.5 mm^2, respectively, for the pre-strain condition of 1%

and 2%. The changes correspond to a percentage reduction of -1.85% and -3.4% of compartment area at the basal pressure, highlighted by the right shifting of the pressure-area curves [52].

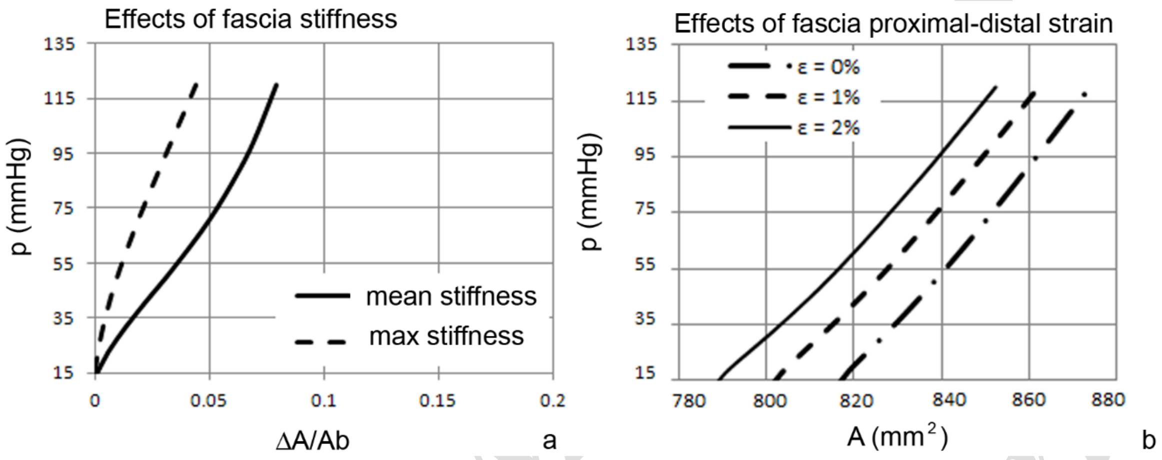

Figure 31 Intracompartmental pressure in the anterior compartment versus the change of compartment area normalized to its basal value. Black solid line represents the numerical result for the average longitudinal stiffness of the fascia, while the black dashed line refers to maximum longitudinal stiffness of the fascia (a). Intracompartmental pressure versus compartment area: numerical results are shown for the plane strain condition (dashed-dotted line) and imposed proximal-distal strain of 1% (dashed line) and 2% (solid line), respectively [52].

Data from literature report the experimental measure of the anterior compartment deformation by evaluating the variation of the equivalent radius along the direction indicated in Figure 30b. These measurements are performed in a range of intra-compartment pressures which spans from physiological to pathological values [54]. A percentage variation of the anterior compartment diameter from 5.8% to 9% with respect to the basal condition, is highlighted by ultrasound measurements on different subjects. The numerical analyses conducted by applying an internal pressure similar to that of experimental conditions (50-60 mmHg) show a percentage increase of the compartment diameter ranging from 5.6% to 7.6% if compared to the basal condition [45]. This interval is in agreement with the literature [54], confirming the reliability of the developed numerical model.

The proposed numerical analyses show that both a difference of fascia stiffness and the increase of the imposed strain on the fascia in the proximal-distal direction cause an increment of the intracompartmental pressure. As the stress-strain level of the fascial tissue is unknown, it is important the quantitative estimation of the correlation between the above-mentioned conditions and the increase of intracompartmental pressure with that of the compartment area. This mechanical description neglects the fascia visco-elastic behavior, which is a marginal feature because the interaction phenomena are considered to take place over the long term, allowing the assumption of viscous processes as being completely developed [52].

The proposed model represents an upgrade of others that have emerged in the literature and describe the tissue mechanical behavior as linear elastic. The non-linear behavior assumed for the crural fascia represents its mechanical response in a more effective way. Further, the model accounts for the anisotropy of the tissue that represents an important aspect in determining the enwrapping action of the fascia. This first numerical approach lets it possible to investigate, with a certain degree of detail, the influence of different features on the biomechanical response of the crural fascia in interaction with surrounding structures. This can be of interest, as matter of example, in evaluating those conditions that could represent a possible onset of pathologies related to non-physiological values of intracompartmental pressure, such as the compartment syndrome. It should be considered the fact that several patient conditions are quantitatively unknown, and their determination would require difficult or invasive methods. For this reason it is important to have a tool capable of supplying a feasible range of mechanical states that can be associated to paraphysiological or pathological conditions [52].

3.7 Three dimensional model of the anterior compartment

An extension of the above described model to the three-dimensional case is mandatory for a more accurate description of fascia effective *in situ* biomechanical role and for the evaluation of the interactions with underlying muscular structures. The proposed numerical approach takes into account the morphology of the whole anterior compartment region, leading to a feasible description of fascia biomechanical behavior. A detailed description of the mechanical response of the different tissues leads to an improvement with respect to previous analytical [55] or numerical models [52]. In particular, this model accounts for the combined presence of constitutive formulations capable of representing the anisotropic and nonlinear response of both crural fascia and muscle tissues [44].

Specific numerical analyses are developed to investigate muscle-fascia interaction phenomena during isotonic muscles contraction and to evaluate pressure induced within muscles and consequent stress and strain fields arising on the crural fascia. Numerical outcomes are validated by means of comparison with experimental data from laser scanning of a leg both during rest condition and during maximal dorsi-flexion contraction. Pressures within the compartment are also compared to experimental data recorded during concentric contraction [56] allowing the model outcomes validation.

3.7.1 Definition of the solid and the numerical model

The solid model of the anterior compartment accounts for the crural fascia and the enveloped muscular structures. It is developed starting from diagnostic images (MRI) by means of a specific segmentation software that allows a high accurate reconstruction of the three dimensional structures. Further, histological and morphometric data from literature are considered for the definition of the model geometry [46]. According to the histological analyses the crural fascia is modeled as a multilayered structure composed of three different strata: two external layers of dense connective tissue (mean thickness 0.3 mm) separated by a layer of loose connective tissue (mean thickness 0.2 mm). In the upper region of the leg, at the iliotibial tract, the crural fascia takes the shape of a cone which represents the connection with the fascia lata of the thigh. In the distal part, at the height of the superior retinaculum, the external layers thickness is increased up to 0.55 mm for a width of 30 mm, with the aim to reproduce the experimentally observed physiological thickening of the fascia. The muscular volume is outwardly surrounded by fascial components and internally it is confined by rigid surfaces representing the bounding of bony structures and interosseous membrane [44].

The finite element discretization of the solid model, performed by means of CAE ABAQUS® software (SIMULIA, Daussault Systems), leads to the definition of the numerical model. Fascia external layers are defined trough four node membrane elements, the interposed stratum through brick elements while, the muscular structure, is discretized by means of tetrahedral elements. The adopted mean side length for all the elements is about 3 mm (Fig. 32). Between the inferior dense layer of the fascia and the enwrapped muscles a contact surfaces is defined. It is characterized by null friction with the aim to account for the physiological condition of relative sliding between muscles and fascia [44].

The four muscles enwrapped by the crural fascia in the anterior compartment are modeled as a single volume and the disposition of the muscle fibers is simplified by assuming the characteristic of a fusiform muscle. With the purpose to define the spatial disposition of the muscle fibers a specific subroutine is implemented. The fiber disposition in a specified point is obtained by considering four spline functions enclosing the point and making use of interpolation by means of bilinear shape functions [44].

Aiming at the evaluation of the physiological shape variation due to the anterior muscular concentric contraction, the morphometry of the leg in a rest condition and during a maximal dorsi-flexion of the foot is considered. These two different configurations are obtained starting from the acquisition of points clouds by means of the laser scanner FARO Edge ScanArm® (FARO Technologies, Inc., Lake Mary, Florida) [44].

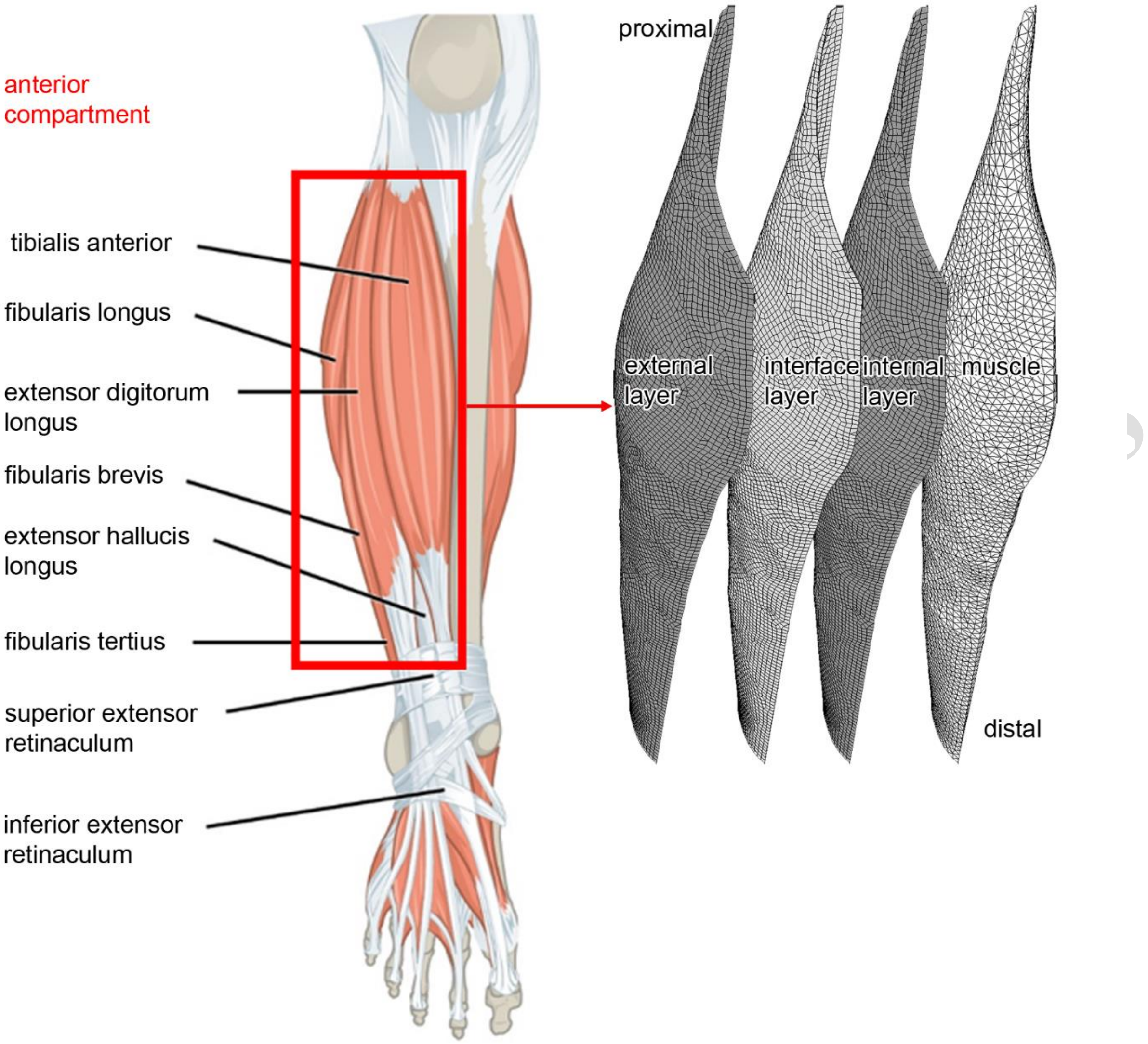

Figure 32 On the left the anatomy of the anterior compartment is highlighted. On the right the different regions of the numerical model: muscle structure and layers of crural fascia.

3.7.2 Constitutive models for lower limb tissues in 3D

3.7.2.1 External fascia layers

For the description of the biomechanical behavior of the dense tissue layers, a fiber-reinforced and almost-incompressible hyperelastic constitutive model is assumed. Exploiting, as usual, the decomposition in volume-changing and volume-preserving components and considering the summation of different contributions due to the ground matrix and fibers mechanical response, it is possible to define the strain energy function. This latter accounts for a family of collagen fibers appointing local transversal isotropic properties to the single layer:

$$W_f = W_{fm} + W_{ff} = \left[\frac{\mu_f}{2} \left(\tilde{I}_1 - 3 \right) + \frac{k_{fv}}{2} \left(J^2 - 1 - 2 \ln J \right) \right] + \frac{\alpha_{f1}}{2\alpha_{f2}} \left[\exp\left(\alpha_{f2} \left\langle \tilde{I}_4 - 1 \right\rangle^2 \right) - 1 \right] \quad (3.12)$$

k_{fv} is related to the initial bulk modulus of the ground matrix, μ_f represents its initial shear stiffness. α_{f1} (stress-like) and α_{f2} (dimensionless) are constitutive parameters related to the fibers mechanical response. The estimated values of the constitutive parameters adopted are reported in Table 4.

k_{fv} (MPa)	μ_f (MPa)	α_{f1} (MPa)	α_{f2}
2000	0.6	4.88	3.61

Table 4 Constitutive parameters obtained by the best fit of the average experimental tensile tests along proximal-distal and medial-lateral directions.

The fibers of the internal and external layer, that are considered mechanically equivalent, differ for spatial orientation: the inner layer is characterized by fibers forming an average angle of 37° with the proximal-distal direction, while the external fibers are symmetrically disposed with the same angle with respect to the proximal-distal direction [44].

3.7.2.2 Internal layer

The interposed loose connective tissue is described by means of a hyperelastic neo-Hookean formulation with a strain energy function W_i defined as:

$$W_l = \frac{\mu_l}{2} \left(\tilde{I}_1 - 3 \right) + \frac{k_{lv}}{2} \left(J^2 - 1 - 2 \ln J \right) \quad (3.13)$$

This layer is primarily composed by hyaluronic acid that is usually considered as a Newtonian fluid characterized by a constant viscosity of 5300 cP in a wide range of temperatures which include 37°C [57]. This formulation describes the internal layer mechanical response as elastic. This is considered a reasonable approximation because it is observed that, during the muscle contraction, the interposed loose tissue is deformed at constant shear strain rate. The shear modulus is determined by image analysis of frames taken from of an echographic video reproducing the mutual sliding of the dense layers of human fascia lata during thigh muscles contraction [44]. The average sliding speed between selected points located in the different fascial layers is computed. Then, by this datum and considering the thickness, a mean shear strain rate of 1.375 s^{-1} of the interposed loose tissue layer is computed. As consequence, a shear modulus of 0.0017 MPa is calculated as $\mu_l = c\dot{\gamma}$ [44].

3.7.2.3 Muscular structure

A three-elements Hill’s functional model is adopted for the description of muscles mechanical response (Fig. 33).

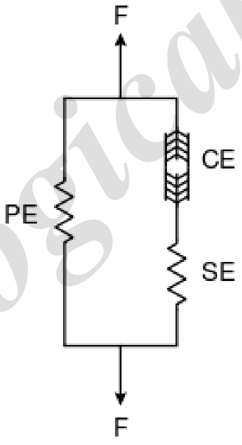

Figure 33 Representation of Hill's elastic muscle model. F is the force characteristic of a muscle, CE represents the contractile element, while SE (series element) and PE (parallel element) are two nonlinear spring elements.

Equation 3.13 provides the relationship between the stretch of the muscle fiber λ_f, the stretch of the active part λ_m and passive part λ_f of the sarcomeric elements [58]:

$$\left(1+\mathrm{k}\right)\lambda_{\mathrm{f}} = \lambda_{\mathrm{m}} + \mathrm{k}\lambda_{\mathrm{s}} \tag{3.14}$$

The parameter k is set at 0.3 according to data from literature. It is therefore possible to deduce the stretch of the fiber as

$$\lambda_{\mathrm{f}} = \sqrt{\tilde{\mathbf{C}} : \left(\mathbf{n}_0 \otimes \mathbf{n}_0\right)} \tag{3.15}$$

where the unit vector $\mathbf{n}_0$ is related to the initial fiber disposition in the undeformed configuration. The muscles stress response is defined through the sum of an isotropic $\mathbf{P}_{iso}$ and an anisotropic $\mathbf{P}_{aniso}$ contributions. It is possible to obtain the isotropic term by deriving the following strain energy function [44]:

$$\mathrm{w}_{\mathrm{iso}} = \alpha_{\mathrm{m1}} \exp\left[\alpha_{\mathrm{m2}}\left(\tilde{\mathrm{I}}_1 - 3\right)\right] + \frac{\mathrm{k}_{\mathrm{mv}}}{2}\left(\mathrm{J}^2 - 1 - 2\ln \mathrm{J}\right) \tag{3.16}$$

while the anisotropic part is expressed through the sum of an active ($\mathbf{P}_a$) and a passive ($\mathbf{P}_p$) contribution:

$$\mathbf{P}_{\mathrm{aniso}} = \left(\mathrm{P}_{\mathrm{p}} + \mathrm{P}_{\mathrm{a}}\right)\mathbf{F}\mathbf{n}_0 \otimes \mathbf{n}_0 \tag{3.17}$$

The passive term, which is related to the response of the parallel elastic element PE, is defined as

$$\mathrm{P}_{\mathrm{p}} = 4\mathrm{P}_0\left(\lambda_{\mathrm{f}} - 1\right)^2 \tag{3.18}$$

while the active term, given by the element CE, is related to the force generated by the actin and myosin cross-bridges at the sarcomere level and it is expressed as:

$$P_a = f_a(t) f_l(\lambda_m) f_v(\dot{\lambda}_m) P_0 \tag{3.19}$$

where $f_a(t)$ is the activation function, $f_l(\lambda_m)$ is the force-length function, $f_v(\dot{\lambda}_m)$ the force-velocity function, and P_0 the maximum isometric stress. The variable t represents the time variable and $\dot{\lambda}_m$ is the derivative with respect to time. The force-velocity function is not necessary for the proposed numerical analyses and it is considered with the aim to provide a constitutive model of general applicability [44]. The activation function has the following formulation:

$$f_a(t) = \begin{cases} a_0 & t \le t_0 \\ a_0 + (a_1 - a_0) \cdot h_t(t, t_0) & t_0 < t \le t_1 \\ a_0 + (a_1 - a_0) \cdot h_t(t_1, t_0) \cdot \left[1 - h_t(t, t_1)\right] & t_1 < t \end{cases} \tag{3.20}$$

being t_0 and t_1 the initial and final time instants of activation, respectively. The constants a_0 and a_1 are set at 0 and 1, according to data from literature [59]. The function h_t assumes the following formulation:

$$h_t(t, t_i) = 1 - \exp\left[-S(t - t_i)\right] \tag{3.21}$$

where $S = 50\ s^{-1}$. The force-length function is assumed as proposed by [60]:

$$f_l(\lambda_m) = \begin{cases} \dfrac{\lambda_m - \lambda_{min}}{\lambda_{opt} - \lambda_{min}} \exp\left[\dfrac{(2\lambda_{min} - \lambda_m - \lambda_{opt})(\lambda_m - \lambda_{opt})}{2(\lambda_{min} - \lambda_{opt})^2}\right] & \lambda_m > \lambda_{min} \\ 0 & \text{otherwise} \end{cases} \tag{3.22}$$

where $\lambda_{min} = 0.682$ and $\lambda_m = 1.019$. The force-velocity function takes the following sigmoid shape:

$$f_v\left(\dot{\lambda}_m\right)=\frac{\delta_1}{\delta_2+\delta_3\exp\left(-\delta_4\dot{\lambda}_m\right)} \tag{3.23}$$

setting $\delta_1 = 1.514$, $\delta_2 = 0.996$, $\delta_3 = 0.542$ and $\delta_4 = 0.558$.

The stress of the serial elastic element SE is given by [60]:

$$P_{SE}=\beta_0\left\{\exp\left[\beta_1\left(\lambda_f-1\right)\right]-1\right\} \tag{3.24}$$

assuming $\beta_0 = 0.001$ and $\beta_1 = 10.0$.

This constitutive formulation is implemented in the finite element code by means of a user defined subroutine through an implicit integration scheme. The time derivative of the stretches λ_f and λ_m are obtained in the algorithmic forms of $\dot{\lambda}_f \cong \left(\lambda_f^{n+1}-\lambda_f^{n}\right)/\Delta t$ and $\dot{\lambda}_m \cong \left(\lambda_m^{n+1}-\lambda_m^{n}\right)/\Delta t$, being Δt the time increment at the current time instant t_{n+1} [44] .

3.7.3 Numerical analysis and results

The reliability of the model, as pertain both the muscle tissue behavior and the interaction phenomena of muscles with the crural fascia, is tested through different analyses.

The constitutive formulation adopted for the muscle is tested by simulating both isotonic and isometric contractions on a muscle model characterized by a simplified geometry which ends with two aponeuroses along the x axis. Exploiting the structure symmetry along the (x,y) and the (x,z) planes it is possible to model only one quarter of the whole structure (Fig. 33). The muscle contraction is evaluated accounting for different spatial distributions of its fibers. In particular it is taken into account a fibers disposition corresponding to a fusiform muscle and a disposition corresponding to a bi-pennate muscle characterized by a pennation angle of 30°. All the fibers are subjected to the same activation function [44]. The suitability of the constitutive model to represent the active behavior of muscle fibers for the simulated conditions is shown in Figure 33. An isotonic contraction, which is characterized by a null external load applied, is here considered. In this particular loading condition the fusiform muscle shows a greater shortening due to the greater length of muscle fibers if compared to the pennate muscle. Further, it is possible to note the different deformation characterizing the two muscles, with a greater bulging of the fusiform muscle with respect to the pennate one [44].

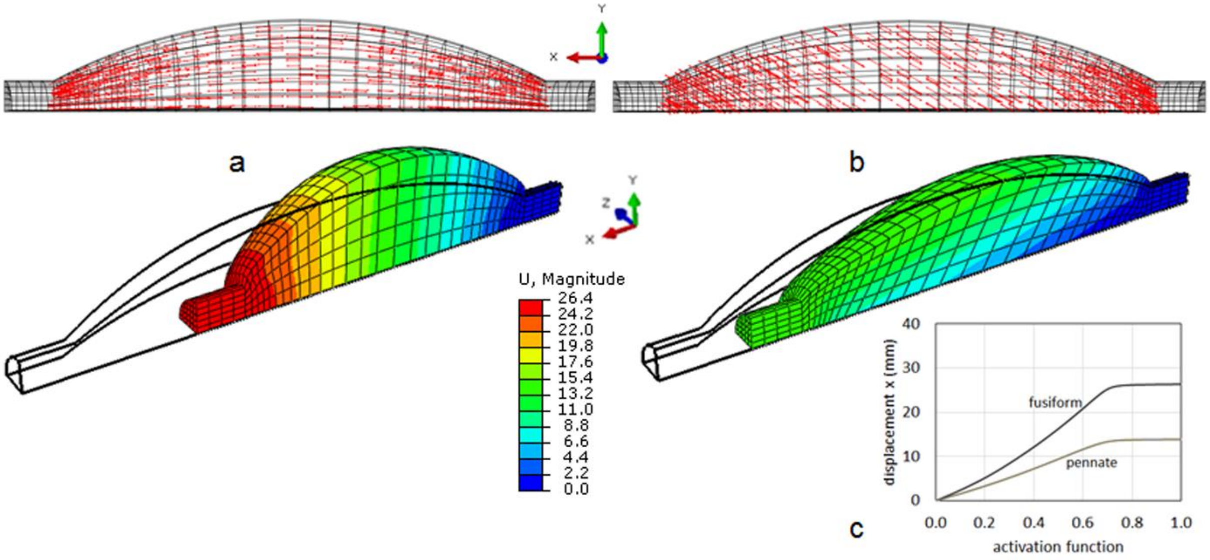

Figure 34 Effects of muscle fibers disposition (a, b) for an isotonic contraction at null imposed force [44].

For the investigation of muscles fascia interactions, particular attention is paid in evaluating the anterior compartment mechanical behavior during the foot dorsiflexion movement. This muscle contraction is simulated through a numerical analysis also considering an additional displacement of 2.5 millimeters imposed on the proximal extremity of the fascia in the distal-proximal direction. This latter has the purpose to mimic the mechanical traction performed by the over thigh structures. An isotonic contraction is applied simultaneously to all the muscle fibers inducing a muscles shortening, as it effectively happens during a dorsiflexion [44].

Figure 35 reports the displacement magnitude contour for two transversal sections (A, B) evaluated both in the undeformed and in the deformed configuration. These sections are chosen in the proximal portion of the muscle where the deformational field reaches the highest values due to the shape variation during the contraction. The maximum radial displacement is about 7 millimeters in the central section B, while it decreases to 5 millimeters in the upper section A [44].

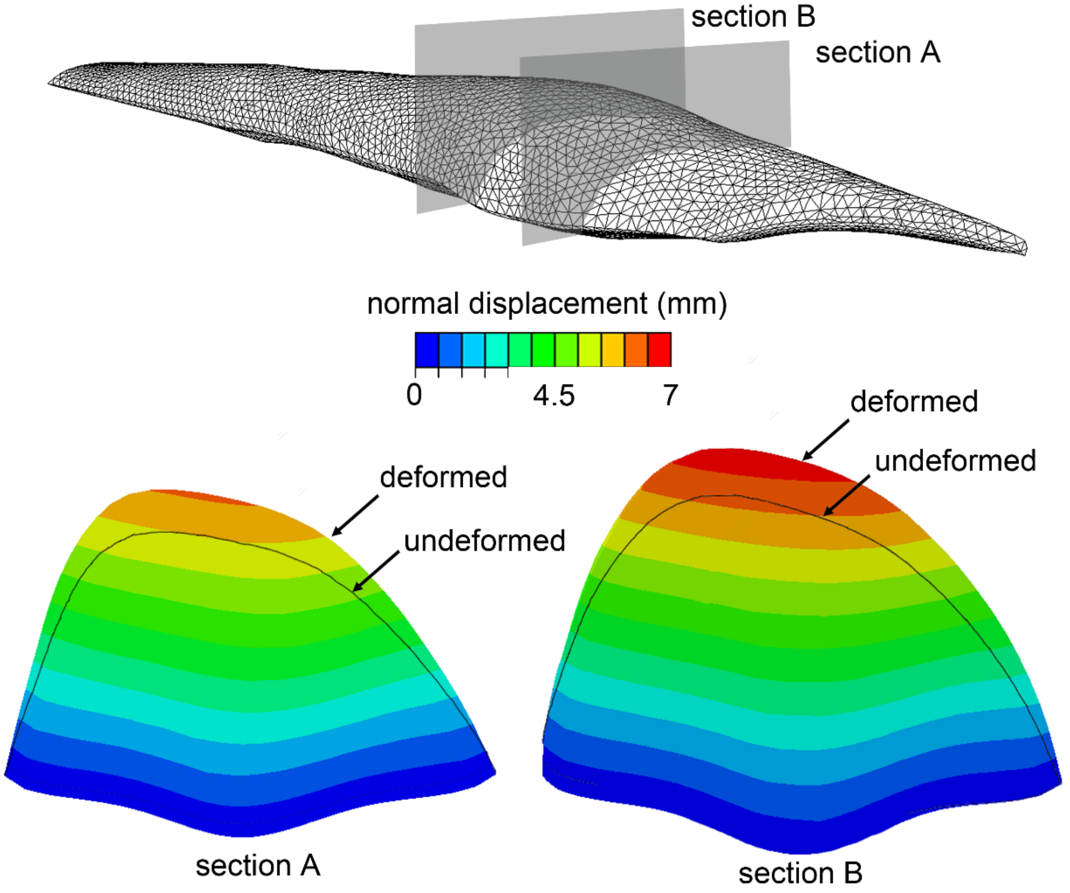

Figure 35 Comparison between undeformed and deformed configuration of the muscle structure by considering two different transversal sections. The normal displacement fields are also reported [44].

Figure 36 shows the contour of the maximum principal stress that is compared between the internal (a) and external (b) layers of the fascia highlighting an average value of about 1.5 MPa in the upper central region. Both these contours show a stress distribution and orientation due to the symmetric disposition of the fibers embedded in the two dense layers. This fact reflects in a feasible way the fascia structural composition as it appears from the histological analyses with the recognition of two almost mutual independent and fiber reinforced layers. In terms of deformations, also the computed corresponding strain field shows a homogeneous distribution with values up to 16% [44].

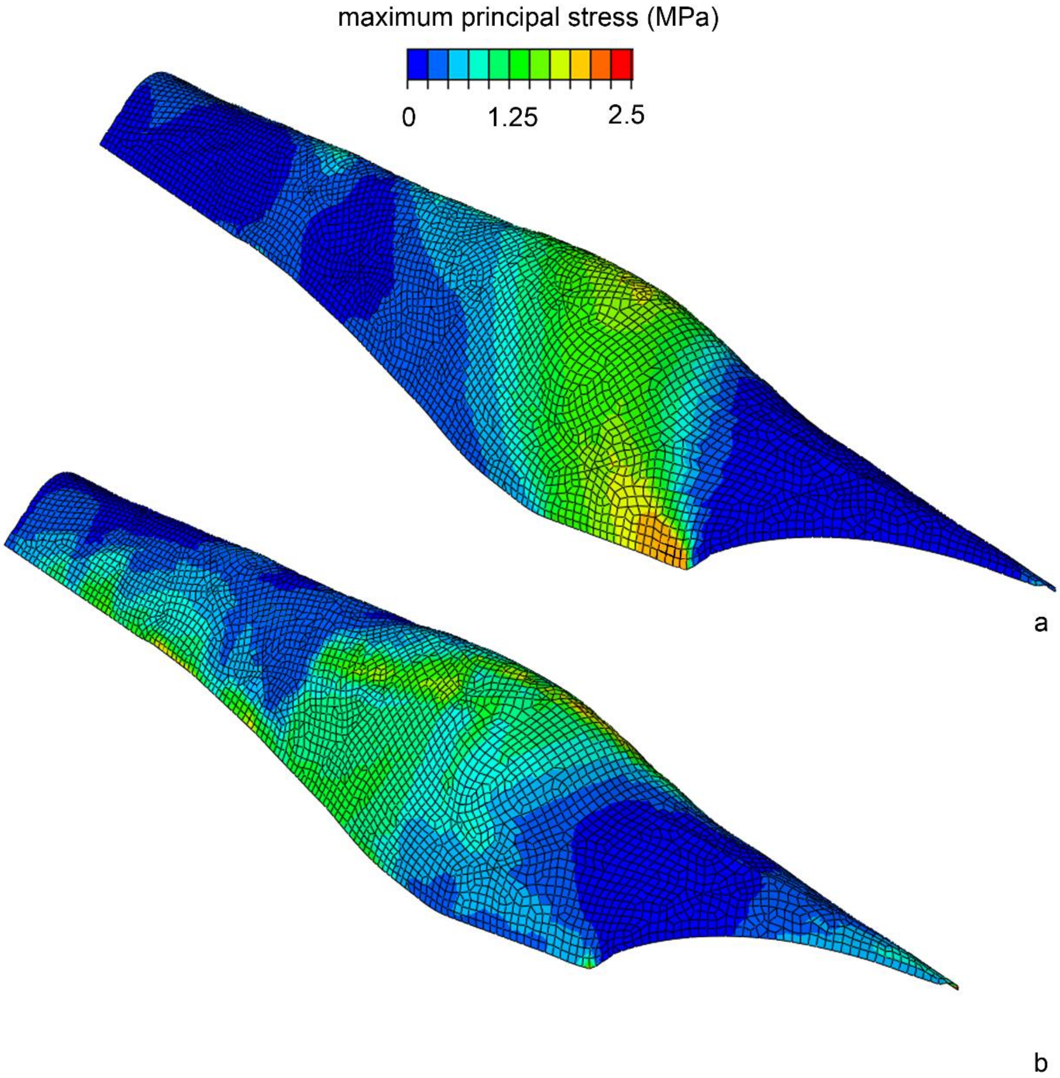

Figure 36 Contour of the maximum principal stress in the internal (a) and external (b) layer of crural fascia [44].

A partial validation of the numerical results can be performed by comparing the radial deformations evaluated by means of laser scanning (Figure 37) and those computed via numerical analysis (Figure 35). The simulated contraction phenomenon provides feasible results that are close to experimental measurements. For a direct comparison, the radial percentage increment is computed by taking into account a measure of the radial deformation normalized to the initial radial length. The radial percentage increment obtained via numerical model is 15.2%, while experimental results from laser scanning acquisition report a percentage variation of about 16.5%. These measurements are evaluated taking into account sections situated at the medial third, in upper central part of the fascial structure, where the contraction phenomenon exhibits its maximal effects [44].

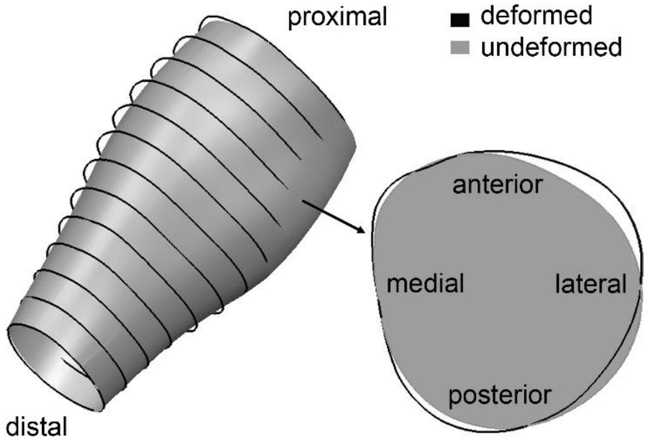

Figure 37 Laser scanning reconstruction of the leg external surface at rest condition (gray) with overlapping black lines corresponding to thirteen leg sections evaluated during the maximal dorsi-flexion contraction. On the right a detail of a leg section at the medial third [44].

An additional check to assess the model reliability is performed by considering the pressure field resulting from the concentric contraction within the anterior compartment. The average pressure value computed at section A (Figure 35) is 161.6 mmHg and it is comparable to those experimentally measured during concentric contraction by means of catheters inserted in the upper portion of the anterior compartment [61]. Analogous experimental data are reported by Friden et al. [62] who monitored the anterior compartment pressure on eight healthy subjects exercised by either concentric or eccentric contractions of the same load (400 submaximal contractions at constant rate, 20/min for 20 min at a load corresponding to 15% of individual maximal dorsiflexion torque). The average pressure measured during the concentric contraction is 157±16 mmHg.

The proposed model neglects the physiological force transmission between the muscle external surface and fascia internal layer due to the presence of connection fibers between these structures, mainly localized in the internal proximal region of the fascia. The quantity and the mechanical effects of these connections represent parameters of difficult quantification. Further, there are few knowledge about the real conformation of crural fascia connections and insertions in the lower and in the upper regions, at the height of the ankle and of the knee joints. As consequence, reasonable simplifications of the model are assumed [44].

The time-dependent behavior of the crural-fascia is here neglected but this approximation appears reasonable according to the loading rate characterizing the simulated contraction and the specific experimental data of intra compartmental pressure taken as reference [61].

Another simplification is introduced by modeling the four muscles enwrapped by the crural fascia as a unique volume characterized by a similar disposition of fibers, corresponding to the typical conformation of a fusiform muscle.

In spite of these limitations, the proposed model represents a reliable and an indirect method for evaluating the interaction between crural fascia and underlying muscular structures. This numerical approach provides a useful tool for a deeper understanding of scarcely investigated phenomena because of the high invasiveness of the required experimental practice. The proposed analysis gives preliminary information about different measures of interest and about the structural and functional behavior of this particular fascial tissue. Stress, strain and pressure magnitudes and distributions are provided in a physiological condition of dorsiflexion contraction. However, the model will allow to consider also different pathological scenario by varying the loading and the kind of mutual interactions of the different structures. As matter of example, a possible pathological condition could be given by a reduction of the mutual sliding between fascia layers or between fascia and muscle surface. The quantification of these mechanical interaction phenomena could be useful from a clinical point of view allowing the study of possible functional alteration related to specific pathological cases [44].

CHAPTER 4 BIOMECHANICAL ANALYSIS OF HEALTY, HERNIATED AND REPAIRED HUMAN ABDOMINAL WALL

4.1 Introduction

In general, a protrusion of any internal organ from its proper cavity is called hernia. The protruded part are usually enveloped in a bag that is formed by membrane with which the cavity is physiologically lined. This kind of pathology can arise in several parts of the body. As matter of example, a deficiency in the skull bones allows the protrusion of part of the brain and its surrounding membranes forming a hernia. Further, defects of the intercostal muscles permit part of the lung, with its pleura, to form a hernia of the contents of the chest. But the most significant example, because of its frequent occurrence, is represented by the abdominal hernia which consists in the protrusion of the viscera through a weakened region of the abdominal wall [63]. Viscera within the abdomen are numerous, some of them are very moveable, and others are weakly connected by peritoneal attachments with surrounding structures, being permanently exposed to size changes and relative situation, from sudden to gradual distension. Further, the contraction of the abdominal wall muscles decreases the abdomen cavity dimensions compressing bowels, this action has the effect to force viscera from their physiological situation. In addition, muscles and tendons have various apertures for the passage of vessels and nerves; these openings have usually the dimensions suitable for the purpose but often become so much relaxed to allow the viscera themselves to protrude. Finally, the muscle are sometimes imperfectly shaped and the viscera can pass through unnatural openings [63].

The abdominal cavity is not protected by any rigid structure, as osseous or cartilaginous tissues, therefore the protection and the support of this anatomical region is entirely due to the abdominal wall. As consequence, the integrity of the abdominal wall allows the physiological functioning of the abdominal cavity that is capable to sustain fast and dynamic situations (cough, vomiting, etc.)

or maintained pressure changes (obesity, pregnancy, etc.). Hernia occurrence can be due to several factor as increased abdominal pressure due to chronic cough, constipation, urinary obstruction, heavy lifting, obesity and family history [64]. Another important cause of the abdominal wall herniation is due to a weakening of the tissues and a consequent loss of stiffness. In the specific, the weakening of the front abdominal region can be secondary to trauma or congenital problems but it can also occur after operations at the site of the surgical incision, owing to improper healing or to excessive strain on the healing tissue. All these causes finally lead to a surgical intervention with the aim to strengthen or substitute the abdominal wall by means of different kinds of meshes characterized by pros and cons, due to their mechanical and biochemical characteristics, already discussed in Chapter 1. Independently on the selected mesh, this latter has to ensure mechanical characteristics that mimic the original response of healthy tissues. At this purpose, it is essential the investigation of the prosthetic tissue placement in the abdomen by considering its possible anisotropic properties in relation with those characterizing the abdominal wall. In the specific, the stiffer direction of the mesh must follow the direction where muscular effort is higher that coincides with the transversal direction, while the more compliant mesh direction must be placed perpendicularly to the previous one.

The objective of this study consists in analyzing the response of different prostheses in hernia surgery via computational techniques by defining a numerical model of the abdominal wall. This action requires reliable constitutive formulations of biological tissues together with a 3D virtual solid model of the abdomen structure. The constitutive formulation exploits experimental data taken from literature that supply a globally complete source of information about the mechanical behavior of the different abdominal wall structures. The development of the numerical model allows different kinds of analyses, firstly considering the healthy abdomen with the aim to assess its global mechanical behavior and the tissues functionality in physiological conditions. Then a hernia defects is introduced in the abdominal wall, with size and position in accordance to clinical evidences. Finally, the abdominal wall is virtually repaired by means of different kinds of grafts (biologic and synthetic) with the purpose to evaluate the mechanical interaction between native abdominal wall tissues and surgical meshes and to assess their mechanical compatibility. These analyses allow the comparison between physiological and pathological conditions letting possible the estimation of the stress and strain fields within biological tissues and prosthetics. The comparison between such fields with the corresponding physiological values in healthy conditions allows the definition of surgical optimization strategies and the choice of the best prosthesis configuration.

4.2 Abdominal wall anatomy and histology

The abdominal wall encloses the abdominal cavity, which holds the gastrointestinal viscera. Its main roles consist in forming a firm, flexible wall which keeps the abdominal viscera in the abdominal cavity, protecting the abdominal viscera from injury, maintaining their anatomical position against gravity, assisting in forceful expiration by pushing the abdominal viscera upwards and, finally, it is involved in any action (coughing, vomiting) that increases intra-abdominal pressure. The abdominal wall is composed of different layers that are, from the external to the internal, skin, superficial fascia or subcutaneous tissue, muscles and associated fascia, parietal peritoneum (Fig. 42).

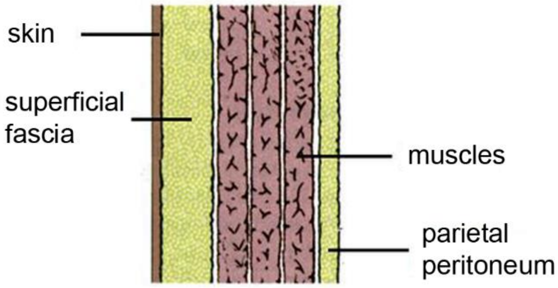

Figure 38 Layers of the abdominal wall

4.2.1 Superficial fascia

Superficial fascia composition depends on its location. In the region above the umbilicus it consists in a single sheet of connective tissue, which is continuous with the superficial fascia in other regions of the body. In the region below the umbilicus it is divided into two layers: the fatty superficial layer, known also as Camper's fascia, and the membranous deep layer, called Scarpa's fascia. This latter is a fibrous layer formed by compacted fibrous strata that distally merges with the deep thigh fascia and superficial perineal fascia to contribute to the fascia lata and Colles' fascia, respectively. Superficial vessels and nerves run between Camper's and Scarpa's fascia [65].

4.2.2 Linea alba, abdominal muscles and associated fascia

The strength of the anterolateral abdominal wall is mainly due to four paired muscles and their respective aponeuroses. These muscles are the rectus abdominis, the external oblique muscle, the internal oblique muscle and the transversus abdominis. In 80% of people there is also a small triangular muscle, called the pyramidalis. It originates from the pubic symphysis, that is located immediately below the rectus, and it is connected to the rectus sheath inserting into the linea alba. The pyramidalis muscle represents the tensor of the linea alba (Fig. 43) [64,65].

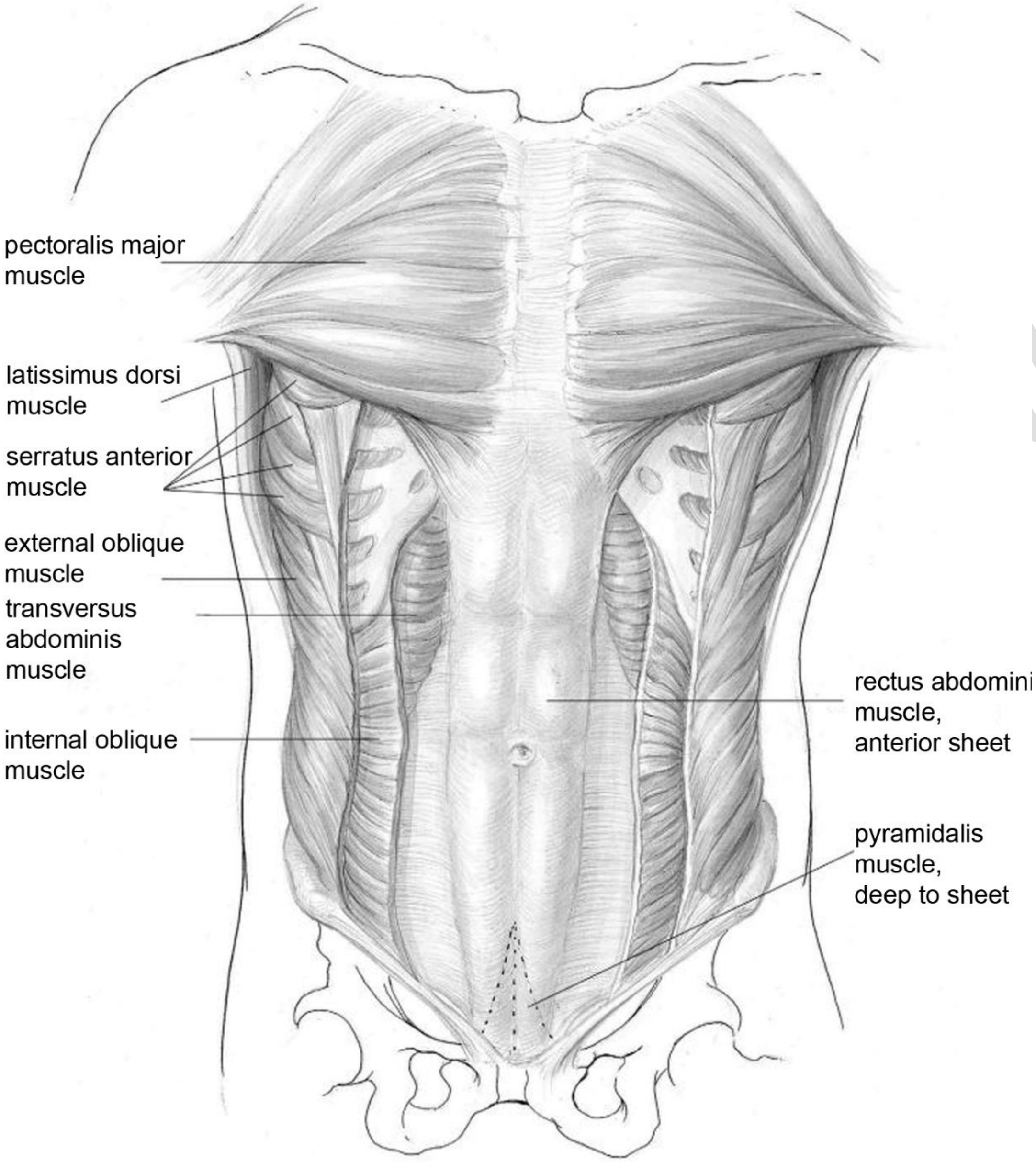

Figure 39 Muscles of the anterior abdominal wall [65].

4.2.2.1 Linea alba

The linea alba consists in a band of dense fibrous tissue, which is located between the medial borders of the rectus abdominis and extends from the xiphoid to the symphysis pubis (Fig. 44). It is composed by the fusion of the aponeurosis of the external and internal oblique and transversus muscles. The linea alba has usually a maximum width up to 1.25 - 2.5 cm [64].

4.2.2.2 Rectus abdominis muscle

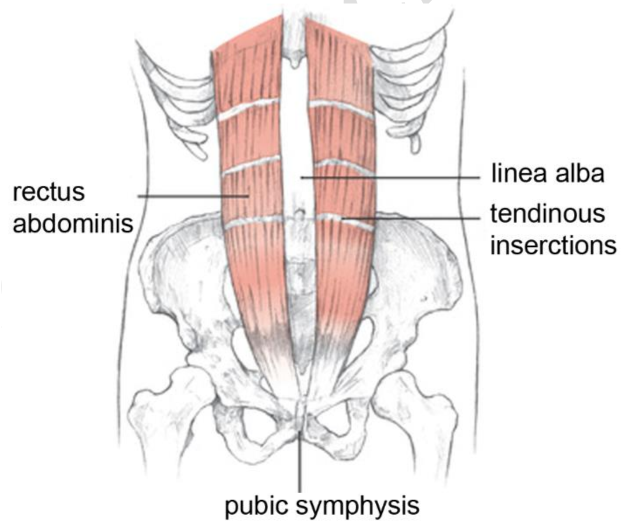

Figure 40 Rectus abdominis muscle.

The rectus abdominis is a vertical muscle of the anterior abdominal wall consisting in a pair of muscles symmetrically disposed with respect to linea alba. Its fibers follow the craniocaudal direction. The rectus muscle originates from the 5th through 7th costal cartilages to insert on the symphysis pubis and crest. Proximally, the rectus is wide, broad, and thin, becoming narrow and thick distally [65]. The rectus muscle is enveloped in a sheet, called anterior rectus sheet, derived from the combined aponeuroses and fasciae of the external oblique, internal oblique, and transversus abdominis (Fig 45). The rectus sheet has contributions from all the above-mentioned aponeuroses only in the region below the umbilicus (Fig. 45c). In the region over the umbilicus, the anterior sheet is only composed of aponeuroses from the external and internal abdominal muscles. It is possible to observe that the internal oblique aponeurosis splits, allowing one layer to pass anteriorly and one posteriorly to the rectus muscle (Fig. 45 b). The posterior sheet presents a similar composition described in relation to the umbilicus. Above the umbilicus it consists of contributions from both the aponeuroses of the internal oblique and the transversus abdominis. In the region that is below the umbilicus, the external abdominal aponeurosis gives no contribution to the formation of the posterior rectus sheet [65].

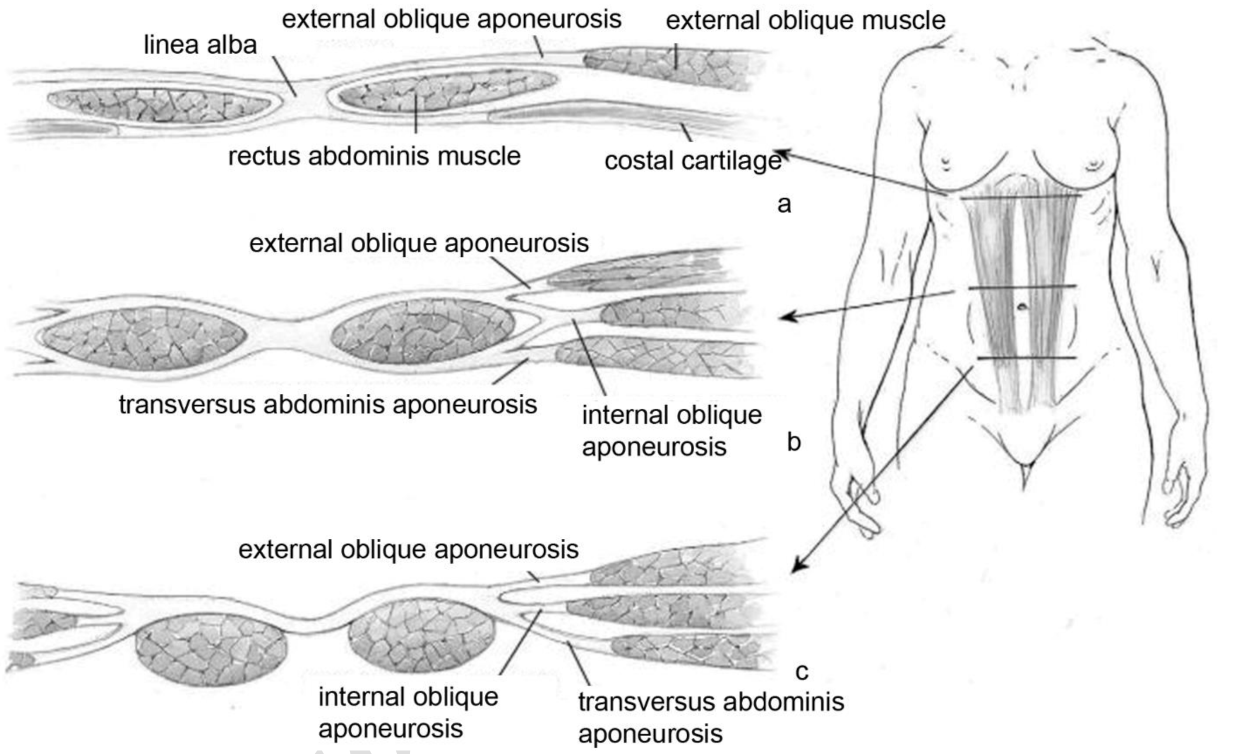

Figure 41 Rectus sheet structural conformation considered at three different heights [65].

The rectus abdominis muscle is involved in trunk flexion or elevation of the pelvis and thorax approach to the pelvis. Further, it collaborates in expiration and in keeping the tone of the abdominal wall. It also allows the abdominal press, which is the process that provokes an increase in the abdominal pressure that is necessary to perform specific physiological tasks (cough, urination, defecation, etc.) [64].

4.2.2.3 External oblique muscle

Figure 42 External oblique muscle.

The external oblique muscle is the largest and the most external of the three flat anterolateral muscles of the abdomen. It originates from the lower 8 ribs posteriorly to interdigitate with both the serratus and latissimus muscles. The direction of the fibers is approximately horizontal in the uppermost portion, while they become oblique in the lowest portions as they fold on themselves to form the inguinal ligament [65]. Further, this muscle is inserted within the external oblique aponeurosis, which merges to the anterior rectus sheet and the linea alba.

The unilateral action of the external oblique muscle allows the trunk rotation to the opposite side, trunk lateral bow and elevation of lateral pelvic edge. The bilateral actions consists in trunk bow forward, lifting the pelvis and contribution to abdominal press during expiration [64].

4.2.2.4 Internal oblique muscle

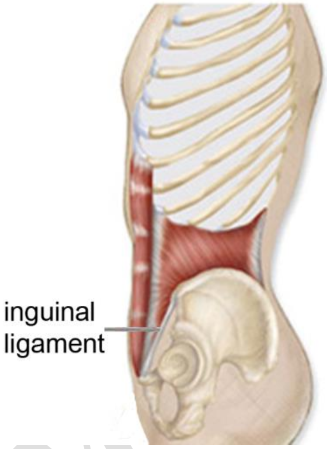

Figure 43 Internal oblique and rectus abdominis.

The internal oblique originates from the anterior two-thirds of the iliac crest and lateral half of the inguinal ligament. The fibers direction is approximately perpendicular to the external oblique fibers. Further, the fibers take the shape of the iliac crest in that they fan out to insert on the 10th to 12th ribs inferiorly [65].

The umbilicus represents an important level in the division of the internal oblique aponeurosis. Uppermost this level, the internal oblique aponeurosis splits to envelop the rectus abdominis and, subsequently, rejoins at the linea alba. In the region below the umbilicus the aponeurosis remains intact and runs anterior to the rectus to finally contribute to the linea alba [65].

The internal oblique muscle allows the unilateral contraction by rotating the trunk on the same side and forward, while the bilateral contraction occurs by bowing the trunk forwards and raising the anterior edge of the pelvis. Further, the internal oblique works in the press and abdominal expiration [64].

4.2.2.5 Transversus abdominis muscle

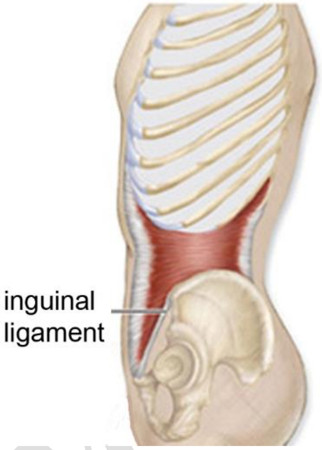

Figure 44 Transversus abdominal muscle

The transversus abdominis muscle is the deepest of the abdominal muscles. It originates from the 7th to 12th costal cartilages, iliac crest, and the lateral third of the inguinal ligament. The muscle fibers are mainly oriented with horizontal direction. As above-mentioned, the umbilicus represents an important landmark in the division of the transversus abdominis muscle fibers. In the region above the umbilicus the transversus abdominis aponeurosis joins the internal oblique aponeurosis to form a portion of the posterior rectus sheet. Below the umbilicus, the transversus aponeurosis only contributes to the anterior rectus sheet. The posterior face of the transversus abdominis muscle is attached to the fibrous tissue called transversalis fascia [65].

The transversus abdominis muscle allows the maintenance of the pressure and of the tone of the abdominal cavity. Further, it works in the rotation of the trunk to the same side, in the contraction and relaxation of the abdominal wall, and it plays a role in the press and abdominal expiration [64].

Several studies report about anthropometric measures of the abdominal muscles, in terms of length, width and thickness. Often, this kind of measure are performed with the aim to assess possible correlations between changes in muscles morphology and the arising of painful syndromes. As matter of example, investigations about Lower Back Pain (LBP) are performed by means of ultrasound tests that are used to evaluate muscles function, structure and activity and change in the thickness of abdominal muscles [66]. Measures on asymptomatic patients provide abdominal muscles physiological thickness that are reported in Table 5. For antero-lateral abdominal wall muscles (transversus abdominis muscle, internal oblique, external oblique), the measure is performed at the right side of the abdominal wall over the anterior axillary line, midway between the 12th rib and the iliac crest. As pertain the anterior abdominal wall muscle (rectus abdominis), the measure is taken at 2–3 cm above the umbilicus and 2–3 cm from the midline [66].

Muscle	**Thickness**	
	μ	SD
Rectus Abdominis	10.8	2.18
External Oblique	5.38	1.64
Internal Oblique	9.35	3.42
Transversus Abdominis	4.36	1.03

Table 5 Average abdominal muscles thickness (mm) and relative standard deviation for healthy subjects [66].

A regional variability in muscles thickness is highlighted, being the upper abdominal wall generally thicker than the lower portion. For this reason, the abdomen is usually divided into different regions in which repeated measures of interest are performed. As matter of example, in a study aiming to assess the fiber orientation within the abdominal muscles, the trunk is divided into three horizontal regions, as reported in Figure 49 [67].

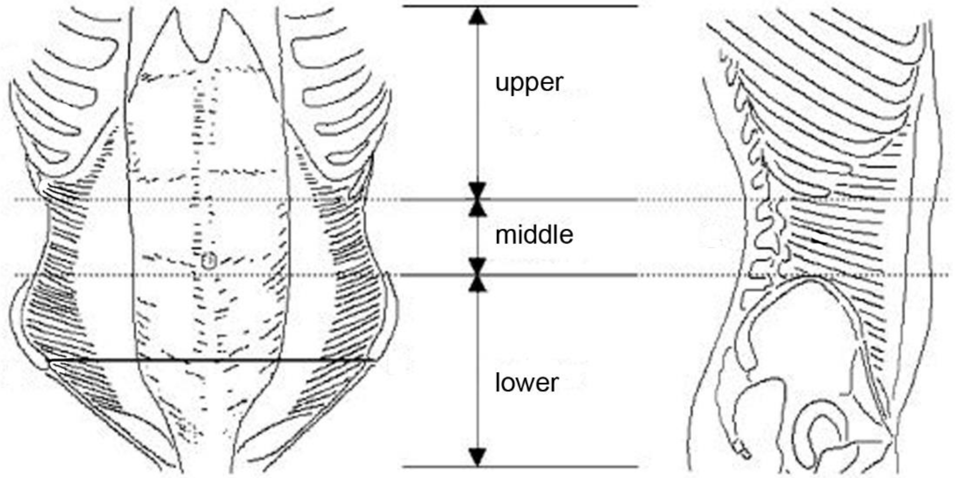

Figure 45 Anterior and lateral view of the upper, middle and lower regions of the abdominal wall. The black solid line on the left represents the line connecting the left and right anterior superior iliac spines (ASIS). This line is taken as lower limit reference for the performed measures [67].

The upper region extends from the 6th costal cartilage to the inferior border of the rib cage. The middle region is defined as the distance between the inferior border of the rib cage and a line connecting the superior borders of the iliac crest, while the lower region is measured from this line to the pubic symphysis. Table 6 reports the morphometric vertical dimensions of these regions and their percentage proportions with respect to the whole abdomen extension.

Region	**Vertical dimension**	
	μ (SD)	Proportion (%)
Upper	15.0 (3.3)	40
Middle	5.2 (2.1)	14
Lower	17.0 (2.6)	46

Table 6 Mean vertical dimensions (cm) and proportions of the upper, middle and lower regions of Figure 48 [67].

The fascicles orientation within muscles is measured in each region by means of image analysis. The line connecting the left and right anterior superior iliac spines (ASIS) is taken as horizontal reference (0°). According to this assumption, fascicles that are inferomedially directed present negative values of the orientation angle while, fascicle that lye on the superomedial direction have positive orientation. In Table 7 are reported the mean orientation angles of the fascicles fibers within the lateral muscles, measured in the different regions. Measurements in the lower region are performed at three different points: the first measure (Lower1) is taken at the height of the ASIS, the second one (Lower 2) two centimeters below the ASIS and the third measure (Lower 3) is performed in a region between ASIS and pubic symphysis.

	Fascicle orientation		
Region	External Oblique μ (SD)	Internal Oblique μ (SD)	Transversus Abdominis μ(SD)
Upper	-49.3 (7.0)	48.2 (12.9)	-2.7 (9.3)
Middle	-58.6 (10.5)	35.3 (9.9)	-13.3 (9.8)
Lower 1	-	0 (7.2)	-21.2 (10.5)
Lower 2	-	-8.2 (9.1)	-20.3 (11.3)
Lower 3	-	15.5 (10.3)	-

Table 7 Average fascicle orientation within different regions (deg). Lower 1 is at ASIS level, Lower 2 is 2 cm below ASIS, Lower 3 is placed halfway between ASIS and pubic symphysis. Negative values of fascicles orientation correspond to the inferomedial orientation, while positive values are referred to the superomedial orientation.

It is possible to observe that fascicles of the transversus muscle vary in their orientation between regions, being horizontal in the upper region, and becoming increasingly inferomedial in the middle and lower regions. As pertain the internal oblique muscle, it shows upper and middle fascicles that attach to the costal cartilages and iliac crest are oriented superomedially. This disposition is consistent with the movements of trunkflexion and rotation performed by this muscle. Regional differences in fascicle orientation are also highlighted in the external oblique muscle whose fascicles are oriented according to the inferomedial orientation. Eventually, the fascicles forming the rectus abdominis muscle are mainly oriented along the craniocaudal direction (90°) in all the considered regions, and for this reason, it is not reported in Table 7.

4.2.2.6 Transversalis fascia

The transversalis fascia is a connective sheet which covers the inner side of the whole abdominal wall. The collagen fibers follow the horizontal direction being almost perpendicular to the craniocaudal anatomical axis. In the uppermost region of the abdominal wall, this structure is a very thin sheet attached to the subperitoneal fascia, becoming stronger and more consistent distally. Therefore, the transversalis fascia covers the whole extension of the deep transversus muscle internal surface, except for the part of the transversus muscle aponeurosis which passes in front of the rectus abdominis, under the arch of Douglas. At this level, the transversalis fascia covers the back of the rectus muscle. Therefore, in this region, only the transversalis fascia and the peritoneum form the posterior rectus sheet. In the uppermost area the transversalis fascia is intimately merged with the diaphragmatic tissue [64].

4.2.3 Parietal peritoneum

The peritoneum is a thin membrane that lines the abdominal and pelvic cavities. It covers most abdominal viscera, being mainly composed of layer of mesothelium supported by a thin layer of connective tissue. In the specific, the parietal peritoneum is that portion of the peritoneum that lines the abdominal and pelvic cavities. These latter are also known as the peritoneal cavity. The parietal peritoneum is distinguished from the visceral peritoneum which covers the external surfaces of most abdominal organs, including the intestinal tract.

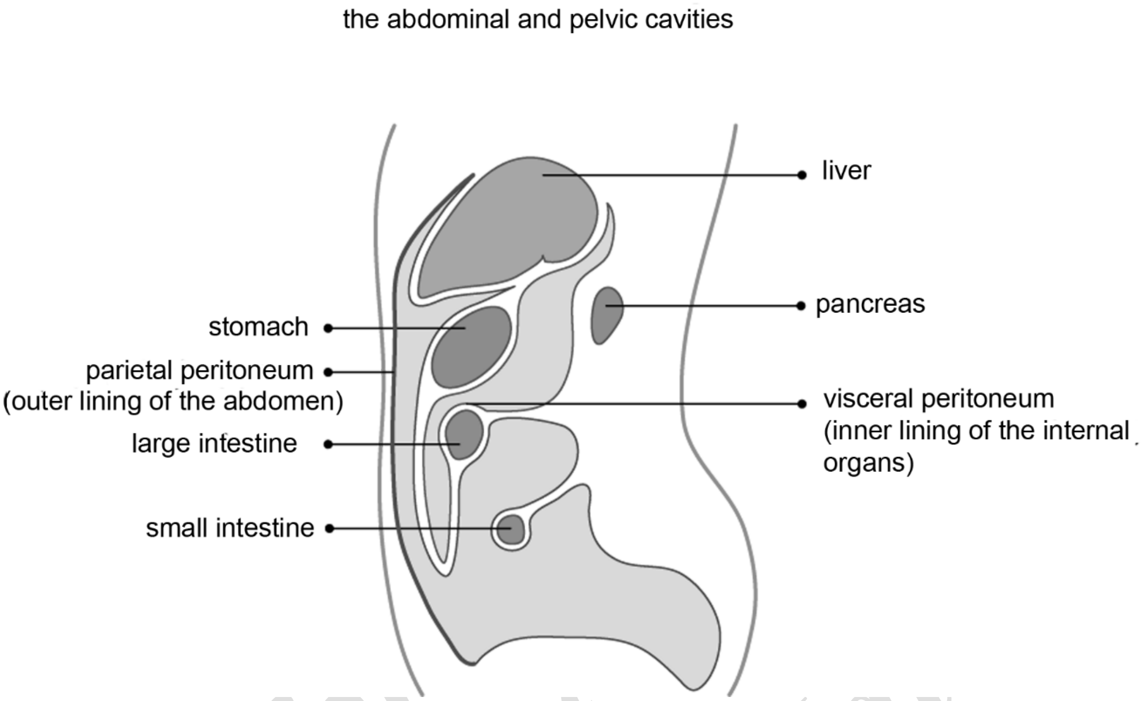

Figure 46 The abdominal and pelvic cavities. Parietal and visceral peritoneum are also highlighted.

4.3 Hernia origin and characteristics

As mentioned above, hernia consists in the protrusion of the viscera through a weakened region of the abdominal wall (Fig 38a), leading to the need of a surgical intervention with the aim to restore a condition which is as similar as possible to the initial physiological condition (Fig 38b).

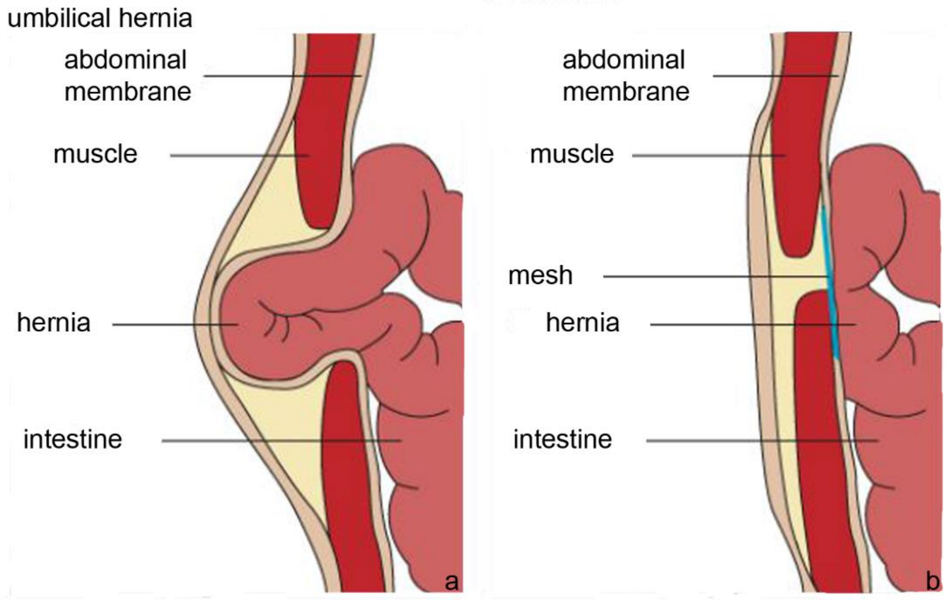

Figure 47 Schematization of an umbilical hernia (a) and its repair by means of a surgical mesh (b).

According to hernia size and position it is possible to perform a classification of these pathologies. Primary abdominal wall hernias show a shape that is usually round or oval. For this reason, the size can be described with one measurement, being width and length more or less comparable most of the time. Cutoff values of 2 and 4 cm are usually chosen to describe three subgroups according to size: small, medium and large [68]. According to the occurrence position it is possible to define hepigastric, umbilical, spiegel, inguinal and femoral hernia, as shown in Figure 39.

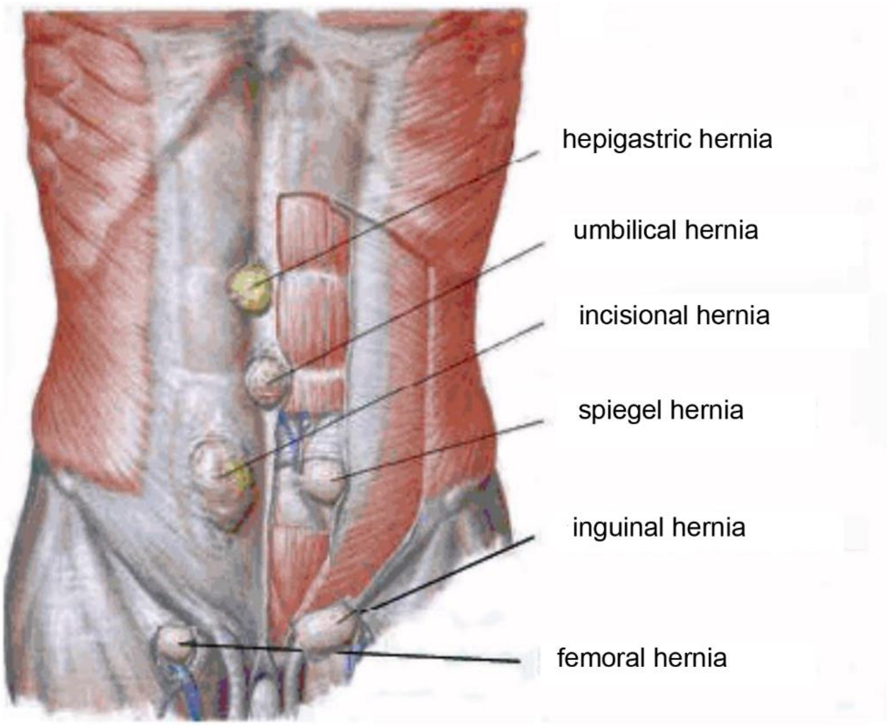

Figure 48 Different types of hernia [64].

Epigastric hernias are located in the midline between the sternum and the umbilicus. Umbilical hernia develops when the abdominal contents protrude because of the umbilical ring weakening. This specific kind of hernia is usually present from the birth due to a congenital weakness of the umbilical ring [64]. Spiegel hernia consists in the protrusion of preperitoneal fat, peritoneal sac, or organs through a defect in the spigelian aponeurosis that can be congenital or acquired. These hernias usually lie in the "spigelian hernia belt," that is a transverse 6-cm-wide zone above the interspinal plane [69]. Inguinal hernia occurs when abdominal contents, as intestine or bladder, protrude through a defect in the muscle wall of the inguinal region. It is possible to classify inguinal hernia into two groups: direct and indirect. Direct inguinal hernias are present when the abdominal contents, in particular the small intestine, pass through a muscle weakness and bulge in the area of the triangle of Hasselbach. Indirect inguinal hernias consist in the protrusion of the abdominal contents through the internal or deep inguinal ring. Hernia content descends along the spermatic cord until reaching the scrotum [64]. The femoral hernia usually appears in the groin or just below it, when a portion of intestine passes through the wall of the femoral canal, which contains the femoral artery, veins and nerves. It is located just below the inguinal ligament.

Different is the case of the incisional hernia that is defined as: "any abdominal wall gap with or without a bulge in the area of a postoperative scar perceptible or palpable by clinical examination or imaging'' [68]. Incisional hernias come in many different sizes and shapes. Therefore, the size of an incisional hernia is defined through its width and length measurements. The width of the hernia defect is defined as the greatest horizontal distance between the lateral margins of the hernia defect on both sides, while the length is defined as the greatest vertical distance between the most cranial and the most caudal margin of the hernia defect [68]. In case of multiple hernia defects, the width is measured between the most laterally located margins of the most lateral defect on that side and the length is measured between the cranial margin of the most cranial defect and the caudal margin of the most caudal defect, as shown in Figure 40 [68].

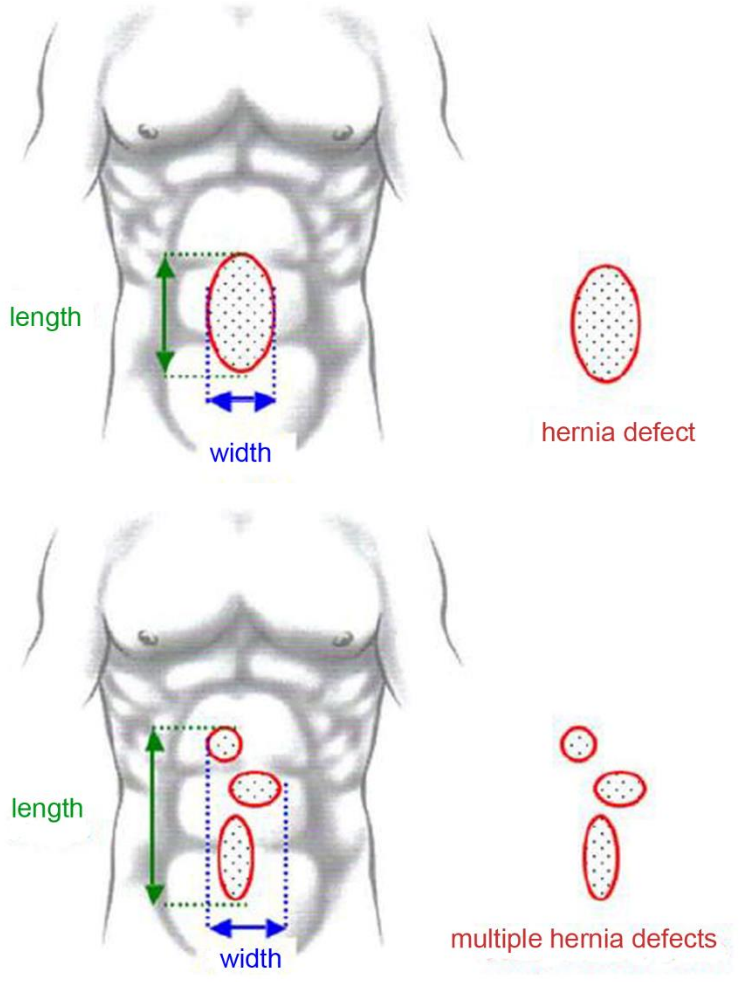

Figure 49 Definition of incisional hernia width and length both for single and multiple hernia defects [68].

Depending on the location and severity of the abdominal hernia, as well as patient medical history, ventral hernia repair surgery can be performed in two different ways. A first approach consists in the classic open surgery. The surgeon makes an incision in the abdominal region where the hernia is located, then intestine or tissue inside the hernia sac is placed back into the abdominal cavity. The hernia is repaired by means of a patch that is placed so that it covers and overlaps the hernia defect. Eventually, the skin incision is closed with stitches, staples, surgical tape, or special glue. The second surgical strategy of intervention is represented by the laparoscopic surgery. Several small incisions (usually from three up to six) are made in the abdominal wall surrounding the hernia. The patient abdomen is inflated with carbon dioxide gas. Surgical instruments and a laparoscope are inserted through the incisions into the abdomen and are used for repair the abdominal wall by means of a patch. Eventually the gas is released and the skin incisions are closed. Laparoscopic ventral hernia surgery offers potential benefits in comparison to classic open surgery, such as quicker recovery time, decreased pain, lower infection rate, reduced hernia recurrences, and fewer complications. The surgical patch can be positioned at different depths and it is possible to recognize four positions that are classified from the deepest to the most superficial as: intraperitoneal, preperitoneal, retromuscular prefascial and premusculoaponeurotic (Figure 41) [64].

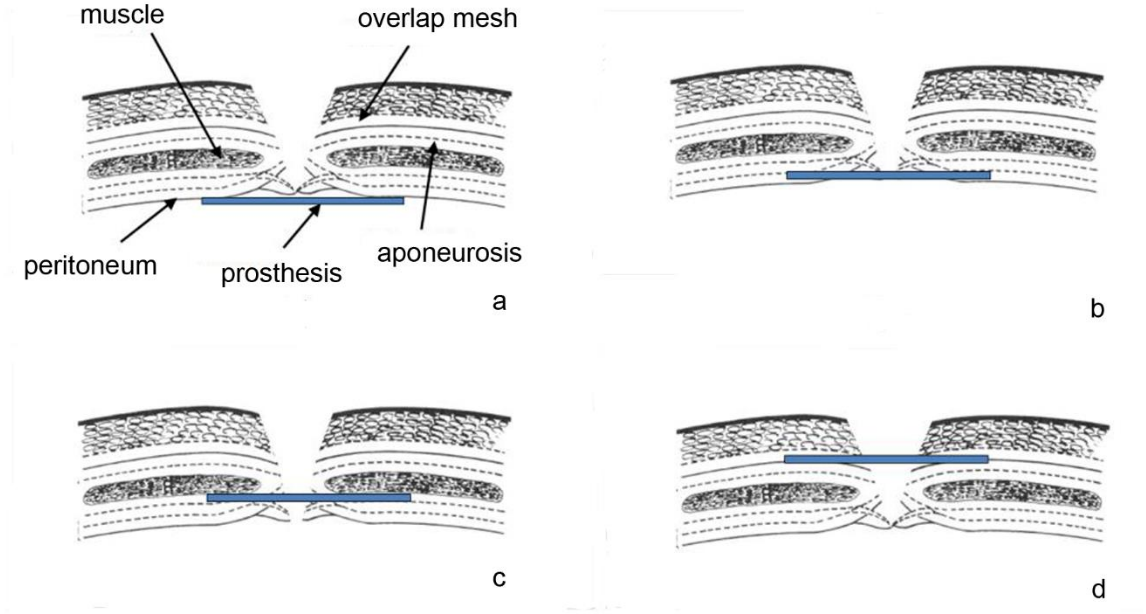

Figure 50 Positions of the prosthesis from the deepest to the most superficial placement: intraperitoneal (a), preperitoneal (b), retromuscular (c), and premusculoaponeurotic (d) [64].

In the intraperitoneal implantation, shown in Figure 41a, the prosthesis is placed into the deepest side of the abdominal wall with the advantage of avoiding any parietal dissection. Further, the pressure within the abdominal cavity helps the closure of the hernia defect.

In the preperitoneal implantation the prosthesis is placed in the deepest side of the wall directly opposite the peritoneum by simple apposition, or with the help of a stitch. With this technique the edges of the mesh protrude significantly from the opening limits and the peritoneum results to be reinforced [64].

The retromuscular prefascial implantation consists in the positioning of the prosthesis between the muscular body and its posterior fascia. The mesh is sutured externally and this technique requires the parietal dissection. Residual pain can appear due to accidental interposition of nerve fibers in the fixing points [64].

Eventually, in the premusculoaponeurotic implantation the purpose is to reinforce, with a prosthetic, a parietal repair using suture and autoplasty. The disadvantage of this technique is due to its superficial character which represents a cause of fragility when pressure increases. Further, any superficial infection or skin necrosis exposes the prosthesis. On the other hand, this position represents the best location for host tissue integration and vascularization [64].

4.3.1 Evaluation of the intra-abdominal pressure (IAP)

Intra-abdominal pressure (IAP) is the pressure within the abdominal cavity that increases with inspiration and decreases with expiration. It is directly affected by the volume of the solid organs or hollow viscera which may be either empty or filled with air, liquid or fecal matter. Further, the presence of ascites, blood or other space-occupying lesions, such as tumors or a gravid uterus, and the presence of conditions that limit expansion of the abdominal wall directly influence IAP. The evaluation of a normal range of IAP during typical activities of daily living is fundamental.

Elevations in IAP can have several adverse effects such as decreased cardiac output due to reduced venous return, reduced splanchnic and hepatic perfusion, and decreased renal blood flow and glomerular filtration rate [70]. Further, the role of IAP, as it pertains to hernia repair, has been widely investigated with the aim to correlate the elasticity and the tensile strength of the abdominal wall with those of prosthetic implants to assess the mechanical biocompatibility.

In a study carried out by Cobb et al., the IAP is measured in twenty healthy young adults with no prior history of abdominal surgery [70]. With the aim to reduce the measurements invasiveness, pressure readings are obtained through a transurethral bladder (Foley) catheter. Each subject is asked to performed 13 different tasks including standing, sitting, bending at the waist, bending at the knees, performing abdominal crunches, jumping, climbing stairs, bench-pressing 25 pounds, arm curling 10 pounds, and performing a Valsalva and coughing while sitting and also while standing. The minimum, the maximum and the average values of measured IAP during these different tasks are reported in Table 8.

Position	**Minimum (mmHg)**	**Maximum (mmHg)**	**μ (mmHg)**	**SD (mmHg)**
Supine	-1	6	1.8	2.2
Standing	15	27	20	3.8
Sitting	10	21	16.7	2.9
Stairs	40	110	68.9	17.4
Abdominal crunch	7	47	26.7	10.7
Bend at waist	6	30	14.4	5.3
Bend at knees	14	30	20.6	4.4
Cough	40	127	81.4	25.6
Standing cough	64	141	107.6	23.0
Valsava	20	64	39.7	11.0
Standing Valsava	32	116	64.9	22.0
Jumping	43	252	171	48.4
Bench press	2	34	7.4	7.3
Arm curl	17	37	25.5	6.0

Table 8 Range of pressure for each performed task [70].

Results of this study highlight an increase of the intrabdominal pressure with the BMI but no correlation are found with the patient gender. Further, the highest IAPs in healthy, nonobese patients are generated during coughing and jumping [70].

Calculations performed in several studies are addressed to the evaluation of the maximum tensile strength of the abdominal wall. In a study performed by Klinge et al. [71] the abdominal wall stress is computed by means of Mariotte law applied to a thin-walled spherical shell under the action of a hydrostatic pressure (Fig.51). Mariotte equation is expressed as:

$$\sigma = \frac{Pr}{2t} \tag{4.1}$$

being P the hydrostatic pressure, r the radius of the spherical shell and t the shell thickness.

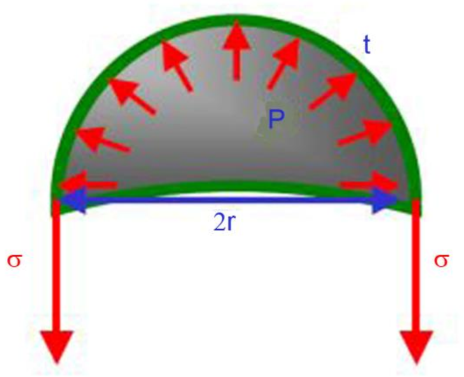

Figure 51 Thin-walled spherical shell.

The authors refer that, in humans, the intrabdominal pressure ranges from 0.2 kPa, at rest, to 20 kPa, which is the maximum. With the assumption of an abdominal wall thickness of 0.08 cm and an intra-abdominal pressure of 20 kPa, the abdominal tensile strength results to be about 196 N/cm^2. In the case of a 2 cm thick layer the tensile strength is reduced to only 7.8 N/cm^2 [71]. It is also possible to compute the total tensile strength, expressed as the tension strength multiplied by the retaining area, which is independent of the thickness of the layer. Therefore, at the upper physiological limit of 20 kPa, if the longitudinal diameter of the human abdominal wall is 32 cm it results in a tensile strength of 16 N/cm of the circumference. The values of 16 N/cm is commonly adopted as the average upper limit reference that any surgical mesh has to withstand.

4.3.2 Three dimensional model of the abdominal wall

4.3.2.1 Virtual solid model

The virtual solid model of a healthy subject is developed starting from histomorphometric data from literature and diagnostic images from Computer Tomography (CT) by means of a specific segmentation software. This latter allows to distinguish the different abdominal structures on the basis on their radiodensity, according to the Hounsfield scale, letting possible their three dimensional reconstruction starting from the single CT slices. By means of this procedure it is possible to define the volumes of linea alba, rectus abdominis muscle, aponeurosis and a structure comprising all the lateral muscles, namely the internal oblique (IO), transversus abdominis (TA) and external oblique (EO) [72].

Figure 52 Three dimensional reconstruction of linea alba (light blue), rectus abdominis muscle (fuchsia), aponeurosis (green) and oblique muscles (yellow).

Exploiting the abdomen symmetry, it is possible to split the structure along the longitudinal axis at the linea alba and model only one half of the abdomen with evident computational advantages. The choice of the right or left half is not significant because no substantial differences between them are highlighted.

The following step for the development of the solid model consists in the smoothing and regularization of the rough surfaces obtained via images segmentation. This is performed by means of a specific software that allows to reach a homogeneous surface of the whole structure as shown in Figure 53.

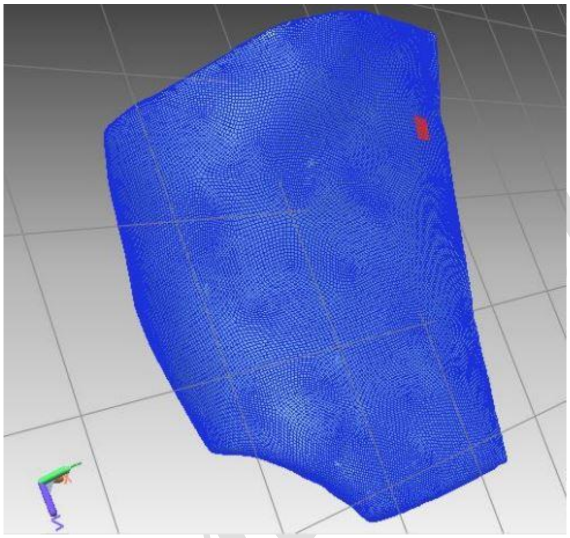

Figure 53 Side view of the smoothed and regularized surfaces of the abdominal structure.

In a subsequent step it is possible to complete the development of the virtual solid model by means of the reconstruction of the single structure surfaces by means of the definition of suitable separation surfaces between them. The results of this operation is reported, exploiting the symmetry, for the whole abdomen in Figure 54a. Once the solid model of the healthy abdomen is obtained, it is possible to introduce a virtual incisional hernia characterized by an elliptic shape with dimensions of 24 mm x 32 mm as shown in Figure 54b. It is introduced along the linea alba over the umbilicus with the major axis oriented along the craniocaudal direction. Hernia size and position are chosen in accordance to clinical evidences.

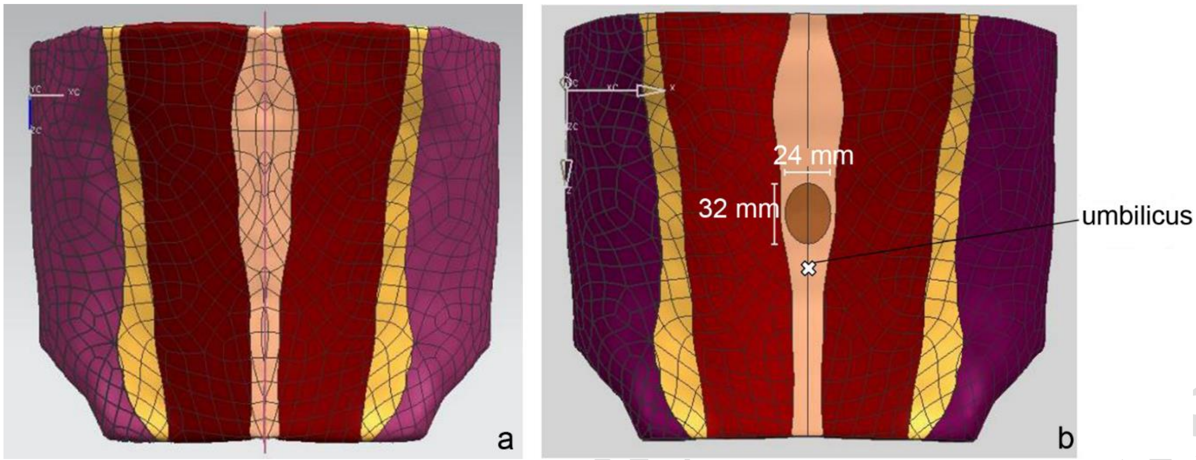

Figure 54 Virtual solid model of the healthy abdominal wall (a). Herniated abdominal wall (b).

According to commonly adopted surgical procedures, the mesh is cut with a rectangular shape having dimensions that exceed the hernia dimensions of 50 mm at each side of the elliptic defect. Therefore, the adopted mesh is 132 mm x 124 mm and it is positioned with the minor side along the craniocaudal direction as shown in Figure 55. The mesh is usually sutured with special tacks (Fig. 55b) that are placed leaving a distance of about 10 mm from the external side of the mesh (blue rectangle of Figure 55a). Each tack is placed at a distance of about 20 mm from the previous one.

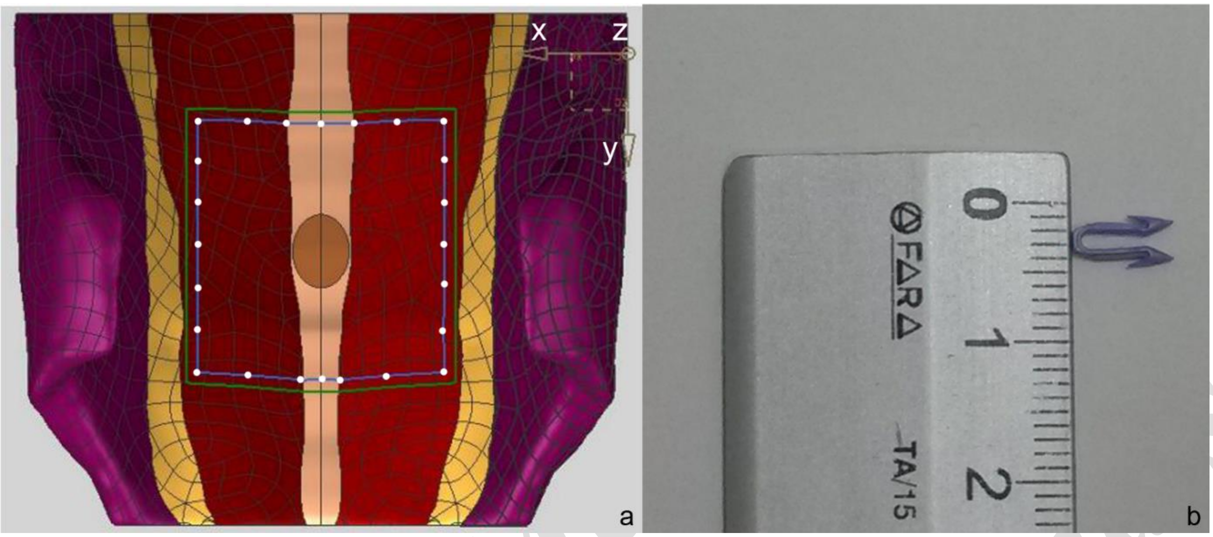

Figure 55 Internal side of the abdomen cavity (a). The green rectangle represents the mesh perimeter while the inner blue rectangle represents the ideal line on which the tacks are placed at a distance of about 20 mm from the previous one (white dots). On the right, the typical tack used for mesh fixation (b).

4.3.2.2 Numerical model

The numerical model is obtained by the discretization of the solid model by means of CAE ABAQUS® software (SIMULIA, Daussault Systems). All the three dimensional structures, namely linea alba, aponeurosis, rectus abdominis muscle and oblique muscles are discretized by tetrahedral elements. At this step, the fascial tissues covering the muscles, are created as two dimensional three node membrane element on the surfaces of the underling three dimensional solid elements (skin). In this way it is possible to create and model the anterior and the posterior rectus sheets, covering the rectus abdominis muscle, and the transversalis fascia. This latter consists in a membrane sheet which covers the whole internal abdominal wall [72]. Eventually, the surgical mesh is obtained with the same procedure and it is discretized by means of three nodes shell elements.

4.3.2.3 Loading and boundary conditions

With the aim to reproduce the physiological boundary conditions, possible translations along the three axis are not allowed in the upper and lower sides of the abdominal wall. These boundaries simulate the insertion of the modeled structures on the ribs and on the xiphoid process in the upper region, and the insertion on the pelvis in the lower portion. Also the extremities of the lateral muscles are considered fixed because of their physiological connections to the costal cartilages of the ribs, to the thoracolumbar fascia and to the iliac crest.

As mentioned-above, the abdomen mirror symmetry is exploited to split the model and to analyze only its left portion to reduce the analysis run time and the required memory. For this reason a symmetry displacement condition is achieved by imposing null displacements in the transversal direction (x in Fig.55a) and allowing displacements on the plane of symmetry (z in Fig. 55a).

A contact surface is defined between the surgical mesh and the underling structures of linea alba and rectus abdominis muscle. Null friction is considered to account the condition of relative sliding between these structures with the exception of the points simulating the tacks in which the corresponding nodes of the mesh and of the biological structure are merged together to mimic the stitches.

Contacts surfaces between fascial sheet and underling solid elements are tied together. This is a reasonable simplification for the purpose of the model which takes into account the fascial stiffness contribution to the overall structure stiffness avoiding negligible complications and consequent increasing in computational cost because of the presence of additional contact surfaces in mutual sliding.

4.3.3 Constitutive formulation for the abdominal wall components

4.3.3.1 Biological structures

The biomechanical behavior of the all considered biological structures is modeled by the adoption of a fiber-reinforced and almost-incompressible hyperelastic constitutive model, already described in the previous chapter. Recalling the formulation it is possible to express the energy density function as:

$$W_f = W_{fm} + W_{ff} = \left[\frac{\mu_f}{2}\left(\tilde{I}_1 - 3\right) + \frac{k_{fv}}{2}\left(J^2 - 1 - 2\ln J\right)\right] + \frac{\alpha_{f1}}{2\alpha_{f2}}\left[\exp\left(\alpha_{f2}\left\langle \tilde{I}_4 - 1\right\rangle^2\right) - 1\right] \quad (4.1)$$

where it is exploited the decomposition in volume-changing and volume-preserving components and the summation of different contributions due to the ground matrix and fibers mechanical response is taken into account. Even in this case, the formulation accounts for a family of collagen fibers appointing local transversal isotropic properties. k_{fv} is related to the initial bulk modulus of the ground matrix, μ_f represents its initial shear stiffness. α_{f1} (stress-like) and α_{f2} (dimensionless) are constitutive parameters related to the fibers mechanical response.

The constitutive parameters identification is performed by means of optimization procedures, exploiting experimental data from literature.

4.3.3.1.1 Linea alba

A study carried out by Förstemann et al. [73] reports about mechanical tests on sixty human fasciae taken from linea alba. Fasciae are cut into smaller specimens along both the craniocaudal and transversal direction. Specimens are tested at room temperature in quasi-static conditions (strain rate ≈ 0.5%/s). Experimental data show a strong anisotropic behavior of this structure that is stiffest along the transversal direction than in the craniocaudal direction. A first optimization is performed along the less stiff direction for the determination of the ground matrix stiffness.

Then, exploiting this parameter, the fitting procedure is performed on data from the stiffest direction, the transversal one, that is considered, as a reasonable simplification, the main mechanical response of the linea alba which corresponds with the model fibers disposition. The average experimental data along the transversal direction and the numerical results from the data fitting are reported in Figure 56. Corresponding values of the constitutive parameters are reported in Table 9.

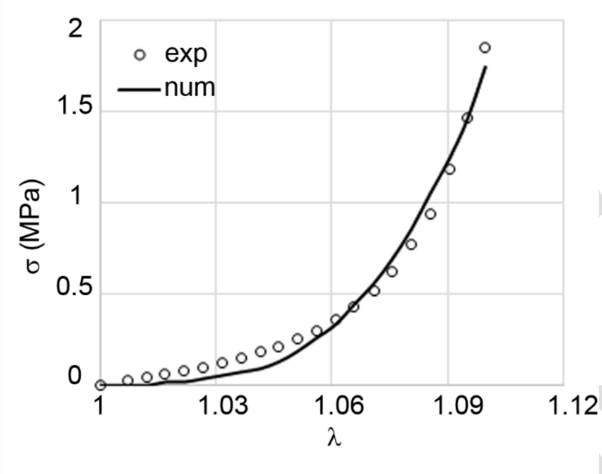

Figure 56 Stress-stretch behavior for the transversal response of the linea alba in terms of Cauchy stress versus stretch. The black solid line is the curve obtained by the numerical model, while open circles represent experimental data for the transversal direction.

k_{fv} (MPa)	μ_f (MPa)	α_{f1} (MPa)	α_{f2}
2000	0.26	0.45	45.68

Table 9 Constitutive parameters obtained by the best fit of the experimental tensile tests.

4.3.3.1.2 Rectus sheet

A study, by Abdelounis et al. [74], concerning the biomechanical characterization of the anterior rectus sheet is taken into account for the characterization of the whole fascial tissues of the model. Seventeen specimens are harvested from three different subjects. Specimens are cut along the medial-lateral direction ensuring a gauge length of 20 mm and a width of 5 mm. The thickness is evaluated by means of images analysis and has a mean values of 1.2 mm. Tensile tests are performed in quasi static conditions by applying a strain rate of 1%/s. Even in this case, for sake of simplicity, it is adopted the presence of a family of fibers disposed along the medial-lateral direction. Data fitting and constitutive parameters are reported in Figure 57 and Table 10.

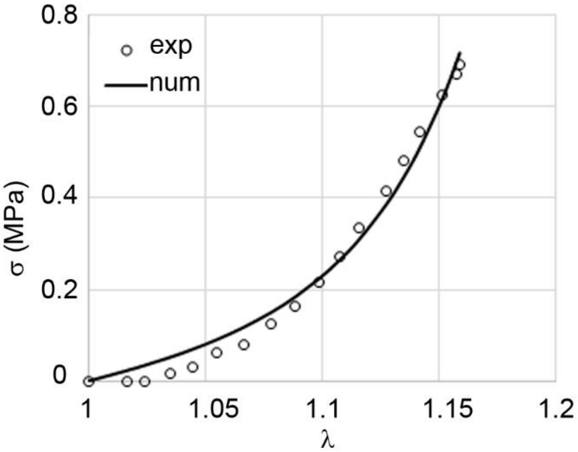

Figure 57 Stress-stretch behavior for the transversal response of the anterior rectus sheet in terms of Cauchy stress versus stretch. The black solid line is the curve obtained by the numerical model, while open circles represent experimental data for the transversal direction.

k_{fv} (MPa)	μ_f (MPa)	α_{f1} (MPa)	α_{f2}
2000	0.02	0.31	7.71

Table 10 Constitutive parameters obtained by the best fit of the experimental tensile tests.

4.3.3.1.3 Rectus abdominis, internal oblique, external oblique and transverse muscles

A study carried out by Cardoso [75] is focused on the biomechanical characterization of rectus abdominis, internal oblique, external oblique and transverse abdominal muscles. All the samples are excised from human donors during autopsies by means of dissecting the abdominal wall from the exterior layer inwards. Uni-axial tensile tests are performed on muscles tissues specimens that are cut along the fibers direction, with an average length of 50 mm and an average width of 25 mm. The samples are tested within the 24 hours after the dissection. Before mechanical testing, tissues are cut into smaller specimens having rectangular shape and are fixed to the experimental apparatus grips by means of Velcro with the aim to avoid any possible slipping. The thickness measurement is performed by means of a digital caliper. All the mechanical tests are performed in hydrated condition at a temperature of 37° C and consist in an elongation up to failure at a constant displacement rate of 5 mm/min. Data fitting are performed by taking into account the effective thickness of each muscle. Fitting curves and corresponding constitutive parameters are reported in in the following.

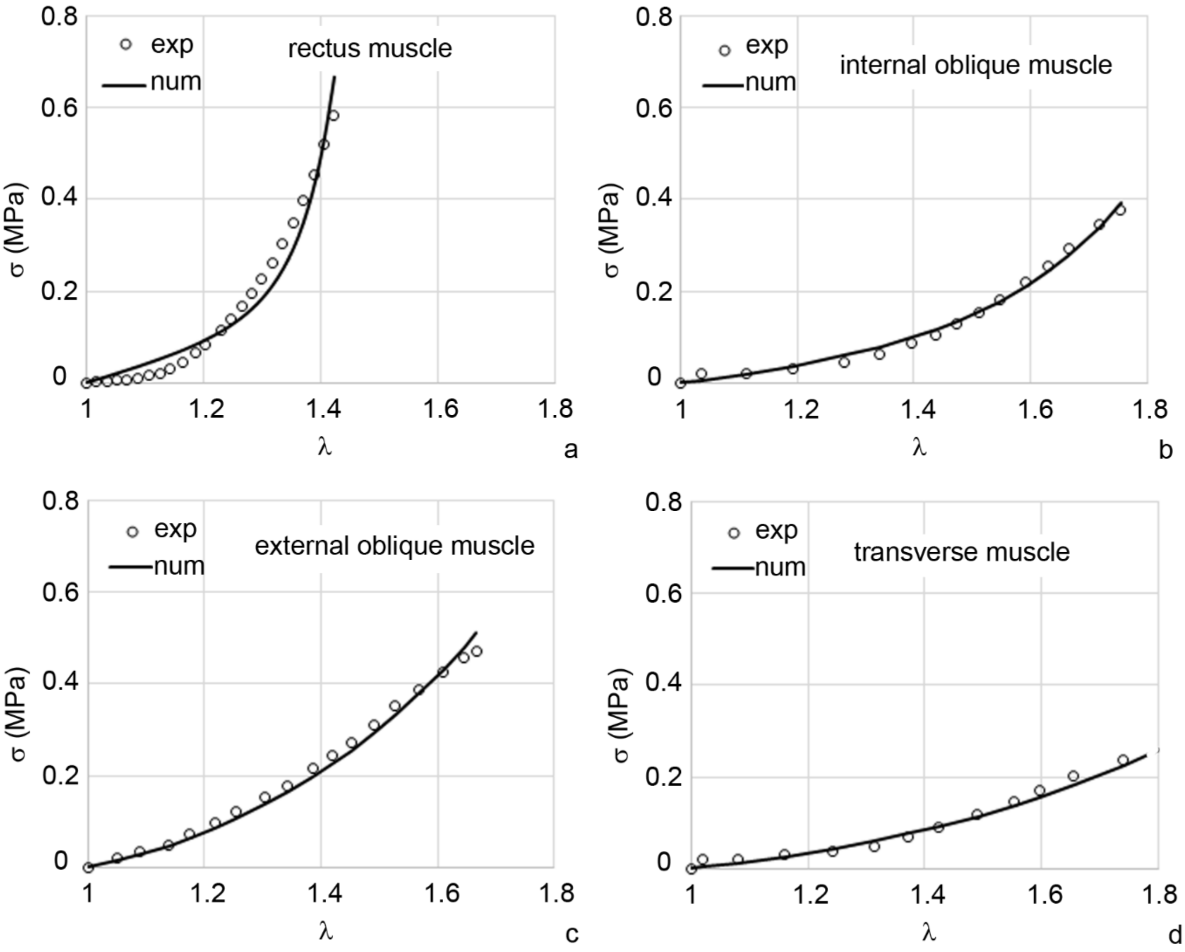

Figure 58 Stress-stretch behavior for the mechanical response of the rectus abdominis muscle (a), internal oblique muscle (b), external oblique muscle (c) and transversus muscle (d) evaluated along the fibers direction in terms of Cauchy stress versus stretch. The black solid line is the curve obtained by the numerical model, while open circles represent experimental data.

	k_{fv} (MPa)	μ_f (MPa)	α_{f1} (MPa)	α_{f2}
Rectus muscle	2000	0.056	0.308	7.708
Internal oblique muscle	2000	0.007	0.007	0.127
External oblique muscle	2000	0.004	0.012	0.0
Transverse muscle	2000	0.003	0.003	0.0

Table 11 Constitutive parameters obtained by the best fit of the experimental tensile tests for each muscular structure.

4.3.4 Numerical analysis and results: the physiological condition

A uniform intrabdominal pressure of 0.023 MPa is applied to the internal surfaces of the whole abdomen. This high pressure value, corresponding to 172.5 mmHg, is chosen to span all the possible physiological IAP values usually recorded during common daily tasks (the highest limit in measured while jumping and it is about 171 mmHg). With the aim to assess the model global reliability, three different internal abdominal pressures corresponding to the standing position (20 mmHg), standing cough (81.4 mmHg) and jump (171 mmHg) are analyzed. Results are reported, in terms of magnitude displacements contours, for the rigth part of the abdomen structure exploiting its symmetry. Figure 59 and 60 make possible the comparison among the magnitude displacements computed during the three chosen conditions: standing (a), standing cough (b), and jump (c) for the front and the side view [72].

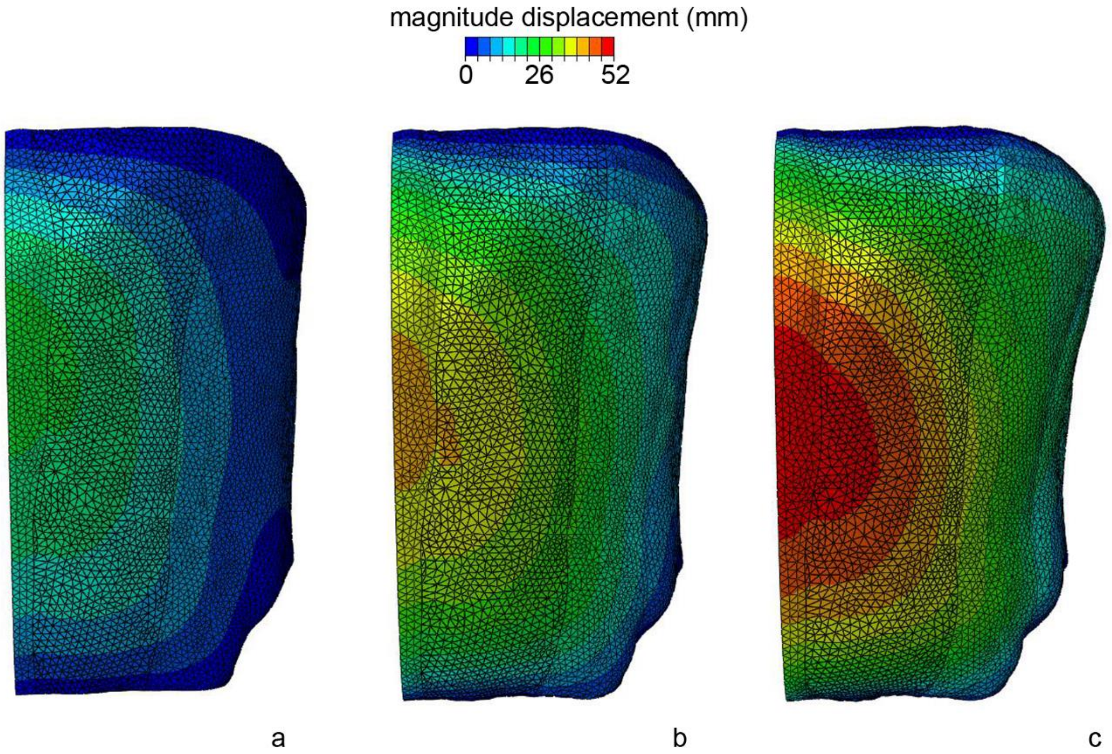

Figure 59 Front view of the magnitude displacement contour computed on the left abdomen side.

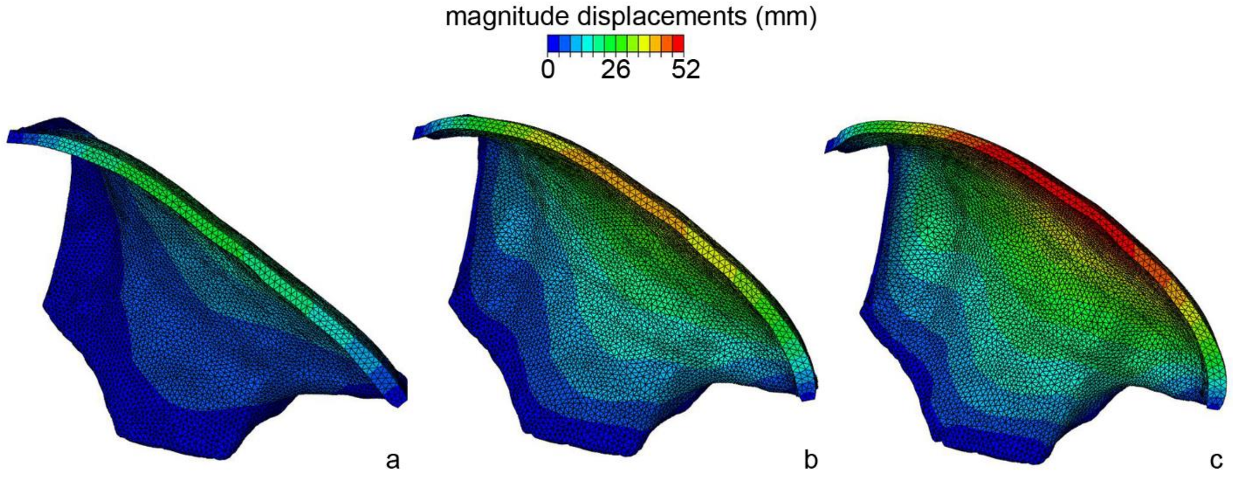

Figure 60 Side view of the magnitude displacement contour computed on the left abdomen side.

Numerical results show a maximal displacement of 23.85 mm in the center of the abdomen during the standing position. This value increase up to 41 mm in the standing cough condition and to 51.9 mm in the jump. The same results can be plotted, as shown in Figure 61, for two different paths of nodes chosen along the craniocaudal (blue) and the transversal direction (red) evaluated during the standing position (1), the standing cough (2) and while jumping (3).

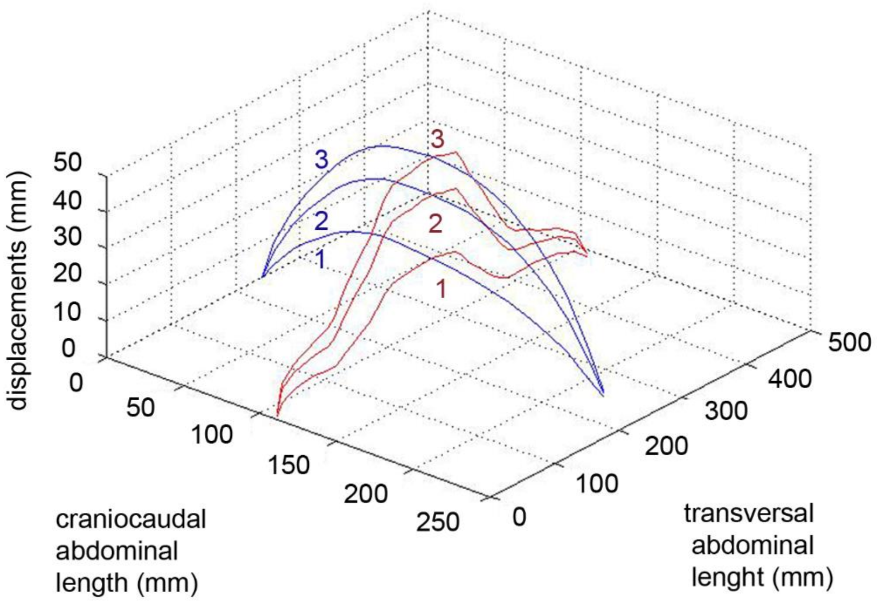

Figure 61 Magnitude displacements evaluated along the craniocaudal (blue) and the transversal direction (red) during the standing position (1), standing cough (2), and while jumping (3) .

These numerical results are validated by means of comparison with the few literature remarks about the healthy abdomen mechanical properties. In a study carried out by Konerding et al. [76], the effects of an increase of the intrabdominal pressure on the abdominal wall is experimentally investigated with the aim to reach a better understanding of the linea alba biomechanics. In the reported human cadaver study, including 7 subjects, the increasing IAP is simulated by the insertion of a balloon which is increasingly filled with water to reach the maximal pressure of

150 mmHg. Colored markers are directly glued on the anterior side of the abdomen by means of a grid characterized by widths of 3 cm which is exploited to measure the local deformation by means of a video camera. Authors report that the ultimate inflation of the peritoneal cavity results in a strain of the linea alba in craniocaudal direction by 16.5 ± 4.6% [76]. The same measure is computed on the numerical model by comparing the undeformed and the deformed configuration at the pressure of 150 mmHg obtaining a strain of 15.24% along the linea alba (Fig. 62).

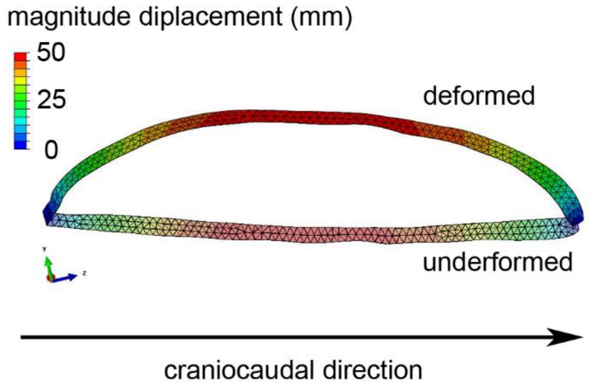

Figure 62 Comparison between the undeformed and deformed side section of the abdomen, taken along the craniocaudal direction [72].

The same authors report of measures of transversal load forces ranging between 29.6 N/cm and 52.2 N/cm that are higher if compared to the upper physiological limit of 16 N/cm which is conventionally adopted [71]. It is possible to compute the same measure of transversal load forces by taking the stress values of the different structural components (fasciae and rectus muscle) and multiplying these stress values by the thickness of the considered structure. This computation is performed by averaging values from different measures taken along a path of nodes oriented in the transversal direction and obtaining a transversal load force of 37.38 N/cm that is within the range of the experimental measures [72].

Another research carried out by Song et al. [77] consists in the study of the movement and change of the abdominal wall during insufflation to a pressure of 12 mmHg in 18 patients undergoing laparoscopic surgery. Measurements are performed by means of a remote motion analysis system based on the use of 12 infrared markers placed on the abdomen surface. This system allows the estimation of an increase in the abdominal area of about 15%. The same calculation is performed on the anterior rectus sheet of the model, which is the most superficial and central abdominal structure being comparable with the experimental measure evaluated on the skin of the subjects. The percentage of area variation is computed, at 12 mmHg, in each membrane element by multiplying the principal strains and obtaining a measure of the same order of magnitude of the experimental findings, with values up to 14% allowing a partial model validation (Fig. 63). In another study by Martins et al., the attention is focused on the uni-axial tensile testing and constitutive modeling of the human anterior rectus sheet, accounting for its effective histological conformation. The nonlinear damage behavior of the tissue is described by means of a structural model built within the frame-work of nonlinear continuum mechanics. The damage process is simulated by considering different damage behaviors for the matrix and the collagen fibers [78]. A more recent study by Hernandez-Gascon et al. develops a finite element model of the abdominal wall starting from diagnostic images (MRI) of a healthy 38-year-old man [79]. The model takes into account the principal abdominal structures and adopts a hyperelastic transversely isotropic formulation for the description of their mechanical behavior. The parameter identification is performed by exploiting experimental data both from human and rabbit. For this reason, the results are not directly comparable to those of the present work, being rabbit muscle tissues even three times stiffer than the equivalent in man. The analysis is performed by applying an increasing intrabdominal pressure and evaluate the passive mechanical behavior of the abdomen by means of stress and displacement contours. The different biological structures results to be stiffer with respect to those of the present work because of the choice of the starting experimental data.

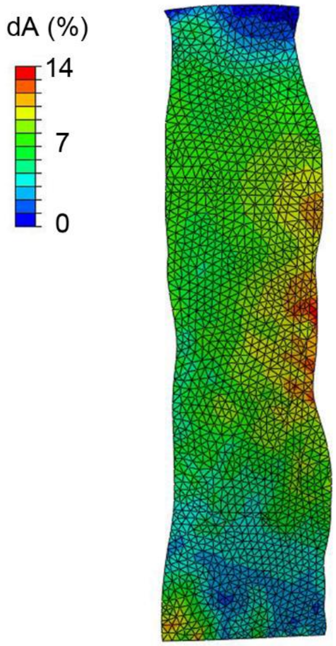

Figure 63 Percentage of area variation within each membrane element of the anterior rectus sheet at 12 mmHg.

Additional experimental investigations are needed to reach a more exhaustive validation of the model. Indeed, data at disposal are drawn from studies with a limited number of subjects. Further, this model takes into account the passive behavior of the abdomen, neglecting muscles active contraction whose action contributes also to the global basal tone that is not here considered. In addition, the mechanical behavior of these biological structures is considered in a balance state on the long period by neglecting the viscous phenomena that characterize all these connective tissues.

Despite the above mentioned limitations, this model represents an improvement of the researches at disposal about the behavior of the abdominal wall. Strong exemplification are often assumed in the description of the abdomen biomechanics by adopting the Laplace’s equation to correlate the radii of the abdominal surface and the inflation pressure [73, 77]. This assumption implies a direct proportionality between stress and the insufflated pressure, but evaluating the maximum displacements along the transversal and the craniocaudal direction, these are not proportional to the pressure increase. Further, large deformations and hyperelasticity characterizing the abdominal structures are neglected. By taking into account a data set completely drawn from human samples, the present work represents an improvement in comparison to a previously developed model accounting for data both from human and rabbit [79], providing a more feasible description of the healthy abdominal wall.

4.3.4.1 Biological mesh

Permacol™ is chosen as a representative example of biological grafts commonly used in the abdominal wall reconstruction. This tissue is obtained from porcine skin which undergoes decellularization and cross-linking processes. Mechanical characterization of this mesh was performed in a previous study by means of the development of uni-axial tensile tests, along two mutual perpendicular directions, and stress relaxation tests at different levels of strain imposed [80].

Uniaxial tensile tests highlighted Permacol™ isotropic behavior as reported in Figure 64 in terms of force for unit of undeformed width of the sample versus stretch. The tensile response is shown in the range which encloses the recognized upper physiological limit value of 16 N/cm for the forces acting on the abdominal wall [80].

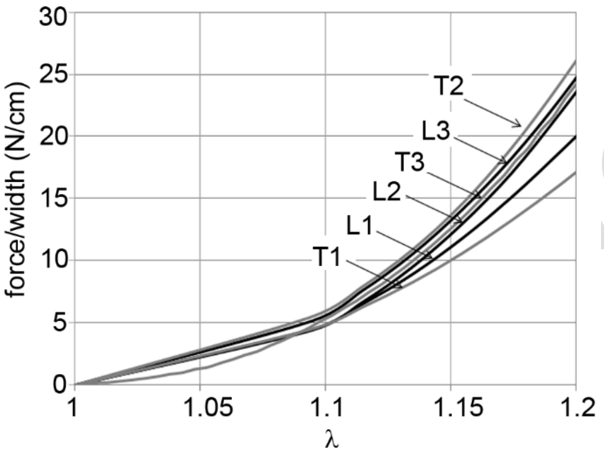

Figure 64 Force for unit of undeformed width versus stretch. L and T indicate samples tested in longitudinal and transversal directions [80].

The adopted constitutive formulation consists in the first order Ogden model, characterized by the following strain energy function:

$$W = \frac{2\mu}{\alpha}\left(\lambda_1^{\alpha} + \lambda_2^{\alpha} + \lambda_3^{\alpha} - 3\right) + U\left(J\right) \tag{4.2}$$

where μ is the shear modulus and α is a dimensionless material constant. The model well interprets Permacol™ biomechanical behavior, as shown in Figure 65. The constitutive parameters are reported in the following.

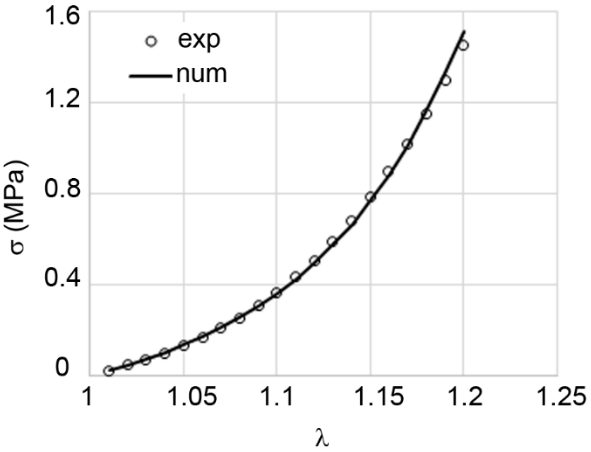

Figure 65 Stress-stretch behavior for the average Permacol™ response in terms of Cauchy stress versus stretch. The black solid line is the curve obtained by the numerical model, while open circles represent experimental data for the transversal direction.

μ (MPa)	α
0.75	16.45

Table 12 Constitutive parameters obtained by the best fit of the experimental tensile tests.

4.3.4.2 Synthetic mesh

Bard® Soft mesh is a lightweight, large pore monofilament polypropylene mesh widely used in abdominal wall surgery. Its particular structure, characterized by parallel filaments oriented only in one direction, appoints a strong anisotropic behavior to this graft (Fig. 66a). This behavior is highlighted by tensile tests developed both along and orthogonally to the filaments direction (Fig. 66b).

Uni-axial, equi-biaxial and plane strain tensile tests were developed for the global mechanical characterization of this mesh.

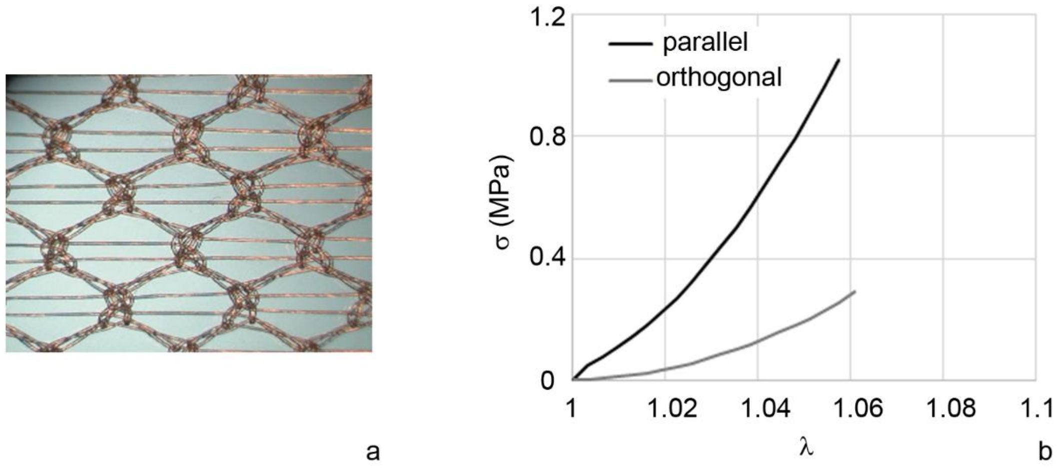

Figure 66 Bard® Soft structure (a). Stress-stretch behavior for the mechanical response to equi-biaxial tensile test along the parallel and the orthogonal direction with respect to the polypropylene filaments.

The adopted constitutive formulation assumes that the ground matrix is reinforced by two families of filaments lying in the membrane plane and it is expressed by the following strain energy function:

$$W = U(J) + \frac{\mu}{2}\left(\tilde{I}_1 - 3\right) + \sum_{i=1}^{2} w_{fi} \tag{4.3}$$

U is the term related to the change of volume, while the other terms are related to the volume-preserving strain. The second term is related to the ground matrix and the other terms to the families of filaments that reinforce the mesh. μ is a stress-like parameter that represents the ground matrix shear stiffness at small strains. The function W_{fi} is defined by means of the following exponential function to account for the filaments increasing stiffening response with strain:

$$w_{fi} = \frac{k_i}{2\alpha_i}\left\{\exp\left[\alpha_i\left(I_{4i}-1\right)\right]-\alpha_i\left(I_{4i}-1\right)-1\right\} \quad \left(i=1,2\right) \tag{4.4}$$

k_i are stress-like parameters, while α_i are dimensionless.

The obtained data fitting and the constitutive parameters are reported in the following:

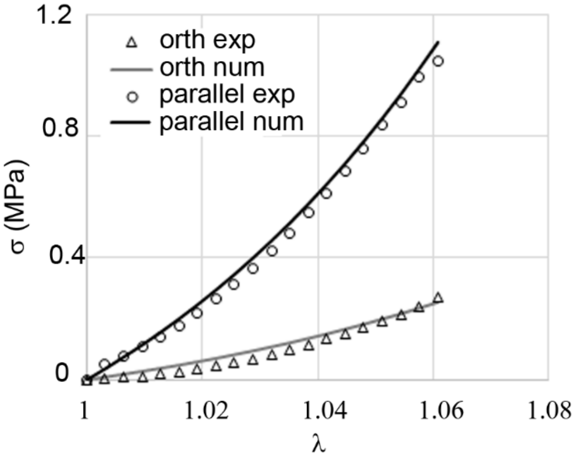

μ (MPa)	k_1 (MPa)	α_1	k_2 (MPa)	$\alpha 2$
0.00001	9.75	2.51	5.22	2.64

Figure 67 Stress-stretch behavior for the average Bard® Soft mesh response, both along the filaments (parallel) and perpendicularly to them (orthogonal), in terms of Cauchy stress versus stretch. The solid lines are the curves obtained by the numerical model, while open symbols represent experimental data from bi-axial tensile tests.

Table 13 Constitutive parameters obtained by the best fit of the experimental bi-axial tensile tests.

The stiffest direction of the mesh is oriented transversally to the abdomen, while the less stiff direction is oriented longitudinally with the aim to reproduce the physiological condition.

4.3.5 Numerical analysis and results: the pathological and repaired condition

Again, a uniform intrabdominal pressure of 0.023 MPa is applied to the internal surfaces of the abdomen. Two different values of IAP are considered for successive comparisons: 20 mmHg corresponding to the standing position, and the higher value of 60 mmHg which comprises most of the physiological tasks. In the following are reported the comparisons between the healthy condition and the abdominal wall after surgical repair simulated by means of a Permacol™ patch and Bard® Soft mesh.

Figures 68 and 69 make possible the comparison among the magnitude displacements computed during the standing position in the case of the healthy abdominal wall (a) and after surgical repair by means of Permacol™ (b) and Bard® Soft mesh (c).

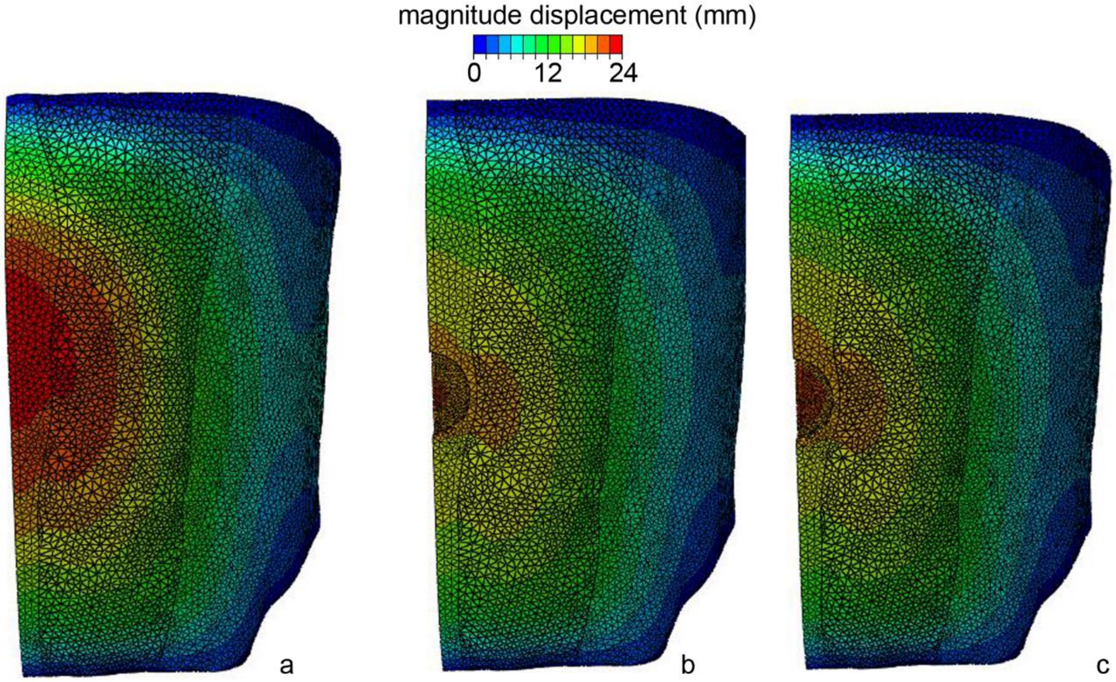

Figure 68 Front view of the magnitude displacement contour computed on the left abdomen side in the healthy condition (a) and after surgical repair by means of a Permacol™ patch (b) and Bard® Soft mesh (c) during the standing position.

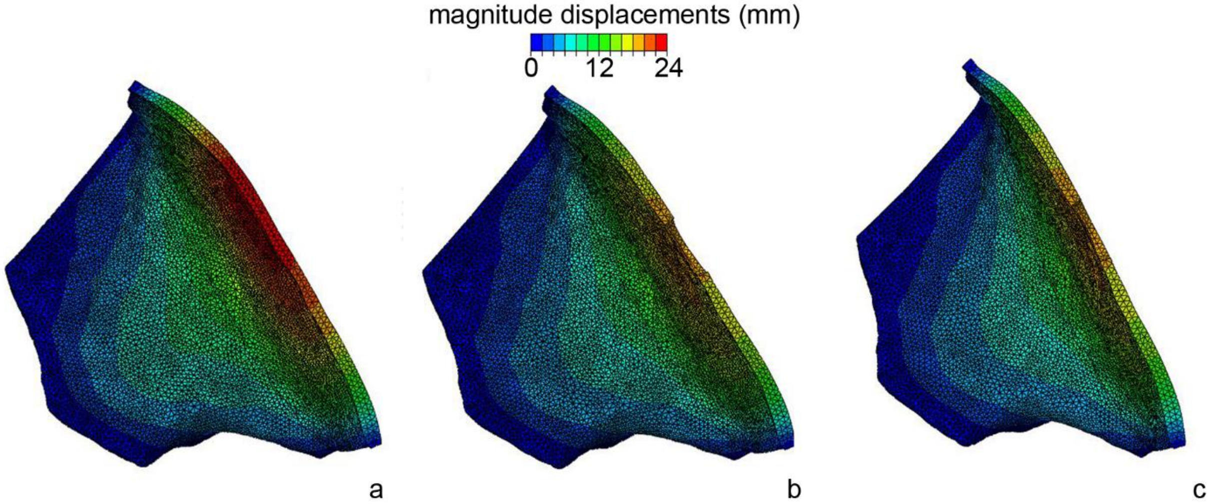

Figure 69 Side view of the magnitude displacement contour computed on the left abdomen side in the healthy condition (a) and after surgical repair by means of a Permacol™ patch (b) and Bard® Soft mesh (c) during the standing position.

Numerical results show a maximal displacement of 23.85 mm in the center of the abdomen during the standing position in the healthy condition. This value decreases to 20.32 mm after the simulation of the surgical repair by means of Permacol™, and 21.33 mm with the adoption of Bard® Soft mesh. The same results are reported in Figure 70 for two paths of nodes chosen along the craniocaudal (a) and the transversal direction (b).

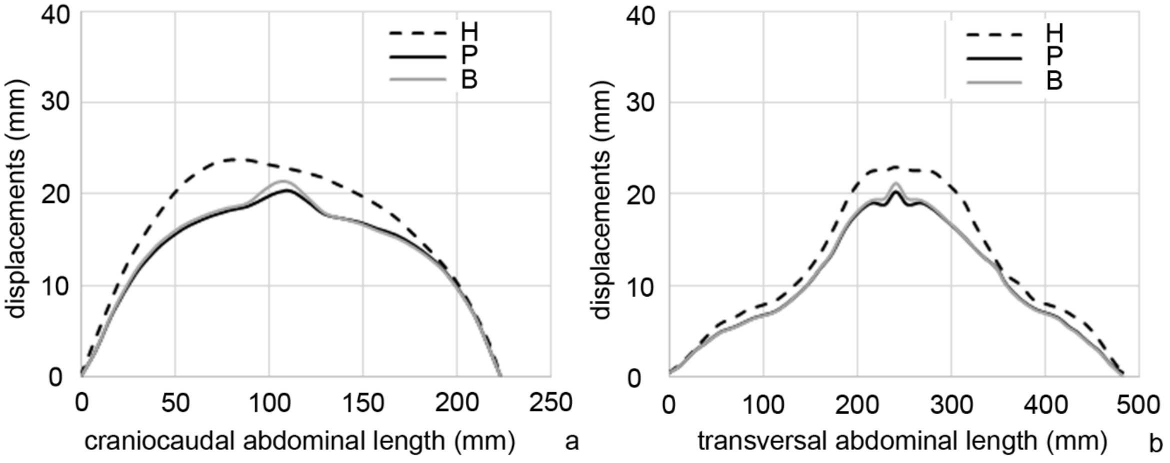

Figure 70 Magnitude displacements evaluated along the craniocaudal (a) and the transversal direction (b) during the standing position in the case of the healthy condition (H) and after surgical repair by means of Permacol™ (P) and Bard® Soft mesh (B).

Figure 71 reports the maximum principal strain computed in the standing position for the above described conditions.

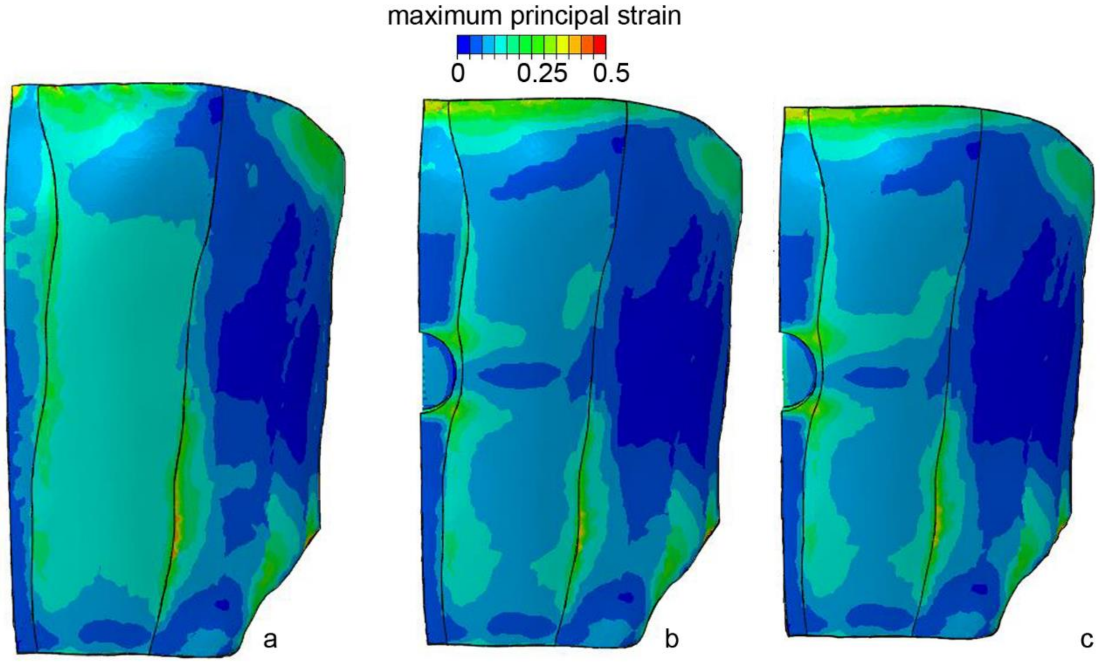

Figure 71 Front view of the maximum principal strain contour computed on the left abdomen side in the healthy condition (a) and after surgical repair by means of a Permacol™ patch (b) and Bard® Soft mesh (c) during the standing position.

In the following, the same numerical outcomes are reported for the intrabdominal pressure value of 60 mmHg.

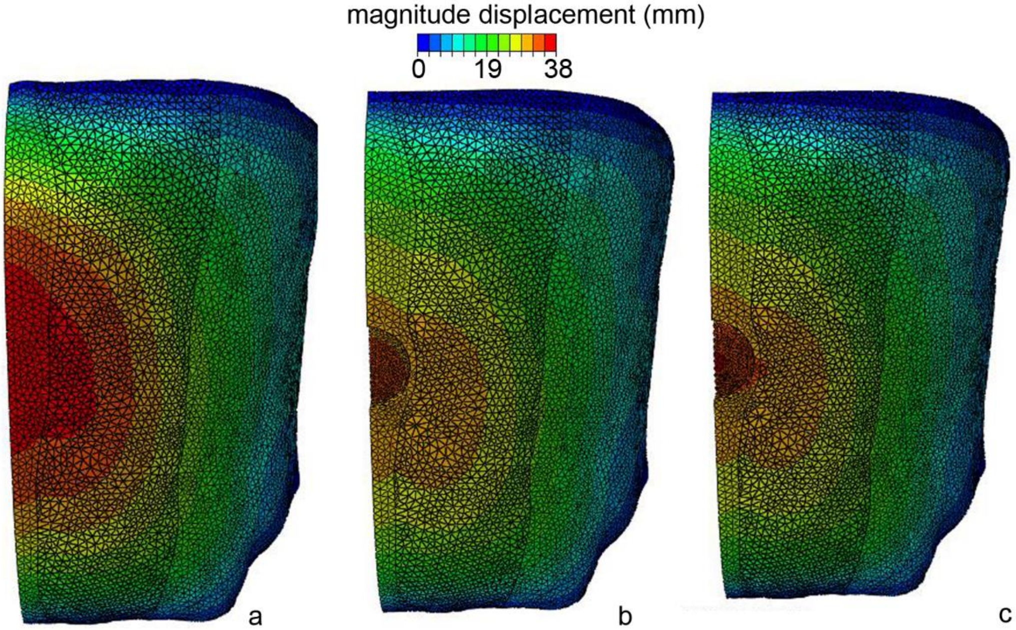

Figure 72 Front view of the magnitude displacement contour computed on the left abdomen side in the healthy condition (a) and after surgical repair by means of a Permacol™ patch (b) and Bard® Soft mesh (c) considering a IAP value of 60 mmHg.

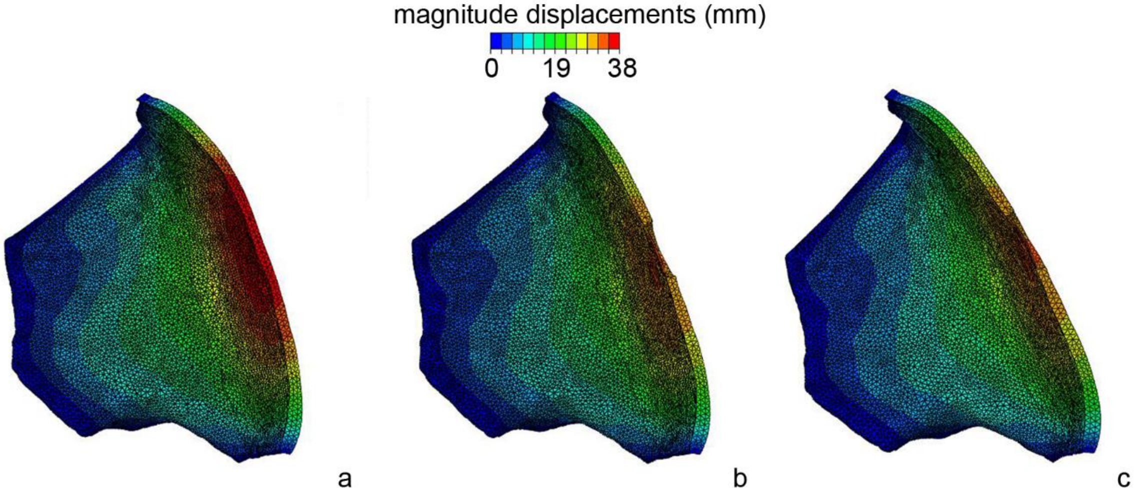

Figure 73 Side view of the magnitude displacement contour computed on the left abdomen side in the healthy condition (a) and after surgical repair by means of a Permacol™ patch (b) and Bard® Soft mesh (c) considering a IAP value of 60 mmHg.

The maximum displacement in the healthy condition is of 37.76 mm while it decreases to 33.56 mm in the case of surgical repair by means of Permacol™ and to 35.03 mm when Bard® Soft mesh is used.

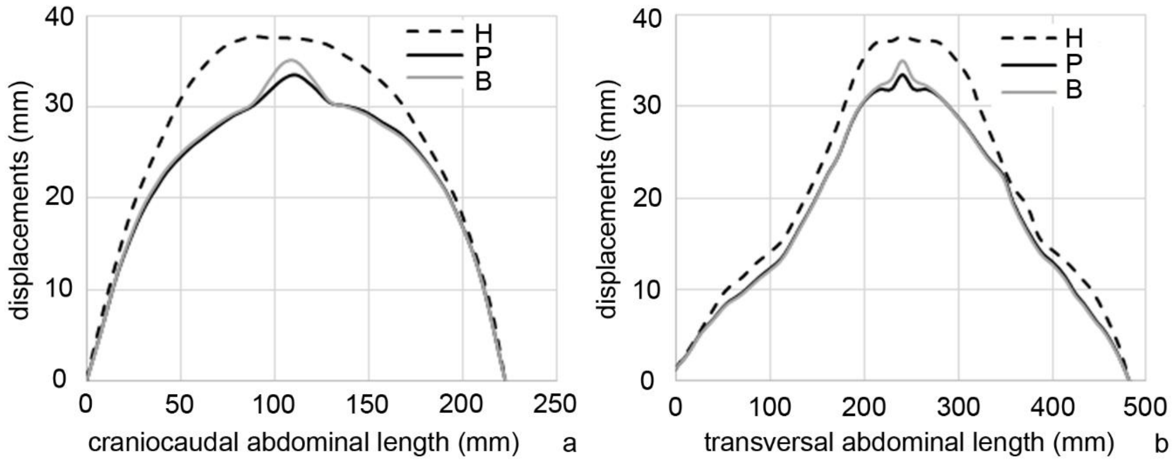

Figure 74 Magnitude displacements evaluated along the craniocaudal (a) and the transversal direction (b) in the case of the healthy condition (H) and after surgical repair by means of Permacol™ (P) and Bard® Soft mesh (B) considering a IAP value of 60 mmHg.

Figure 75 reports the results in terms of maximum principal strain.

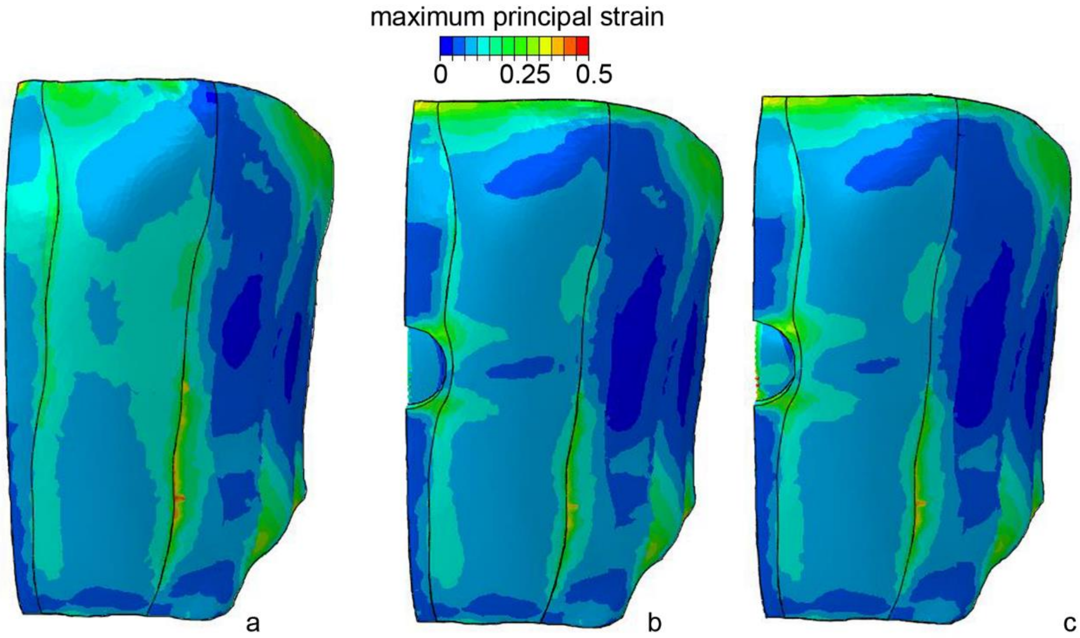

Figure 75 Front view of the maximum principal strain contour computed on the left abdomen side in the healthy condition (a) and after surgical repair by means of a Permacol™ patch (b) and Bard® Soft mesh (c) considering a IAP value of 60 mmHg.

By comparing numerical results it is possible to observe that the introduction of a surgical mesh determines a global stiffening of the abdominal wall, independently on the adopted kind of patch. The mismatch between the overall mechanical behavior of the healthy and repaired abdominal wall could be associated to the post-surgical pain and discomfort complained by patients.

Limited differences can be found by varying the kind of the surgical patch.

Another possible investigation can be performed by varying the orientation of the Bard® Soft mesh with respect to the craniocaudal and transversal abdominal directions. In the above reported results, the mesh stiffest direction matches with the abdominal transversal direction, while the mesh most compliant direction corresponds to the craniocaudal direction (dir1). By inverting the mesh orientation (dir2) it is possible to compare the effects induced by a misplacement of the patch (Fig. 76).

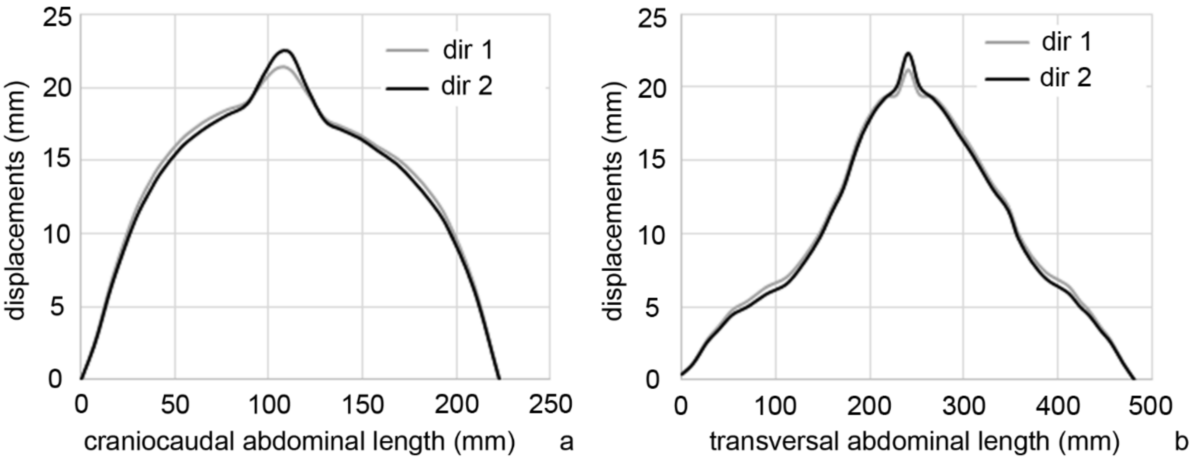

Figure 76 Magnitude displacements evaluated along the craniocaudal (a) and the transversal direction (b) in the standing position. The gray line represents the result obtained with Bard® Soft mesh oriented with the stiffest direction along the abdomen transversal direction (dir1). The black line is obtained by orienting the mesh stiffest direction along the craniocaudal direction (dir2).

The effects due to the mesh orientation affect primarily the region of the hernia inducing a greater deformation of the surgical patch, while the global mechanical behavior of the abdomen, in the regions surrounding the hernia, is almost unchanged.

As mentioned above, the mechanical behavior of the abdominal wall is here evaluated in a passive condition, neglecting the active behavior of the muscles that contract during the considered physiological tasks. The muscular contraction contributes to a stiffer mechanical response of the abdominal wall. This aspect could be taken into account for future developments together with the consideration of the time dependent phenomena through the adoption of a suitable constitutive formulation.

Despite of these limitations, the present work supply a useful tool for a preliminary evaluation of the mechanical effects induced by the introduction of a surgical mesh in the abdominal wall. Future developments include an extension of the investigated materials used the abdominal wall surgery with an in-depth analysis of different synthetic meshes.

CONCLUSIONS

The research activity proposed moves from the biomechanical characterization of fascial tissues, of a xenograft (Permacol™) and of a representative example of synthetic meshes (Bard® Soft mesh) commonly used in surgical repairs.

The mechanical characterization of the fascial tissues is performed by means of a large experimental activity and the adoption of a constitutive formulation consistent with tissues structural conformation and properties, such as large deformability, non-linear elasticity and viscoelastic properties. The numerical modelling of the crural fascia represents a step for the evaluation of fascial tissues structural behavior with the aim to assess their in situ functionality. This is performed by taking into account different loading conditions within the anterior lower limb compartment.

Different suitable constitutive models are chosen for the interpretation of the mechanical behavior of Permacol™ and Bard® Soft mesh.

The subsequent numerical modelling of the abdominal wall is addressed to the evaluation of the biomechanical properties and to the simulation of the different grafts functionality in healthy and pathological conditions. By assuming different mechanical characteristics for the meshes it is possible to evaluate different grafts behavior, allowing a useful comparison between different conformations and properties, as suitable tool according to the specific pathological cases, to evaluate the possible mechanical interaction between mesh and surrounding tissues. In general, the numerical model represents a useful support for surgical planning and general clinical-surgical considerations. Future possible advances and variations, for example the dimensions, the shape and the location of both the hernia defect and surgical meshes, will make it possible to perform sensitivity analysis depending on different features, leading to considerations that will be evaluated depending on patient specific approach.

REFERENCES

[1] Shankaran V, Weber DJ, Reed RL, Luchette FA (2011). A Review of Available Prosthetics for Ventral Hernia Repair. Ann Surg 253(1):16-26.

[2] Hernández-Gascón B, Peña E, Melero H, Pascual G, Doblaré M, Ginebra MP, Bellón JM, Calvo B (2011). Mechanical behaviour of synthetic surgical meshes: finite element simulation of the herniated abdominal wall. Acta Biomater 7(11):3905-3913.

[3] Gaertner WB, Bonsack ME, Delaney JP (2007). Experimental evaluation of four biologic prostheses for ventral hernia repair. J Gastrointest Surg 11(10):1275-1285.

[4] Hashizume R, Fujimoto KL, Hong Y, Amoroso NJ, Tobita K, Miki T , Keller BB, Wagner WR (2010). Morphological and mechanical characteristics of the reconstructed rat abdominal wall following use of a wet electrospun biodegradable polyurethane elastomer scaffold. Biomaterials 31 (12):3253-3265.

[5] Bellows CF, Alder A, Helton WS (2006). Abdominal wall reconstruction using biological tissue grafts: present status and future opportunities. Expert Rev Med Devic 3 (5):657-675.

[6] Matthews BD, Pratt BL, Pollinger HS, Backus CL, Kercher KW, Sing RF, Heniford BT (2003). Assessment of adhesion formation to intraabdominal polypropylene mesh and polytetrafluoroethylene mesh. J Surg Res 114:126–132.

[7] Read RC(2004). Milestones in the history of hernia surgery: prosthetic repair. Hernia 8:8–14.

[8] Todros S, Pavan PG, A. N. Natali (2015). Synthetic surgical meshes used in abdominal wall surgery: part I - materials and structural conformation. J Biomed Mater Res B Appl Biomater doi: 10.1002/jbm.b.33586.

[9] Klinge U (2007). Experimental comparison of monofile light and heavy polypropylene meshes: less weight does not mean less biological response. World J Surg 31:867–8.

[10] Cobb WS, Burns JM, Peindl RD, Carbonell AM, Matthews BD, Kercher KW (2006). Textile analysis of heavy-weight, mid-weight and light-weight polypropylene mesh in a porcine ventral hernia model. J Surg Res 136:1–7.

[11] Brown GL, Richardson JD, Malangoni MA, Tobin GR, Ackerman D, Polk HC (1985). Comparison of prosthetic materials for abdominal wall reconstruction in the presence of contamination and infection. Ann Surg 210:705–711.

[12] Klinge U, Klosterhalfen B, Ottinger AP, Junge K, Schumpelick V (2002). PVDF as a new polymer for the construction of surgical meshes. Biomaterials 23:3487–3493.

[13] Amid PK (1997). Classification of biomaterials and their related complications in abdominal wall hernia surgery. Hernia 1: 15-21.

[14] Maurer MM, Rohrnbauer B, Feola A, Deprest J, Mazza E (2014). Mechanical biocompatibility of prosthetic meshes: A comprehensive protocol for mechanical characterization. J Mech Behav Biomed 40:42-58.

[15] Dietz HP, Vancaillie P, Svehla M, Walsh W, Steensma AB, Vancaillie TG (2003). Mechanical properties of urogynecologic implant materials. Int. Urogynecol. J. Pelvic Floor Dysfunct. 14:239–243.

[16] Deeken CR, Abdo MS, Frisella MM, Matthews BD (2011). Physicomechanical evaluation of Polypropylene, Polyester, and Polytetrafluoroethylene Meshes for Inguinal Hernia Repair. J Am Coll Surg 212:68–79.

[17] Cobb WS, Peindl RM, Zerey M, Carbonell AM, Heniford BT (2009). Mesh terminology 101. Hernia 13:1–6.

[18] Culav EM, Clark CH, Merrilees MJ (1999). Connective tissues: matrix composition and its relevance to physical therapy. Phys Ther 79:308-319.

[19] Castro Brás LE, Shurey S, Sibbons PD (2012). Evaluation of crosslinked and non-crosslinked biologic prostheses for abdominal hernia repair. Hernia 16 (1):77-89.

[20] Society of American Gastrointestinal and Endoscopic Surgeons http://www.sages.org/wiki/biologic-mesh/ (last access 14-04-2015).

[21] Cano ML, Carrasco MA, Perez MTQ, Via MAA (2013). Biological implants in abdominal waal hernia surgery. Cir Esp 91(4):217–223.

[22] Cornwell KG, Landsman A, James KS (2009). Extracellular matrix biomaterials for soft tissue repair. Clin Podiatr Med Surg 26(4): 507-523.

[23] Ionescu MI, Ross DN, Deac R, Grimshaw VA, Taylor SH, Whitaker W, Wooler GH (1970). Autologous fascia lata for heart valve replacement. Thorax 25(1): 46–56.

[24] Nakata K, Shino K, Horibe S, Natsu-ume T, Mae T, Ochi T (2000). Reconstruction of the lateral ligaments of the ankle using solvent-dried and gamma-irradiated allogeneic fascia lata. J Bone Joint Surg Br 82(4):579-82.

[25] Cerruto MA, Cardarelli S, Aloisi A, Gigli F, Tiscione D, Arancio M, Ruggera L, Zattoni F, Curti P (2001). Pubo-vaginal sling using cadaveric fascia lata in the treatment of female stress urinary incontinence due to a sphincteric deficiency: our experience with a 10-year follow-up. J Urol 165(5):1605-11.

[26] Lemound J, Stoetzer M, Kokemüller H, Schumann P, Gellrich NC (2014). Modified Technique for Rehabilitation of Facial Paralysis Using Autogenous Fascia Lata Grafts. J Oral Maxillofac Surg 73:176–183.

[27] Stecco C, Porzionato A, Lancerotto L, Stecco A, Macchi V, Day JA, De Caro R (2008). Histological study of the deep fascia of the limbs. J Bodywork Mov Ther 12(3):225-30.

[28] Stecco C, Pavan PG, Porzionato A, Macchi V, Lancerotto L, Carniel EL, Natali AN, De Caro R (2009). Mechanics of crural fascia: from anatomy to costitutive modelling. Surg Radiol Anat 31:523-529.

[29] Benjamin M (2009) The fascia of the limbs and back – a review. J Anat 214: 1–18.

[30] Stecco A, Macchi V, Masiero S, Porzionato A, Tiengo C, Stecco C, Delmas V, De Caro R (2009). Pectoral and femoral fasciae: common aspects and regional specializations. Surg Radiol Anat 31:35–42.

[31] Stecco C, Pavan PG, Porzionato A, Macchi V, Lancerotto L, Carniel EL, Natali AN, De Caro R (2009). Mechanics of crural fascia: from anatomy to costitutive modelling. Surg Radiol Anat 31:523-529.

[32] Fung YC (1981). Biomechanics: mechanical properties of living tissues. Springer-Verlag, New York.

[33] Spencer AJM (1992). Continuum theory of the mechanics of fiber-reinforced composites. Springer-Verlag, New York.

[34] Holzapfel GA (2000). Nonlinear solid mechanics. John Wiley & Sons LTD, New York.

[35] Gurtin, ME (1981). An introduction to continuum mechanics. Academic Press, San Diego.

[36] Limbert G, Middleton J (2004). A transversally isotropic viscohyperelastic material: Application to the modeling of biological soft connective tissues. Int J Solids Struct 41: 4237-4260.

[37] Truesdell C, Noll W (1992). The non-linear field theories of mechanics (second edition), Springer-Verlag, Berlin.

[38] Belytschko T, Liu WK, Moran B (2001). Nonlinear finite elements for continua and structures, John Wiley & Sons LTD, New York.

[39] Carew TE, Vaishnav RN, Patel DJ (1968). Compressibility of the arterial wall. Circ Res 23(1):61-8.

[40] Zhang G (2005). Evaluating the viscoelastic properties of biological tissues in a new way. J Musculoskelet Neuronal Interact 5(1):85-90.

[41] Natali AN, Pavan PG, Carniel EL, Dorow C (2004). Viscoelastic response of the periodontal ligament: an experimental-numerical analysis. Connect Tissue Res 45:222-230.

[42] Lei F, Szeri AZ (2007). Inverse analysis of constitutive models: biological soft tissues, J Biomech 40 (4):936-940.

[43] Park MW, Kim YD (1998). A systematic procedure for setting parameters in simulated annealing algorithms. Computers Ops Res. 25(3):207-217.

[44] Pavan PG, Pachera P, Forestiero A, Reggiani C, Natali AN (2015). Investigation of interaction phenomena between crural fascia and muscles by using a three-dimensional numerical model. Under revision at J Biomech.

[45] Pavan PG, Pachera P, Stecco C, Natali AN (2015). Biomechanical behavior of human crural fascia in anterior and posterior regions of lower limb. Med Biol Eng Comput 53(10):951-9.

[46] Pavan PG, Stecco C, Pachera P, De Caro R, Natali AN (2014). Investigation of the mechanical properties of the human crural fascia and their possible clinical implications. Surg Radiol Anat 36(1):25-32.

[47] Natali AN, Carniel EL, Pavan PG (2008). Constitutive modelling of inelastic behaviour of cortical bone. Med Eng Phys 30(7):905-912.

[48] Pfaeffle HJ, Toamino MM, Grewal R, Xu J, Boardman ND, Woo SL, Herndon JH (1996). Tensile properties of the interosseous membrane of the human forearm. J Orthop Res 14(5): 842-845.

[49] Nordez A, Hug F (2010). Muscle shear elastic modulus measured using supersonic shear imaging is highly related to muscle activity level. J Appl Physiol 108:1389-1394.

[50] Geerligs M, Peters WMG, Ackermans PAJ, Oomens CWJ, Baaijens FTP (2008). Linear viscoelastic behavior of subcutaneous adipose tissue. Biorheology 45:677–688.

[51] Mattei CP, Beca S, Zahouani H (2008). In vivo measurements of the elastic mechanical properties of human skin by indentation tests. Med Eng Phys 30:599–606.

[52] Pavan PG, Pachera P, Natali AN (2015). Numerical modelling of crural fascia mechanical interaction with muscular compartments. Proc Inst Mech Eng H J Eng Med Part h 229(5):395-402.

[53] French EZ, Price WH (1962). Anterior tibial pain. Br Med J 2:1290.

[54] Gershuni DH, Gosink BB, Hargens AR, Gould RN, Forsythe JR, Mubarak SJ, Akeson WH (2011). Ultrasound evaluation of the anterior musculofascial compartment of the leg following exercise. Clin Orthop Relat Res 10:59-65.

[55] Hurschler C, Vanderby R, Martinez DA, Vailas AC, Turnipseed WD (1994). Mechanical and biomechanical analyses of tibial compartment fascia in chronic compartment syndrome. Ann Biomed Eng 22:272-279.

[56] Friden J, Sfakianos PN, Hargens AR (1985). Muscle soreness and intramuscular fluid pressure: comparison between eccentric and concentric load. J Appl Physiol 61(6):2175-9.

[57] Roman M, Chaudhry H, Bukiet B, Stecco A, Findley WT (2013). Mathematical Analysis of the Flow of Hyaluronic Acid Around Fascia During Manual Therapy Motions. J Am Osteopath Assoc 113:600-610.

[58] Mijailovich SM, Stojanovic B, Ko Liang A, Wedeen VJ, Gilber RJ (2010). Derivation of a finite-element model of lingual deformation swallowing from the mechanics of mesoscale myofiber tracts obtained by MRI. J Appl Physiol 109:1500-1514.

[59] Joahansson T, Meier P, Blickhan R (2000). A finite-element model for the mechanical analysis of skeletal muscle. J Theor Biol 206:131-149.

[60] Eheret AE, Böl M, Itskiv M (2011). A continuum constitutive model for the active behaviour of skeletal muscle. J Mech Phys Solids 59:625-636.

[61] Mubarak SJ, Owen CA, Hargens AR, Garetto LP, Akeson WH (1978). Acute compartment syndromes: diagnosis and treatment with the aid of the wick catheter. J Bon Joint Surg Am 60(8):1901-1905.

[62] Friden J, Sfakianos PN, Hargens AR (1985). Muscle soreness and intramuscular fluid pressure: comparison between eccentric and concentric load. J Appl Physiol 61(6):2175-9.

[63] Cooper A, Key SA (1844). The anatomy and surgical treatment of abdominal hernia: with numerous plates. Philadelphia: Lea & Blanchard.

[64] Gascon BH (2013). Mechanical modelling of the abdominal wall and biomaterials for hernia surgery. PhD thesis.

[65] Ahluwalia HS , Burger JP, Quinn TH (2004). Anatomy of the anterior abdominal wall. Oper Tech Gen Surg 6(3):147-155.

[66] Norasteh A, Ebrahimi E, Salavati M, Rafiei J, Abbasnejad E (2007). Reliability of B-mode ultrasonography for abdominal muscles in asymptomatic and patients with acute low back pain. J Bodyw Mov Ther 11.1: 17-20.

[67] Urquhart DM, Barker PJ, Hodges PW, Story IH, Briggs CA (2005). Regional morphology of the transversus abdominis and obliquus internus and externus abdominis muscles. Clin Biomec 20.3: 233-241.

[68] Muysoms FE, Miserez M, Berrevoet F, Campanelli G, Champault GG, Chelala E, Dietz UA, Eker HH, Nakadi IE, Hauters P, Pascual MH, Hoeferlin A, Klinge U, Montgomery A, Simmermacher RKJ, Simons MP, Smietanski M, Sommeling C, Tollens T, Vierendeels T, Kingsnorth A (2009). Classification of primary and incisional abdominal wall hernias. Hernia13:407–414.

[69] Skandalakis PN, Zoras O, Skandalakis JE, Mirilas P (2006). Spigelian hernia: surgical anatomy, embryology, and technique of repair. Am Surg 72(1):42-8.

[70] Cobb WS, Burns JM, Kercher KW, Matthews BD, Norton HJ, Heniford BT (2005). Normal Intraabdominal pressure in healthy adults. J. Surg. Res 129.2: 231-235.

[71] Klinge U, Klosterhalfen B, Conze J, Limberg W, Obolenski B, Öttinger AP, Schumpelick V (1998). Modified mesh for hernia repair that is adapted to the physiology of the abdominal wall. Eur J Surg, 164.12: 951-960.

[72] Pachera P, Pavan PG, Todros S, Cavinato C, Fontanella CG, Natali AN (2015). “A numerical investigation of the healthy abdominal wall structures”. Under revision at J Biomech

[73] Förstemann T, Trzewik J, Holste J, Batke B, Konerding MA, Wolloscheck T, Hartung C (2011). Forces and deformations of the abdominal wall—a mechanical and geometrical approach to the linea alba. J Biomech 44.4: 600-606.

[74] Abdelounis HB, Nicolle S, Otténio M, Beillas P, Mitton D (2013). Effect of two loading rates on the elasticity of the human anterior rectus sheath. J Mech Behav Biomed Mater, 20: 1-5.

[75] Cardoso MHS (2012). Experimental study of the Human Abdominal Wall. Universidade do Porto PhD thesis.

[76] Konerding MA, Bohn M, Wolloscheck T, Batk B, Holste JL, Wohlert S, Trzewik J, Förstemann T, Hartung C (2011). Maximum forces acting on the abdominal wall: Experimental validation of a theoretical modeling in a human cadaver study. Med Eng Phys 33:789–792.

[77] Song C, Alijani A, Frank T, Hanna GB, Cuschieri A (2006). Mechanical properties of the human abdominal wall measured in vivo during insufflation for laparoscopic surgery. Surg Endosc 20: 987–990.

[78] Martins P, Peña E, Natal Jorge RM, Santosd A, Santos L, Mascarenhas T, Calvo B (2011). Mechanical characterization and constitutive modelling of the damage process in rectus sheath. J Mech Behav Biomed Mater 8:111-22.

[79] Hernández-Gascón B, Mena A, Peña E, Pascual G, Bellón JM, Calvo B (2013). Understanding the passive mechanical behavior of the human abdominal wall. Ann Biomed Eng 41(2):433-44.

[80] Pavan PG, Pachera P, Todros S, Tiengo C, Natali AN (2015). Mechanical characterization of animal derived grafts for surgical implantation. J Mech Med Biol. doi: 10.1142/S0219519416500238.